ACS Catalysis

Review

Cite This: ACS Catal. 2020, 10, 1024−1059

pubs.acs.org/acscatalysis

Facet-Engineered Surface and Interface Design of Monoclinic Scheelite Bismuth Vanadate for Enhanced Photocatalytic Performance

Sha Chen,[†,‡] Danlian Huang,*[,†,‡] Piao Xu,[†,‡] Xiaomin Gong,[§] Wenjing Xue,[†,‡] Lei Lei,[†,‡] Rui Deng,[†,‡] Jing Li,[†,‡] and Zhihao Li[†,‡]

[†]College of Environmental Science and Engineering, Hunan University, Changsha 410082, China

[‡]Key Laboratory of Environmental Biology and Pollution Control, Hunan University, Ministry of Education, Changsha 410082, China

[§]College of Resources and Environment, Hunan Agricultural University, Changsha 410128, China

ABSTRACT: Monoclinic scheelite bismuth vanadate (mBiVO$_4$) has gradually been in the limelight in recent years because of its great potential in energy conversion and environmental remediation. However, the rapid recombination of photogenerated electron−hole pairs in mBiVO$_4$ have impeded the improvement of its photocatalytic performance and stability. Therefore, important issues are increasingly focused on fine-tuning the physicochemical properties of mBiVO$_4$ at the atomic level based on facet-engineered surface and interface design to optimize its selectivity and activity. Herein, the review begins with the fundamental aspects of mBiVO$_4$ semiconductor, including crystal structure, optical properties, electronic structure, and photocatalytic principles. Then the synthetic methods based on surface and interface design that develop to tailor the facet of mBiVO$_4$, along with the discussion of the mechanisms for facet-dependent photocatalytic performance, are presented. Most importantly, the latest advances in facet engineering that have been performed to regulate the surface of single mBiVO$_4$ and to design the interface structures that are directly involved in the photocatalytic reaction for mBiVO$_4$-based composites are encompassed. Moreover, the photocatalytic application achievements with mBiVO$_4$ as photocatalysts in energy conversion and environmental remediation are also summarized. Finally, perspectives on the existing challenges and future research directions for this emerging frontier are discussed.

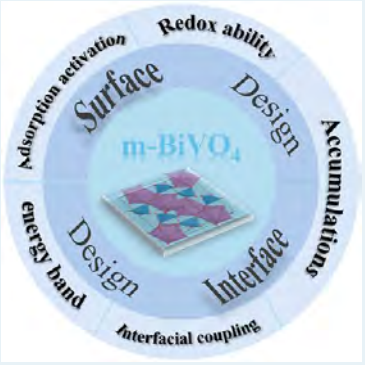

KEYWORDS: *monoclinic scheelite bismuth vanadate (mBiVO$_4$), facet-engineering, surface, interface, photocatalysis*

1. INTRODUCTION

Environmental pollution and energy shortage, as a byproduct of industrialization and rapid population growth, have attracted an increasing attention around the world.[1,2] For sustainable development, the development of nonpolluting technologies for environmental restoration and energy conversion is one of the top priorities for the moment. Conventional physical and biological treatment techniques, such as adsorption,[3−5] ultrafiltration,[6] bioflocculation,[7,8] and phytoremediation,[9,10] are limited by the inability to perform advanced processing, high cost, and secondary pollution. Therefore, our goal should be to promote the exploitation of environmentally friendly, ecologically harmonious, sustainable, and high-energy chemical technologies, which is the most pressing challenge the scientific community faces. Photocatalysis, a process to convert solar energy into chemical energy, is regarded as a promising direction to alleviate the increasingly serious environmental and issues and energy crisis.[11−13]

Semiconductor photocatalysis is a process in which the energy generated by electron photoexcitation across semiconductors' bandgaps participates in the surface reaction of chemical compounds, wherein a semiconductor is an important factor for evaluating photocatalytic performance. Among various semiconductors, TiO_2 with high photoreactivity, excellent stability, and low toxicity has gathered the most extensive research interest in the scientific community,[14−16] ever since the landmark work reported by Fujishima and Honda of photoelectrochemical water splitting using TiO_2 photoelectrode under ultraviolet light irradiation in 1972.[17] Thereafter, Frank and Bard employed TiO_2 as a photocatalyst to achieve photocatalytic reduction of CN^- in 1977 and obtained excellent remediation efficiency.[18] Since then, the application of semiconductor photocatalytic technology has attracted extensive attention, and significant progress has been made in photocatalytic degradation of hazardous substances,[19,20] photocatalytic water splitting,[21,22] artificial photosynthesis,[23−25] and photoelectrochemical conversion.[26−28] Nevertheless, the relatively wide band gap (3.2 eV) caused by its inherent high-positive valence band (VB) limits its absorption to ultraviolet light accounting for only 5%

Received: August 11, 2019
Revised: December 2, 2019
Published: December 11, 2019

DOI: 10.1021/acscatal.9b03411
ACS Catal. 2020, 10, 1024−1059

energy distribution of solar energy, resulting in poor photocatalytic performance. Given that, the development of high quality, efficient, and stable visible-light-response semiconductors for environmental remediation and energy conversion remains a challenging research direction.

Among numerous visible-light-response materials, bismuth vanadate especially the monoclinic scheelite structure hereinafter referred to mBiVO$_4$, has stood out as a frontier photocatalyst for various important reactions since Kudo et al. used mBiVO$_4$ as a photocatalyst to achieve photocatalytic water oxidation with Ag^+ ions as an electron scavenger under visible light irradiation.[29] In addition, there is a hybrid orbital of Bi 6s and O 2p in the electronic structure of mBiVO$_4$ compared with TiO$_2$ whose electronic structure consists only of O 2p orbitals and can only respond to ultraviolet light (Figure 1). The existence of additional Bi 6s orbitals results in

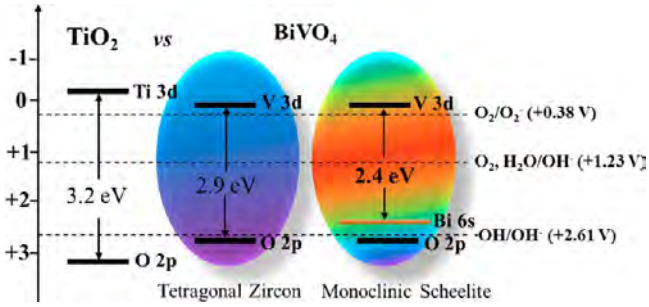

Figure 1. Energy and band structure diagram of tetragonal zircon and monoclinic scheelite BiVO$_4$ (mBiVO$_4$) in comparison to TiO$_2$ at pH 0.

a short transfer distance for the excited electrons in the VB of mBiVO$_4$ to the V 3d state in the conduction band (CB) of VO_4^{3-}, which leads to a decrease in bandgap energy, thereby significantly expanding the light absorption region to visible light.[30] More importantly, mBiVO$_4$ with controllable crystal facets greatly affects the charge separation and transfer process due to the different atomic coordination and configurations in different facets that determines the electronic structure and optical properties of mBiVO$_4$.[31]

The unique facet structure of mBiVO$_4$ endows it great potential as an excellent photocatalyst, and extensive research has been conducted on this attractive semiconductor. Example such as a comprehensive review outlining the prospective progress of mBiVO$_4$-based photocatalyst in photocatalytic water treatment was reported by Samsudin.[32] Nevertheless, the wide application of mBiVO$_4$ is still limited by its low electron transfer efficiency,[33] slow water oxidation kinetics,[34] poor charge carrier mobility,[35] and weak surface adsorption capacity.[36] Subsequently, various modification strategies such as morphological modification,[37] element doping,[38] semiconductor coupling,[39,40] deposition of cocatalysts,[41,42] defect formation (oxygen vacancy generation),[43] and crystal facet control[44] have been developed to achieve enhanced photocatalytic performance. In view of this popular topic, several excellent reviews with respect to the feasible strategies for improving the photocatalytic and/or photoelectrochemical performance of mBiVO$_4$ have been reported.[45,46] Nevertheless, the synthesis of effective and commercially viable mBiVO$_4$ and/or mBiVO$_4$-based materials for various photocatalytic applications are yet to be realized.

More recently, an increasing exploration has focused on the surface and interface engineering of materials because the surface as the adsorption and activation sites of the reactive species has a significant impact on the efficiency of surface redox reactions involving photogenerated electrons and/or holes, and the interface created between two adjacent components plays an important role in the interfacial charge transfer from light-harvesting centers to the surface reaction sites.[47,48] This importance to the improvement of photocatalytic performance has been gradually projected onto mBiVO$_4$. Since the facets forming the surface and interface are key factors to consider, the current research focus has shifted to designing the surface structure of mBiVO$_4$ from the atomic level to achieve morphological control of the crystal facets on the micro and nanoscales. Moreover, the daily published reports on the facet control of mBiVO$_4$ to further explore its potential applications in photocatalysis indicates that the relevant exploration on such topic is growing at an increasing speed. However, as far as we can identify from the literature, no review on this subject has been published so far; therefore, a timely and comprehensive review about the surface and interface design of mBiVO$_4$ based on facet engineering is highly desirable to promote the latest developments in this field of research.

Herein, we will focus on the facet-engineered surface and interface design of mBiVO$_4$ in photocatalysis, including controlled synthesis, rational design, and further behavior evaluation of novel photocatalysts for environmental restoration and energy conversion. Specifically, this Review starts by briefly introducing the fundamental aspects of mBiVO$_4$ semiconductor, including crystal structure, optical properties, electronic structure, and photocatalytic principles. As a bridging section, the common methods for the synthesis of mBiVO$_4$ with specific facet exposure are presented, accompanied by the discussion of facet-dependent performance in various photocatalytic reactions. Especially, facet engineering that attempts to regulate the surface of single mBiVO$_4$ and to combine with other strategies for the modification of charge carrier behavior in mBiVO$_4$-based photocatalytic system is discussed in detail. Moreover, the design is not the end of facet engineering, which has to be evaluated by various photocatalytic reactions. Therefore, the photocatalytic application achievements of mBiVO$_4$ photocatalytic system in energy conversion and environmental remediation are also summarized. Finally, perspectives and future research directions on this emerging frontier are discussed, with the aim to take advantage of the outstanding structure and electronic properties of facet-controlled mBiVO$_4$ for various energy and environment-related applications.

2. FUNDAMENTAL ASPECTS OF MBIVO$_4$ SEMICONDUCTOR

Natural BiVO$_4$ exists as a mineral pucherite with orthogonal structure, while BiVO$_4$ synthesized in the laboratory mainly exists in three forms, namely, tetragonal zircon, tetragonal scheelite, and monoclinic scheelite, of which only thermodynamically stable monoclinic scheelite mBiVO$_4$ exhibits excellent photocatalytic performance under visible light irradiation.[49] This relatively high photocatalytic performance of mBiVO$_4$ is largely determined by its crystal structures. Therefore, a brief overview of the crystal structures available for mBiVO$_4$ and its corresponding electronic structures and optical properties are paramount for well understanding the

DOI: 10.1021/acscatal.9b03411
ACS Catal. 2020, 10, 1024−1059

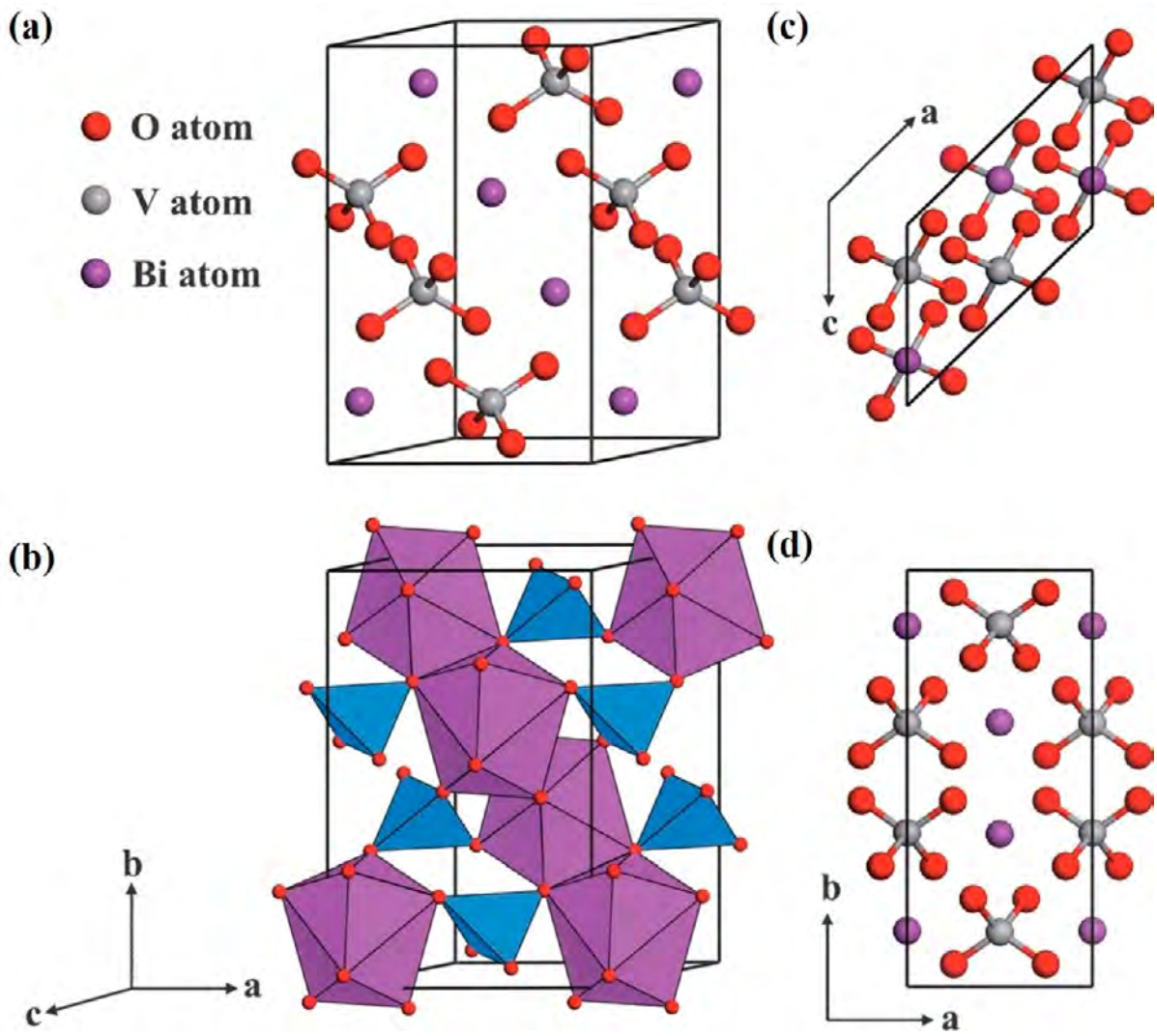

Figure 2. (a) Crystal structure of mBiVO$_4$. The corresponding polyhedron structure is represented in (b) (VO$_4$ tetrahedron in blue, and BiO$_8$ dodecahedron in purple). The top view (c) and side view (d) of the structure are also given. Reproduced with permission from ref 50. Copyright 2011 Royal Society of Chemistry.

relationship between structure and photocatalytic performance, which will be elaborated in detail in this section.

2.1. Crystal Structures. The basic structural unit of mBiVO$_4$ is composed of VO$_4$ tetrahedron and BiO$_8$ dodecahedron, in which the V site coordinates with four oxygen atoms and the Bi site is surrounded by eight oxygen atoms, as displayed in Figure 2.[50] Moreover, the alternating arrangement of Bi and V atoms along the crystallographic axis endows mBiVO$_4$ layered structural characteristics, with the difference that the −Bi−V− configuration is along the a (or c) axis while the −Bi−V-V-Bi- configuration is along the b-axis.[51,52]

The structure determines performance, as demonstrated by Tokunaga et al.; for example, mBiVO$_4$ exhibited relatively high photocatalytic performance for oxygen evolution compared to tetragonal scheelite BiVO$_4$ regardless of exposure to visible light or UV light, in spite of their comparable band gap energies.[53] An excellent explanation for this different photocatalytic performance based on surface energy calculations is that the local environment at the V and Bi site in mBiVO$_4$ exhibits more significant deformation, as opposed to the tetragonal and zircon-type forms with symmetric structures.[54] The distortion of BiO$_8$ results in an improved lone-pair effect of the Bi 6s,[55] and the VO$_4$ tetrahedral distortion can induce an internal electric field, which not only promotes the separation of photogenerated electron−hole pairs but also endows it anisotropic optical properties.[54]

2.2. Optical Properties and Electronic Structures of mBiVO$_4$ Semiconductor. In terms of the optical anisotropy of mBiVO$_4$, density functional theory (DFT) calculation showed that the presence of well-dispersed Bi 6 s orbitals in VB maximum (VBM) can influence the optical anisotropy near the absorption edge and accelerate the charge mobility, thereby resulting in optimal photocatalytic performance.[50] More importantly, Zhang et al. reported that mBiVO$_4$ nanosheets with an exposed {010} facet exhibited better spectral selectivity and improved color properties than the corresponding bulk materials.[56] An excellent explanation for this improved photocatalytic activity and selectivity is the optical anisotropy of mBiVO$_4$, that is, the visible-light absorption mainly arises from the photon incident along the direction of a- and c- axis. This optical anisotropy can provide guidance for the preparation of mBiVO$_4$ with better light absorption ability by increasing the exposure ratio of {100} or {001} facet, which

DOI: 10.1021/acscatal.9b03411
ACS Catal. 2020, 10, 1024−1059

also demonstrates the importance of surface and interface design based on facet engineering for improving the photocatalytic activity of mBiVO$_4$.

In addition to optical anisotropy, the slight distortion of crystal structure in mBiVO$_4$ also determines its electronic structure, and many investigations on this structure have been performed. For instance, Walsh et al. reported that hybridization between the Bi 6s and O 2p states at the top of the VB is responsible for the smaller band gap of the mBiVO$_4$, while the CB is composed of O 2p and Bi 6p orbitals,[57] which is in agreement with the model proposed by Payne et al.[58] That an interaction between the O 2p and Bi 6s at the VBM as well as the Bi 6p result in electron asymmetry around the Bi atom, which greatly improves the stability of mBiVO$_4$. However, Zhao et al. proposed a different structure on the basis of their DFT calculations; that is, mBiVO$_4$ is an indirect bandgap semiconductor.[53] The VBM is predominated by the nonbonding O 2p$_\pi$ and Bi 6s orbitals, while the bottom of the CB is mainly the nonbonding V 3d. The relatively narrow band gap of mBiVO$_4$ is attributed to the lone-pair distortion in Bi 6s, resulting in the upshift of the O 2p states to lower energy level.

More recently, Cooper and his co-worker gave a comprehensive research based on experiment and DFT calculations, which provided insight into the electronic structure, including the orbital character of CB and VB of mBiVO$_4$ (Figure 3).[59] According to the DFT and partial

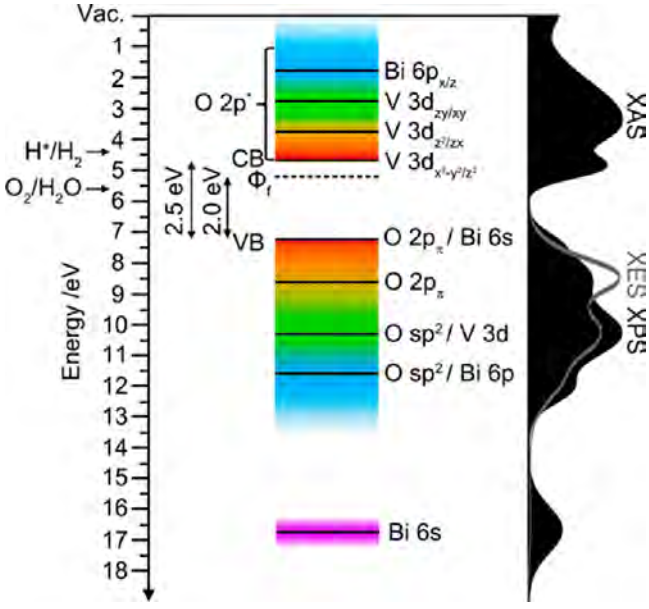

Figure 3. Energy level diagram representing the electronic structure of mBiVO$_4$ based on DFT calculations and experimental spectra. The dominant orbital character in each region is represented with respect to the vacuum level. Reproduced with permission from ref 59. Copyright 2014 American Chemical Society.

densities of states (DOS) results, the VB is mainly O 2p state, wherein VBM consists of the contributions of nonbonding O 2p$_\pi$ and Bi 6s The CB is determined by the V 3d states with primarily $d_{x^2-y^2}$ and d_{z^2} character at the lowest energy edge, but contains Bi 6p character at the upper region. Additionally, the band gap is determined to be 2.48 eV by combining X-ray absorption spectrum (XAS) and X-ray emission spectroscopy measurements (XES), resulting in good absorption capacity in the visible light region, which can well explain the enhance photocatalytic performance for water oxidation in mBiVO$_4$ compared with zircon-based BiVO$_4$ under visible light irradiation.

In summary, the theoretical investigation on the crystal structure, optical properties, and electronic structures of mBiVO$_4$ can provide excellent guidance for further exploring the potential of mBiVO$_4$. Previous studies have demonstrated that the photocatalytic performance of mBiVO$_4$ is largely dependent on its exposed facets, and the exposed facets can be obtained by selectively controlling the nucleation and growth rates of mBiVO$_4$ in different directions during crystal growth. In this regard, the crystal structure investigation facilitates the precise control of parameters in the facet synthesis process. Moreover, since the differences in optical properties and electronic structures of different facets result in facet-dependent photocatalytic performance, the optimal photocatalytic performance can be achieved by facet engineering to increase the exposed area of the favorable crystal facets. The following content is a good proof of the above.

2.3. Photocatalytic Principles over mBiVO$_4$ Semiconductor. Given that environmental restoration and energy conversion are the biggest bottlenecks at present, photocatalytic organic pollutants degradation and water splitting are two of the most challenging and important applications. In the case of Gibbs free energy, the organic degradation involving oxygen molecules is a photoinduced downhill reaction, the core of which lies in the generation of reactive oxygen species through the redox reaction between the photogenerated charge carriers and the water molecule or dissolved oxygen. Conversely, photocatalytic water splitting involves the conversion of photon energy into chemical energy with a large positive change in Gibbs free energy, which is a typical uphill reaction. Despite the above differences, they follow the same principle of photocatalysis, the conversion efficiency of solar energy to chemical energy is codetermined by light capturing efficiency, charge separation efficiency and charge utilizations' efficiency (Figure 4).[60] In general, under light

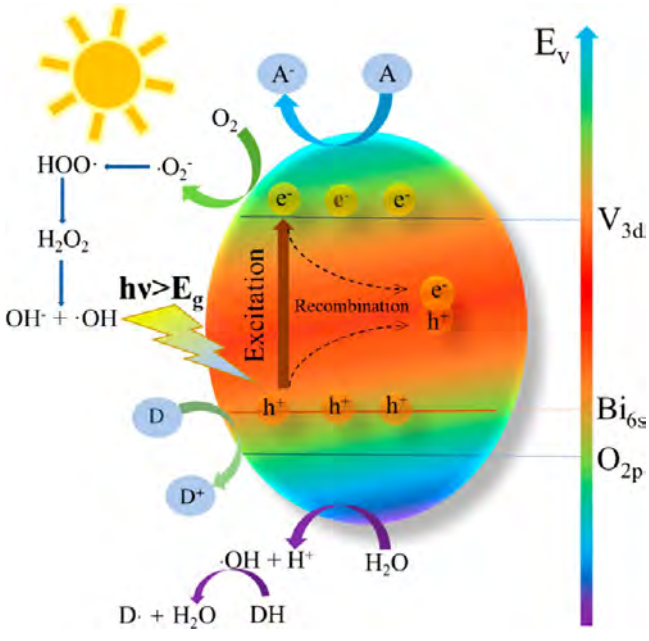

Figure 4. Schematic illustration for energetics and primary reaction mechanism of mBiVO$_4$ photocatalyst.

DOI: 10.1021/acscatal.9b03411
ACS Catal. 2020, 10, 1024−1059

irradiation, mBiVO$_4$ absorbs photons higher than or equal to its band gap energy to generate photogenerated charge carriers, followed by the transfer of excited electrons from the VB to the corresponding CB, leaving positive holes in the VB. Subsequently, the excited electrons and holes migrate to the surface of mBiVO$_4$ to participate in the redox reaction therein for solar energy conversion and mineralization of chemisorbed species. Note that mBiVO$_4$ exhibits chemical activity only when excited electrons and holes are consumed for the surface redox reactions. However, in fact, the chemical reaction between mBiVO$_4$ and the adsorbed pollutants is completed in 10^{-8} to 10^{-3} seconds, which is far longer than the time of recombination of electron−hole pairs, within a fraction of nanoseconds.[56] Therefore, the fast recombination of photogenerated electrons and holes is the main limiting step in evaluating the photocatalytic performance of mBiVO$_4$.

As mentioned before, optimal solar-to-chemical energy conversion is obtained only when photogenerated electrons and/or holes are effectively consumed by the surface reaction species. To improve the consumption efficiency of photogenerated charge carriers, the surface structure that is related to the adsorption and activation abilities of reaction species is a key factor to consider. Besides, in order to promote the separation and transfer of photogenerated charge carriers, research with respect to mBiVO$_4$ has developed from optimizing single mBiVO$_4$ to designing mBiVO$_4$-based composites. For mBiVO$_4$-based hybrid photocatalysts, the structure and quality of the interface plays an important role toward the charge transfer from light-harvesting component to reaction sites, which also need to be rationally designed.

Moreover, for semiconductors with crystal facet characteristics, the facets that make up the surface and interface are key parameters to consider when optimizing surface and interface properties.[61,62] Researches on semiconductor crystal facet engineering have shown that photogenerated electrons and holes can be transferred to different crystal facets due to the self-induced internal electric fields.[63,64] Similar characteristics also exist in mBiVO$_4$, as demonstrated by Li and his group.[65] With $HAuCl_4$, H_2PtCl_6 and $AgNO_3$ as precursors, the metallic Ag, Au, and Pt were selectively deposited on the {010} facet, while PbO_2 and MnO_x particles were inclined to deposit on the {110} facet, indicating that photogenerated electrons and holes can participate in photocatalytic reduction on {010} facets and photocatalytic oxidation on {110} facets, respectively. A similar phenomenon also occurred in the deposition of dual precursors with simultaneous photoreduction and photooxidation. An efficient charge separation on adjacent crystal facets, {110} and {010} facet, resulted in more available photogenerated electrons and holes respectively participating in the redox reaction on different facets of mBiVO$_4$, thereby significantly improving the photocatalytic performance. Given that, the desired photocatalytic performance can be obtained by directionally designing the exposed facets of mBiVO$_4$, which can be achieved by controlling the process of crystal synthesis, as described below.

3. SYNTHETIC METHODS FOR FACET TAILOR OF *M*BIVO$_4$ BASED ON SURFACE AND INTERFACE DESIGN

It is well-known that crystal facet tailoring is an effective method for tuning/optimizing the photocatalytic performance of semiconductor materials. Adjusting the specific surface configuration and atomic structure enables effective regulations of the photocatalytic performance of different exposed facets. Research on the investigation of the relationship between the photocatalytic performance of mBiVO$_4$ and the crystal facets was first reported by Li and his research group.[66] With mBiVO$_4$ as a model catalyst, they confirmed that photogenerated electrons and holes can be effectively separated into the {010} and {110} facets of mBiVO$_4$, respectively.[67] Furthermore, on the basis of DFT calculation, they demonstrated that the {010} facet of mBiVO$_4$ exhibited higher activity owing to its higher charge carrier mobility, better water adsorption capacity, and lower overall energy potential for oxygen evolution. This landmark discovery provides new insights into the synthesis of highly efficient mBiVO$_4$ materials based on facet engineering for converting solar energy into chemical energy in the field of semiconductor physics and chemistry.

3.1. Facet Tailor on the Surface of *m*BiVO$_4$. For single mBiVO$_4$, the facet engineering mainly focuses on its surface. In general, exposed facets can be obtained in a semiconductor by selectively controlling the nucleation and growth rates in different directions during crystal growth, which is also referred to as the bottom-up route. In theory, a crystal preferentially maintains its lowest total surface energy. According to the Gibbs−Wulff theorem, the facets with higher surface energy grow rapidly and eventually vanish from the final crystals in the growth process, whereas the facets with lower surface energy grow slowly and are preserved to form the final crystal shape.[31] As a result, mBiVO$_4$ prepared under natural or equilibrium conditions normally exposes thermodynamically more stable facet rather than the highly active facet, which is detrimental to the conversion of solar energy. Therefore, facet engineering for the synthesis of mBiVO$_4$ with highly active facet exposure is still limited.

At present, the wet-chemistry routes (primarily solvothermal and hydrothermal) with the addition of solvent, capping agents or structure directing agents, are the most widely used methods for manipulating the nucleation and growth behaviors of mBiVO$_4$, especially growth rates along different orientations.[68,69] During solvothermal synthesis, the surface atomic arrangement and surface affinity of each orientation of the crystal for the solvent are different, the growth rates of the individual crystal facets are inconsistent and ultimately affect the final shape of the crystal. For instance, mBiVO$_4$ with a hierarchical structure oriented along the {040} facet was prepared through a template-free solvothermal route in an ethylene glycol (EG)/water mixed solution by adjusting the pH value of the precursor solution.[70] The formed BiVO$_4$ nanoparticles (NPs) were initially assembled into building blocks, followed by self-assembly through the Ostwald ripening process to form mBiVO$_4$ crystals oriented along the {040} facets. In this process, the adsorbed EG molecules acted as capping agent to decrease the growth rate and induced the oriented aggregation of the crystals.[71] The mBiVO$_4$ sample prepared at pH 5 with the highest intensity of highly active {040} facet exhibited the optimal photocatalytic performance for MB degradation due to more efficient charge separation and faster charge transfer. Likewise, nanostructured mBiVO$_4$ sheets with a highly exposed {010} facet were obtained through a solvothermal process using 15% glycerol as solvent and directing agent at pH 6.[72]

As mentioned before, the key to achieving selective exposure of the active facets is to change the relative stability of each facet during crystal growth. Some organic or inorganic

DOI: 10.1021/acscatal.9b03411
ACS Catal. 2020, 10, 1024−1059

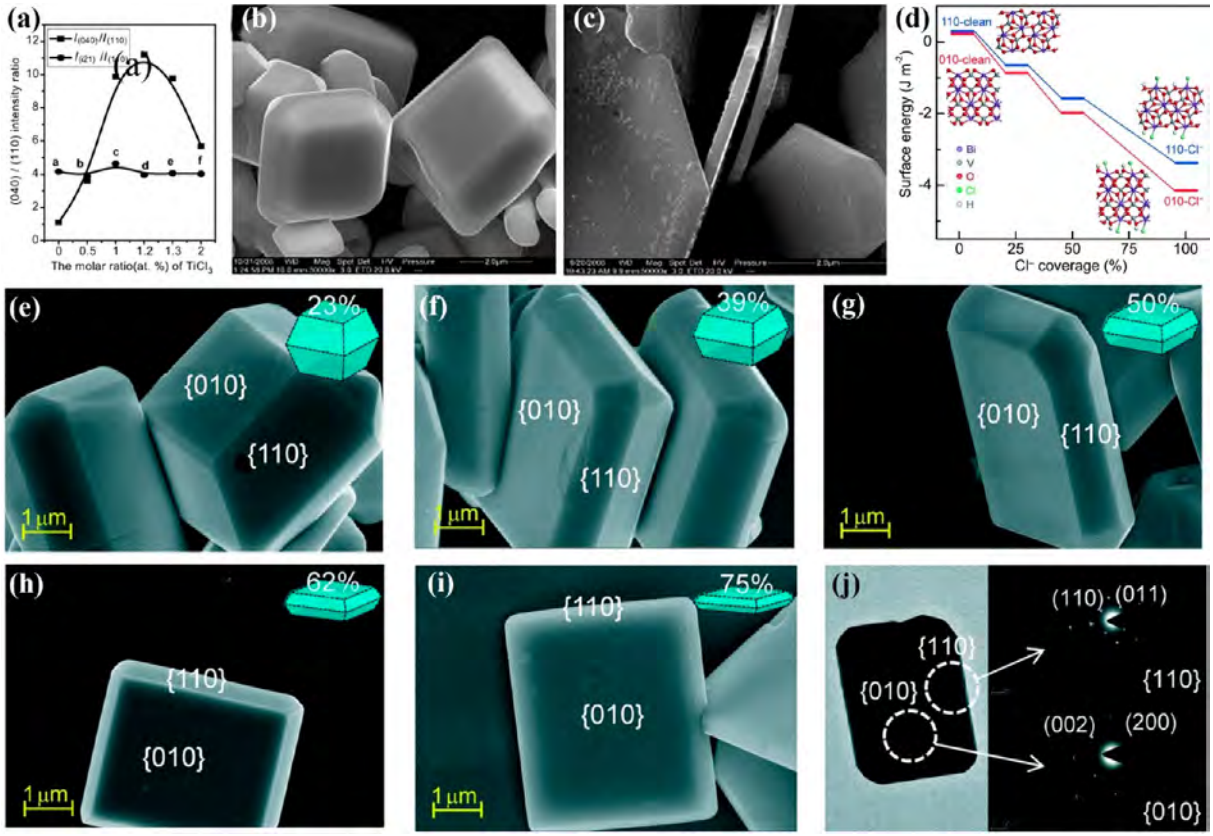

Figure 5. (a) Correlations of the Ti/Bi molar ratio with the intensity ratios of (040)/(110) and (121)/(110) in the XRD patterns of the corresponding $BiVO_4$ samples, and the intensity was normalized using the (110) diffraction peak as an internal standard. SEM images of samples of (b) $BiVO_4$ prepared without using the directing agent and (c) $BiVO_4$ prepared by the addition of the $TiCl_3$ directing agent. Reproduced with permission from ref 68. Copyright 2011 Wiley-VCH Verlag GmbH & Co. KGaA, Weinheim. (d) Effect of Cl^- coverage on the surface energies of {010} and {110} surfaces. SEM images: (e) $BiVO_4$–HT-23%, (f) $BiVO_4$–HT-39%, (g) $BiVO_4$–HT-50%, (h) $BiVO_4$–HT-62%, (i) $BiVO_4$–HT-75%, (j) TEM image of $BiVO_4$–HT-50% and SAED patterns of its {110} and {010} facets (HT represents hydrothermal treatment). Reproduced with permission from ref 75. Copyright 2017 Royal Society of Chemistry.

additives can be used as capping agents to selectively cover the facets with higher surface energies, which reduces the surface energy of materials with more active sites, thereby inhibiting the crystal growth along the corresponding direction. Therefore, the selective exposure of active facets can be delicately tailored by introducing the additives in the reaction medium. Up to now, an organic capping agent takes a dominant role in controlling the selective exposure of active facets of $m$$BiVO_4$ due to the diversity of organic molecules. For instance, Zhang et al. synthesized $m$$BiVO_4$ nanosheets that possessed a high percentage of individual facet on their top and bottom flat surfaces through hydrothermal method using sodium dodecyl benzenesulfonate (SDBS) as a facet-capping agent.[59] The {010} facet of $m$$BiVO_4$ with larger atom density than any other facets can provide more chances for sulfonic radicals absorption, which resulted in the preferred adsorption of SDBS on {010} facets, ultimately allowing the aggregation of the tetragonal $BiVO_4$ NPs to form $m$$BiVO_4$ nanosheets with exposed {010} facets. The electron diffraction pattern corresponding to the diffraction pattern of {010} zone axis, HR-TEM image, and the fast Fourier transform images all indicated the prepared $m$$BiVO_4$ with a preferred {010} surface facet. Meng et al. fabricated $m$$BiVO_4$ with well-defined morphologies by using triblock copolymer Pluronic P123 as surfactant and various bases as pH adjustor. The selective adsorption of P123 on the surface of the $BiVO_4$ nuclei reduced the surface energy, which decreased the growth rate of the crystal facets adsorbed with P123, thereby inducing compression along the axis perpendicular to these facets.[73]

Nonetheless, the photocatalytic performance of $m$$BiVO_4$ with selective exposure facets prepared by surfactant-assisted hydrothermal methods is still limited, as it is difficult to remove the surfactant molecules attached to the crystal structure of the $m$$BiVO_4$ photocatalyst during the synthesis, which is not conducive to the adsorption and activation of target reactant molecules, resulting in a failure to reliably evaluate the relationship between crystal facet and photocatalytic performance. In addition, such surfactant-assisted hydrothermal methods also increase the cost of material synthesis. On account of this, small inorganic ions, alternative to organic surfactants and ligands, can be used as facet-selective directing agent that not only allows the $m$$BiVO_4$ crystal to preferentially grow along the certain facet, but also is easier to be removed.[74] For instance, Wang et al. synthesized $m$$BiVO_4$ crystals preferential exposed to the (040) surface corresponding to {010} facet by adding trace amounts of $TiCl_3$ as a directing agent in an inorganic solution under hydrothermal treatment for 24 h and then calcined at 673 K for 2 h.[68] The X-ray diffraction (XRD) pattern of the as-prepared $m$$BiVO_4$ sample showed that the intensity of (040) diffraction peak became stronger with the increase of the directing agent $TiCl_3$, suggesting that $TiCl_3$ can induce the orientation growth of

DOI: 10.1021/acscatal.9b03411
ACS Catal. 2020, 10, 1024−1059

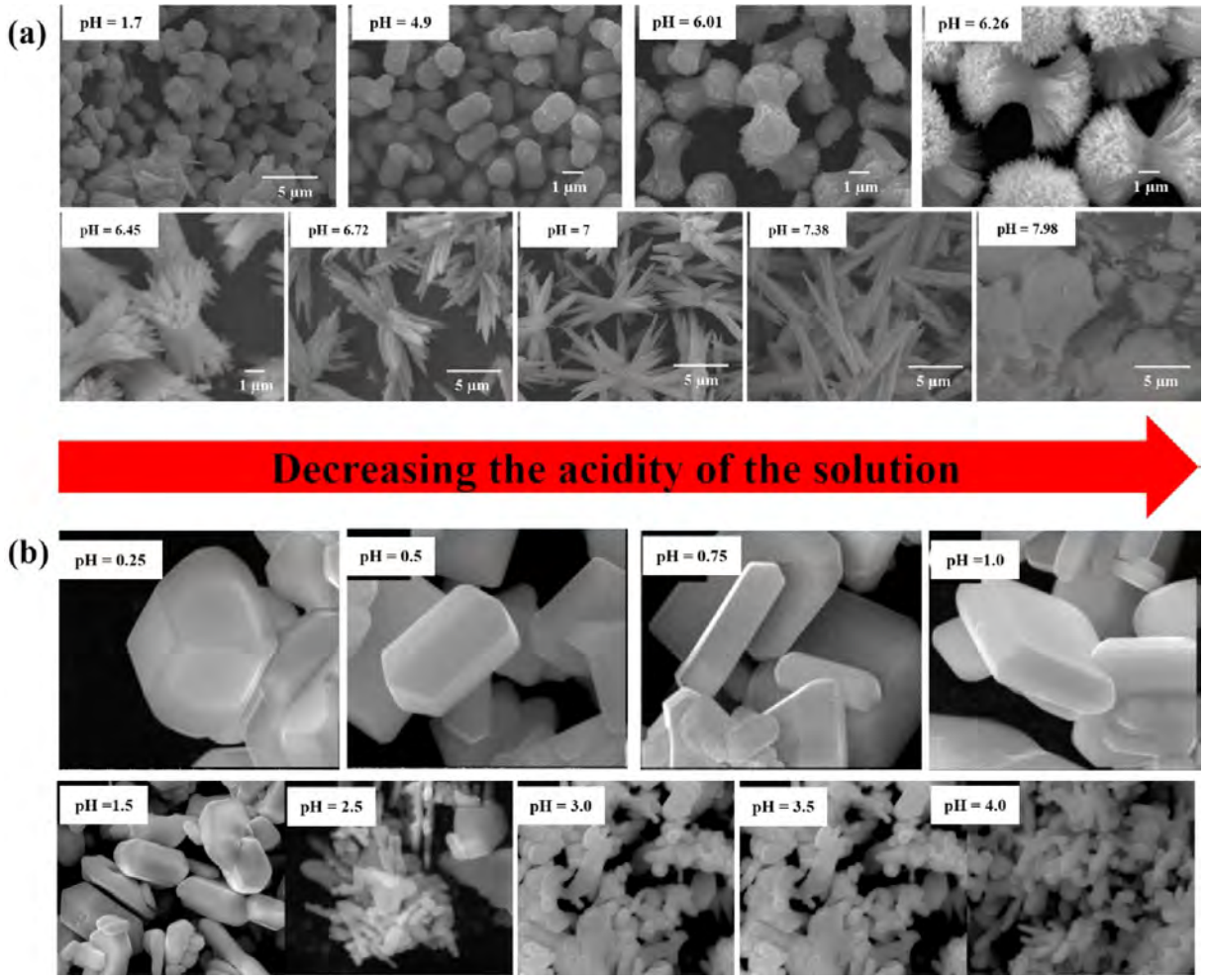

Figure 6. (a) SEM images of different shaped $BiVO_4$ hierarchical structures obtained at pH values of 1.7, 4.9, 6.01, 6.26, 6.45, 6.72, 7, 7.38, and 7.98, respectively. Reproduced with permission from ref 79. Copyright 2014 Elsevier. (b) SEM images of the *m*$BiVO_4$ prepared by hydrothermal method under pH = 0.25, 0.5, 0.75, 1.0, 1.5, 2.5, 3.0, 3.5, 4.0. Reproduced with permission from ref 81. Copyright 2017 American Chemical Society.

m$BiVO_4$ crystal preferentially along the {010} facet (Figure 5a). Scanning electron microscopy (SEM) images of *m*$BiVO_4$ showed that single *m*$BiVO_4$ had a smooth surface and was a regular decagon with high crystallization, with less {010} facet exposure in the absence of a directing agent (Figure 5b). Whereas the sheet-like morphology with the average thickness of 260 nm was obtained in the presence of a directing agent, which possessed a higher percentage of {010} facet on their top and bottom flat surfaces (Figure 5c). Further research on the synthesis *m*$BiVO_4$ using NaCl as directing agents further demonstrated that Cl^- played a critical role in controlling the exposure ratio of {010} to {110} facets.[75] They found that the use of KCl, $CaCl_2$, $ZnCl_2$, and $AlCl_3$ instead of NaCl as an additive also resulted in a uniform truncated tetragonal bipyramidal morphology, the employment of NaF, NaBr, NaI, and Na_2SO_4 to replace NaCl led to the generation of an irregular morphology of $BiVO_4$ particles. DFT calculation showed that the addition of Cl^- would result in a more significant decrease in the surface energy of the {010} facet as compared to that of the {110} facet (Figure 5d). As a result, the exposure area of {010} facet increased as the concentration of Cl^- increased (Figure 5e–j). In addition, Thalluri et al. prepared *m*$BiVO_4$ with the {040} facet preferential orientation through hydrothermal reaction using ammonium carbonate as a structure directing agent at 180 °C.[76] The XRD pattern of *m*$BiVO_4$ demonstrated that the addition of ammonium carbonate facilitated the exposure of the {040} facet at high pH, which increased the percentage of V^{4+}. More recently, amino acids have been employed as inducers to induce and regulate the growth of some materials due to their effective influence on the size and shape of inorganic materials.[77] Inspired by this, Wang et al. prepared *m*$BiVO_4$ with a preferential {040} facet orientation through hydrothermal process using amino acids as morphology-directing agents, the highest peak intensity corresponding to the {040} facet was presented at the hydrothermal temperature of 180 °C.[78]

However, for thermodynamically disfavored surface facets, kinetic control is another universal approach that takes into account the stability and the relative growth rate of the facet.[79] These methods are mainly the assembly of atoms into crystals, representing a bottom-up approach to facet engineering. For instance, various *m*$BiVO_4$ samples with {001} facet exposure were prepared by Xi and Ye through a facial hydrothermal route without adding surfactant at pH values ranging from 1.0 to 7.0, in which the pH played a significant role to the formation of *m*$BiVO_4$ samples.[80] An increased pH accelerated the hydrolysis of $BiCl_3$ to poorly soluble BiOCl, resulting in a low concentration of the free Bi^{3+} ions in the solution, which slowed the nucleation of *m*$BiVO_4$ crystals and eventually formed a series of products deviating from the thermodynamic

DOI: 10.1021/acscatal.9b03411
ACS Catal. 2020, 10, 1024–1059

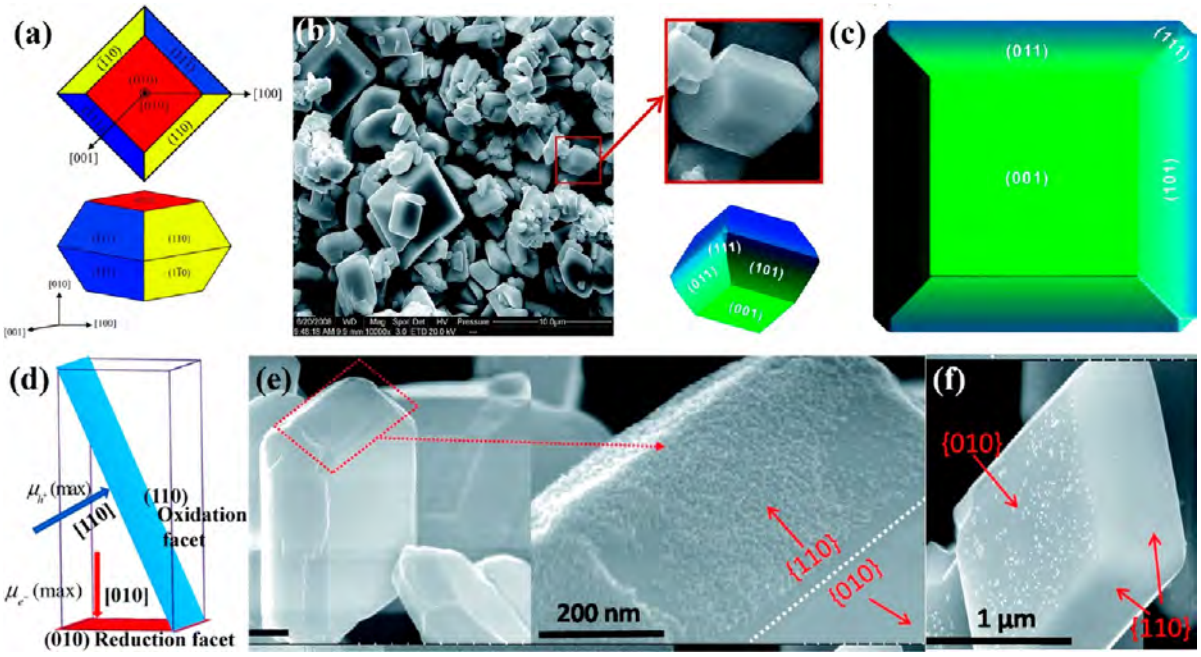

Figure 7. (a) Equilibrium shape of a $BiVO_4$ crystal in the monoclinic clinobisvanite phase, according to the Wulff construction and the calculated surface energy: Top view, and perspective view. Reproduced with permission from ref 83. Copyright 2011 Royal Society of Chemistry. Equilibrium morphology of m-$BiVO_4$ (b) The SEM image, (c) prediction. Reproduced with permission from ref 84. Copyright 2017 Royal Society of Chemistry. (d) Electron (or hole) transfer paths along the crystal axis [*hkl*] and the corresponding facet (*hkl*). Reproduced with permission from ref 66. Copyright 2015 Royal Society of Chemistry. (e) SEM images of CoO_x deposited on {110} facets of $BiVO_4$ by photo-oxidation deposition. (f) SEM image of Pt as the reduction cocatalyst deposited on {010} facets of $BiVO_4$. Reproduced with permission from ref 85. Copyright 2014 Royal Society of Chemistry.

shape. Therefore, *m*$BiVO_4$ nanoplates with highly anisotropic structures can only be synthesized by carefully controlling nucleation kinetics, and a relative strong 004 diffraction peak indicated a preferred orientation along the {001} facet. Based on a similar pH-dependent crystal growth mechanism, Dong et al. reported that the dominated facet of the prepared *m*$BiVO_4$ evolved from {040} to {110} with the decrease of the acidity of the precursor (Figure 6a).[79] As a result, the samples obtained at pH 6.26 with highly anisotropic particle growth and optimal hierarchical structure exhibited the highest photocatalytic performance for RhB degradation. Moreover, Zhao et al. prepared *m*$BiVO_4$ catalysts with different facet exposure by controlling the pH values of the solution during hydrothermal treatment (Figure 6b).[81] These various morphologies were attributed to the fact that the pH of the solution can influence the kinetics of the recrystallization reaction by controlling the saturation of the reactants and the structure of the growth units, thereby further determining the morphology of the crystal. Moreover, *m*$BiVO_4$ with different relative exposure ratio of {010} to {110} facet was prepared by adjusting the concentration of nitric acid.[82] The results showed that the exposure ratio of {010} to {110} facet increased with the decrease of nitric acid concentration.

To sum up, different facets of *m*$BiVO_4$ have varied electronic structures due to distinct atomic arrangements and terminations, which results in the different properties of crystal facets in the adsorption of reactant molecules, the transfer of the photogenerated carriers, and the desorption of product molecules in the photocatalytic reaction process. Therefore, the reactive performance of a given photocatalyst sensitively varies on the exposed crystal facets. Of note, despite many reports of successful synthesis and some quantitative efforts to understand them, current studies have neither determined whether the active crystal facet is highly exposed nor clarified the mechanism by which high active crystal facet preferentially grow. Therefore, it is still a challenge to predict the outcome of the chemical synthesis of *m*$BiVO_4$. Major challenges include understanding the complex chemistry involved in the reduction of metal salt, how metal atoms and ions nucleate seeds, and how seeds grow into well-defined shapes, possibly with the help of solution-phase additives called capping agents or structure-directing agents. Given that, the theoretical prediction on the exposed facets of *m*$BiVO_4$, especially those related to photocatalytic performance, are critical to the microscopic mechanism of experimental observation.

One of the early theoretical investigations with respect to the surface energy of several low-index by DFT calculation showed that only three facets with lower surface energies, ({010}, {110}, and {111} facet), were exposed to the vacuum, which resulted in the prepared *m*$BiVO_4$ exhibited a truncated regular octahedron (Figure 7a).[83] This calculated result was in agreement with the SEM image of the experimentally synthesized *m*$BiVO_4$ (Figure 5b,c).[68] Li et al. predicted the equilibrium morphology of *m*$BiVO_4$, a corner-cut truncated bipyramid with {001}, {101}, {011}, and {111} facet exposed, based on the surface energies calculation by Wulff construction (Figure 7c). This model prediction was almost identical to the experimental results (Figure 7b),[84] and the existence of {111} facet for real crystals of *m*$BiVO_4$ was demonstrated compared with the morphology predicted by Zhao and co-worker. Moreover, Yang et al. applied the GGA-PBE to calculate the band structures of {010} and {110} facet according to the orbital curvature of the CB minimum (CBM) and VBM, and the results showed that the {010} facet exhibited a higher

DOI: 10.1021/acscatal.9b03411
ACS Catal. 2020, 10, 1024−1059

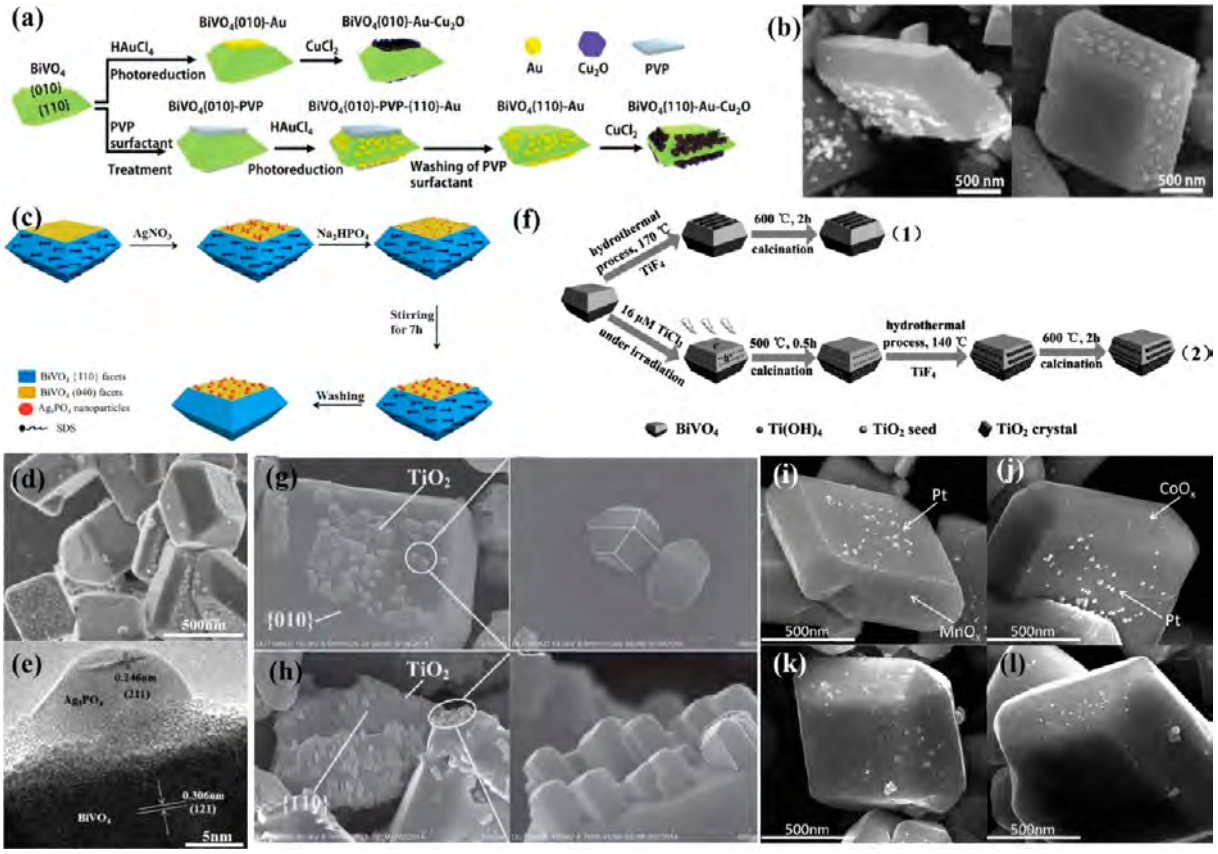

Figure 8. (a) Schematic illustration of the synthetic process for the $BiVO_4$-based heterostructures. (b) SEM images of the as-synthesized $BiVO_4${010}-Au and $BiVO_4${110}-Au. Reproduced with permission from ref 90. Copyright 2018 Wiley-VCH Verlag GmbH & Co. KGaA, Weinheim. (c) Schematic diagram for the formation process of $Ag_3PO_4/BiVO_4$ heterojunction photocatalyst with Ag_3PO_4 nanoparticles selectively deposited on $BiVO_4$ facets. (d) FE-SEM image of $Ag_3PO_4/BiVO_4$. (e) HR-TEM image of the $Ag_3PO_4/BiVO_4$ photocatalyst. Reproduced with permission from ref 91. Copyright 2013 Wiley-VCH Verlag GmbH & Co. KGaA, Weinheim. (f) Schematic illustration of the process to prepare $BiVO_4$-010-TiO_2 heterojunction (1) and $BiVO_4$-110-TiO_2 heterojunction (2). (g) SEM images of $BiVO_4$-010-TiO_2 heterojunction (TiO_2 grown on the {010} facet of $BiVO_4$). (h) SEM images of $BiVO_4$-110-TiO_2 heterojunction (TiO_2 grown on the {110} facet of $BiVO_4$). Reproduced with permission from ref 92. Copyright 2015 Wiley-VCH Verlag GmbH & Co. KGaA, Weinheim. SEM images of Pt/MnO_x/$BiVO_4$ and Pt/Co_3O_4/$BiVO_4$ dual-cocatalyst systems prepared by photodeposition and impregnation methods: (i) Pt (P.D.)/MnO_x (P.D.)/$BiVO_4$; (j) Pt (P.D.)/Co_3O_4 (P.D.)/$BiVO_4$; (k) Pt (imp)/MnO_x (imp)/$BiVO_4$ and (l) Pt (imp)/Co_3O_4 (imp)/$BiVO_4$. Reproduced with permission from ref 85. Copyright 2014 Royal Society of Chemistry.

charge carriers mobility.[67] Based on Marcus-EHAM theory, Liu et al. combined DFT+U method with a small polaron model to calculate the carrier mobility and hopping activation energy in seven low-index facets of *m*$BiVO_4$. They proposed that the electron/hole mobility along the crystal axis [*hkl*] could essentially determine the ability of gathering electron/hole for the corresponding crystal facet {*hkl*}(Figure 7d).[66] This prediction was validated by Li et al., in which metals as reduction cocatalysts tended to deposition on the {010} facet of *m*$BiVO_4$, while metal oxides as oxidation cocatalysts tend to deposition on the {110} facet (Figure 7e,f).[85]

3.2. Facet Tailor at the Interface of *m*$BiVO_4$-Based Composites. For *m*$BiVO_4$-based composites, the facet engineering with respect to tailor the exposed facets of *m*$BiVO_4$ is more complicated because of the complexity of hybrid structures. The coupling of different components to form a hybrid structure necessarily results in the generation of an interface that is the location for charge carriers pass through, and a high efficiency of charge carriers across the interface can greatly prevent the charge recombination. Therefore, the focus of interface design of *m*$BiVO_4$-based composites is to adjust the facets through controlled synthesis for improving charge transfer efficiency and for reducing recombination loss.

In terms of interface engineering, selective growth or deposition are rather important, which can make use of different wetting abilities of new components on the surface of existing components. The interfacial wetting of components is an important factor that has to be taken into account. In general, to minimize interfacial energy, the newly formed materials tend to deposit on better wetted surface, such as the surface with the same crystalline phase, small lattice mismatch, similar composition, and/or consistent hydrophilicity/hydrophobicity, as well as that having strong chemical interactions or chemical bonding with the new component.[86] The wetting process is typically controlled by two growth models, namely, epitaxial growth and nonepitaxial growth, and self-assembly methods.

In the epitaxial growth model, the surface of the existing component provides sites for the growth of the new component, and the formation of the new component will minimize the lattice mismatch with the existing component to reduce the interfacial energy, which greatly lowers the flexibility in changing the interfacial facets.[87] Therefore, the

DOI: 10.1021/acscatal.9b03411
ACS Catal. 2020, 10, 1024−1059

control of the interfacial facet is mainly achieved on some facets of semiconductor by self-assembly or nonepitaxial methods. Example such as the pear-shaped mBiVO$_4$/BiPO$_4$ composite was successfully fabricated by an oriented self-assembly process, followed by Ostwald ripening.[88] Bi^{3+} ions tend to precipitate with VO_4^{3-} and PO_4^{3-} in the precipitation process, followed by mBiVO$_4$ and BiPO$_4$ assembled themselves into loose pear-shaped structure in order to reduce the high surface energy originated from undesired bonds. The mBiVO$_4$/BiPO$_4$ composite with oriented exposed {040} facet provided more multiatomic BiV_4 centers, which were the origin of multielectron transfer and functioned as active sites in the subsequent photocatalytic reactions. Additionally, the negatively charged PO_4^{3-} was more likely to trap holes but repel electrons, which significantly facilitated the separation of photogenerated electrons and holes, thereby resulting in improved photocatalytic performance. Likewise, mBiVO$_4$ with high activity {040} facet exposure was completely covered by the thin rGO sheets by an evaporation-induced self-assembly method.[89] The exposed high-active {040} facets maximizing the coupling interface between mBiVO$_4$ and rGO also promoted the electrons transfer across the contact interface, thereby enhancing the photocatalytic efficiency for MB degradation.

Similar to surface design, the use of capping agents is also applied to engineer interface structures. The capping agents are selectively adsorbed to the specific facets, which prevents the further growth of a second component on the capped facets. As a result, an interface is selectively generated between the newly formed component and the uncovered facets. For example, Au NPs was reduced on the electron-deficient {110} facet of truncated octahedron mBiVO$_4$ crystals with polyvinylpyrrolidone (PVP) as a capping agent (Figure 8a).[90] The PVP preferentially adsorbed to the {010} facet of mBiVO$_4$, which effectively inhibited the nucleation of Au NPs on the {010} facet, thus forming the mBiVO$_4${110}-Au interface. Whereas in the absence of PVP, Au NPs were selectively deposited on the {010} facet with $HAuCl_4{\cdot}4H_2O$ as a precursor due to the accumulation of photogenerated electrons on the {010} facet (Figure 8b). Likewise, Ag_3PO_4 NPs were selectively deposited on the {040} facet of truncated bipyramid mBiVO$_4$ semiconductors using sodium dodecyl sulfate (SDS) as a capping agent (Figure 8c).[91] The preferential adsorption of SDS to {110} facet occupies the adsorption sites of Ag^+ species, while {110} facet with low-coordinated oxygen atoms provides sufficient binding sites to anchor Ag^+, and as such, a mBiVO$_4${040}-Ag_3PO_4 interface was rationally formed (Figure 8d,e). Based on a similar mechanism, the TiO_2 crystal prepared with TiF_4 as a precursor was preferentially grown on the {010} facet of mBiVO$_4$ since {010} facet can provide enough binding sites to anchor Ti^{4+} (Figure 8f,g).[92] Conversely, the nucleation of TiO_2 crystal on the {110} facet of mBiVO$_4$ was hampered due to a relatively large d-value mismatch. Therefore, a seeding process for first oxidizing Ti^{3+} to Ti^{4+} on the {110} facet of mBiVO$_4$ and then calcining at 500 °C to form TiO_2 seeds was proposed prior to followed treatment similar to the preparation of mBiVO$_4$-010-TiO_2 (Figure 8f,h).

Given the adverse effects of the capping agent remaining on the surface of catalyst on the photocatalytic performance, facet-dependent photodeposition, an alternative method to the formation of facet-selective interface, has been extensively investigated. As demonstrated by Li and his group, the difference in energy band between adjacent facets of mBiVO$_4$ semiconductor caused photogenerated electrons and holes to accumulate on different facets, respectively, which provides a driving force for selective deposition of new components on the facets through reduction or oxidation reactions. For example, Pt NPs and MnO_x (Co_3O_4) species can be selectively deposited on the surface of mBiVO$_4$ through a photodeposition approach.[85] As both the CB and VB edges potential of mBiVO$_4${010} facet were more negative than that of {110} facet, the photogenerated electrons and holes were accumulated on the {010} and {110} facet, respectively. The photoreduction of $PtCl_6^-$ occurred on the {010} facet of mBiVO$_4$ to generate a mBiVO$_4${010}-Pt interface (Figure 8i), while the oxidation occurred on the {110} facet to form a mBiVO$_4${110}-MnO_x (Co_3O_4) interface (Figure 8j) in the photodeposition process. Conversely, Pt NPs and MnO_x (Co_3O_4) species loaded by the impregnation method were randomly deposited on all facets of mBiVO$_4$ (Figure 8k,l). Likewise, Chen et al. prepared the Ag@AgBr/BiVO$_4$/Co_3O_4 composite by sequential deposition of Ag@AgBr and Co_3O_4 on the {010} and {110} facet of mBiVO$_4$.[93]

On the basis of the above analysis, the advanced synthesis methods for micro and nanomaterials with well-defined facets have greatly advanced the process of surface as well as interface control of mBiVO$_4$ based on facet engineering. However, in order to precisely control the exposed facet of mBiVO$_4$ to accurately evaluate facet-dependent photocatalytic performance and investigate catalytic mechanisms, both the intrinsic correlation between surface and interface, and the relationship between structural features and functions should also be highly reasonable.

4. FACET ENGINEERING ON THE SURFCAE OF *M*BIVO$_4$

For monocomponent semiconductor photocatalyst, the facets that make up the surface of the semiconductor are key parameters that should be rationally designed, which mainly influences the photocatalytic performance of the materials from the following three mechanisms. First of all, the atomic arrangements occurring on the surface of the catalyst directly determine the amount of adsorption and activation of the reactants, thereby affecting the photocatalytic activity and selectivity. Moreover, the surface electronic band structures determined by the surface facets can provide redox reaction sites for photogenerated charge carriers. Finally, crystal orientation growth determines the efficiency of charge separation and transfer, which further affects the density of available photogenerated electrons and holes that directly participate in the redox reactions occurring at the surface of the catalyst. Furthermore, photogenerated electrons and holes can spontaneously accumulate on different facets of semiconductor due to the existence of thermodynamically favorable spatial charge separation and then participate in the surface redox reaction therein. On the grounds of above analysis, the target of the facet engineering of single mBiVO$_4$ is to rationally tailor the surface facets by various approaches to obtain an optimal photocatalytic performance.

4.1. Selective Exposure of Surface Facets with High Photocatalytic Activity. Because of the difference in electronic structure and surface energy, the ability of different facets to the adsorption and activation of reactant molecules is different. Fully investigating the surface activity of different facets helps to selectively promote the growth of highly active

DOI: 10.1021/acscatal.9b03411
ACS Catal. 2020, 10, 1024−1059

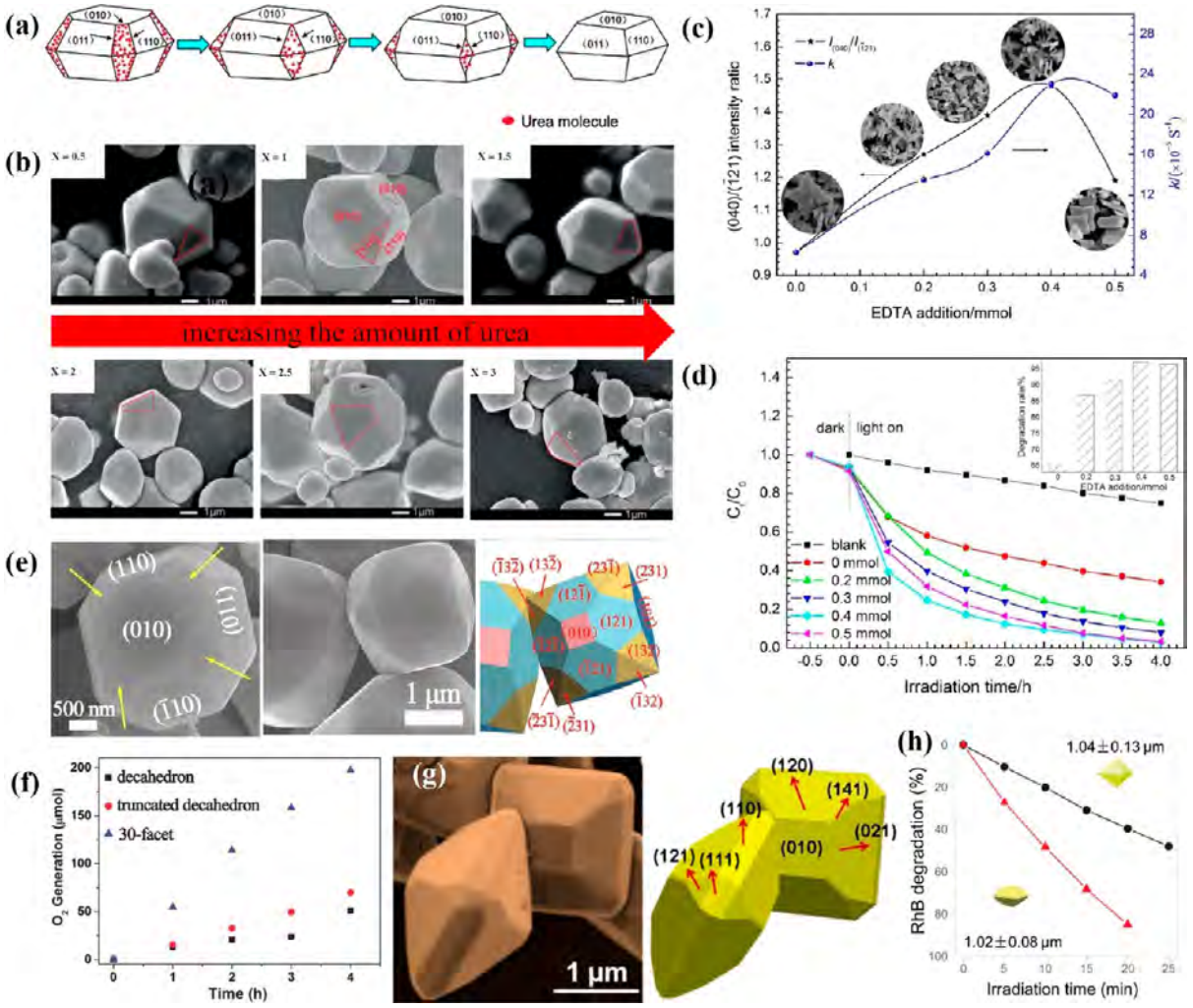

Figure 9. (a) Formation mechanism of the {111} facets of OD-$BiVO_4$. (b) SEM images of OD-$BiVO_4$-X (X denotes the amount of urea used): X = 0.5, 1, 1.5, 2, 2.5, 3. Reproduced with permission from ref 94. 2017 Wiley-VCH Verlag GmbH & Co. KGaA, Weinheim. (c) Relationship between the addition amount of EDTA and the morphology, $I_{(040)}/I_{(121)}$ intensity ratio, and photocatalytic performance (k) of different $BiVO_4$ samples. (d) Photocatalytic degradation of MB without photocatalysts and using the $BiVO_4$ samples obtained by a solvothermal process with the addition of EDTA as photocatalysts. Reproduced from ref 96. 2018 Royal Society of Chemistry. (e) FE-SEM images and the corresponding schematic illustration of the 30-faceted $BiVO_4$ polyhedra. (f) Time courses of photocatalytic O_2 generation over the decahedron, truncated decahedron, and 30-faceted $BiVO_4$ polyhedron. Reproduced with permission from ref 98. 2017 Wiley-VCH Verlag GmbH & Co. KGaA, Weinheim. (g) SEM image of the obtained $BiVO_4$ microcrystals enclosed with many facets and simulated BiVO4 crystals with the facet indexes labeled. (h) Photo degradation of RhB with the roughly 1 μm sized octahedral-shaped (black) and 42-faceted (red) $BiVO_4$ crystals as photocatalysts. Reproduced with permission from ref 100. Copyright 2019 Elsevier.

facets while suppressing undesired facet exposure by controlling the crystal growth environment.

In terms of material synthesis, some inorganic ions or organic molecules tend to selectively adsorb on the high-energy facets of the semiconductor to lower the surface energy, and these molecules can act as director to induce the growth of the semiconductor along a particular crystal facet. For instance, the surface facet exposure of octadecahedron-$BiVO_4$ (OD-$BiVO_4$) can be precisely controlled through altering the amount of added urea.[94] The urea molecules preferentially adsorbed on the {111} facet, which suppressed the growth of other facets (Figure 9a). As a result, the prepared $m$$BiVO_4$ catalyst exhibited a typical decahedron shape with {010}, {011}, and {110} facets exposure in the absence of urea, while a new {111} facet was gradually generated in the presence of urea, and the areas of {111} facet showed a slight increase as the amount of urea increased (Figure 9b). The photocatalytic performance for RhB degradation showed that the degradation efficiency decreased with the increase of urea, suggesting that the {111} facet was not conducive to the improvement of photocatalytic activity. In view of this, by controlling the added urea at a low level, the optimal photocatalytic performance can be obtained. Another example, the H^+ preferentially adsorbed on {010} facets of $m$$BiVO_4$ to reduce the surface energy, which reduce the reactivity and growth rate of the high-energy {010} facet, remaining the {010} facet as the final morphology.[95] Since the BiV_4 multiatomic center in the {010} facet of $m$$BiVO_4$ makes it easier to interact with the electron donor, the oxygen atom in the hydroxyl group of Gly was more likely to adsorb on the {010} facet, thereby directionally inducing the growth of $m$$BiVO_4$ along the {010} facet.[96] Likewise, the −COOH (or $-NH_2$) of the amino acids adsorbed on the surface of $m$$BiVO_4$ would induce the crystal growth along the {040} facet.[78]

DOI: 10.1021/acscatal.9b03411
ACS Catal. 2020, 10, 1024−1059

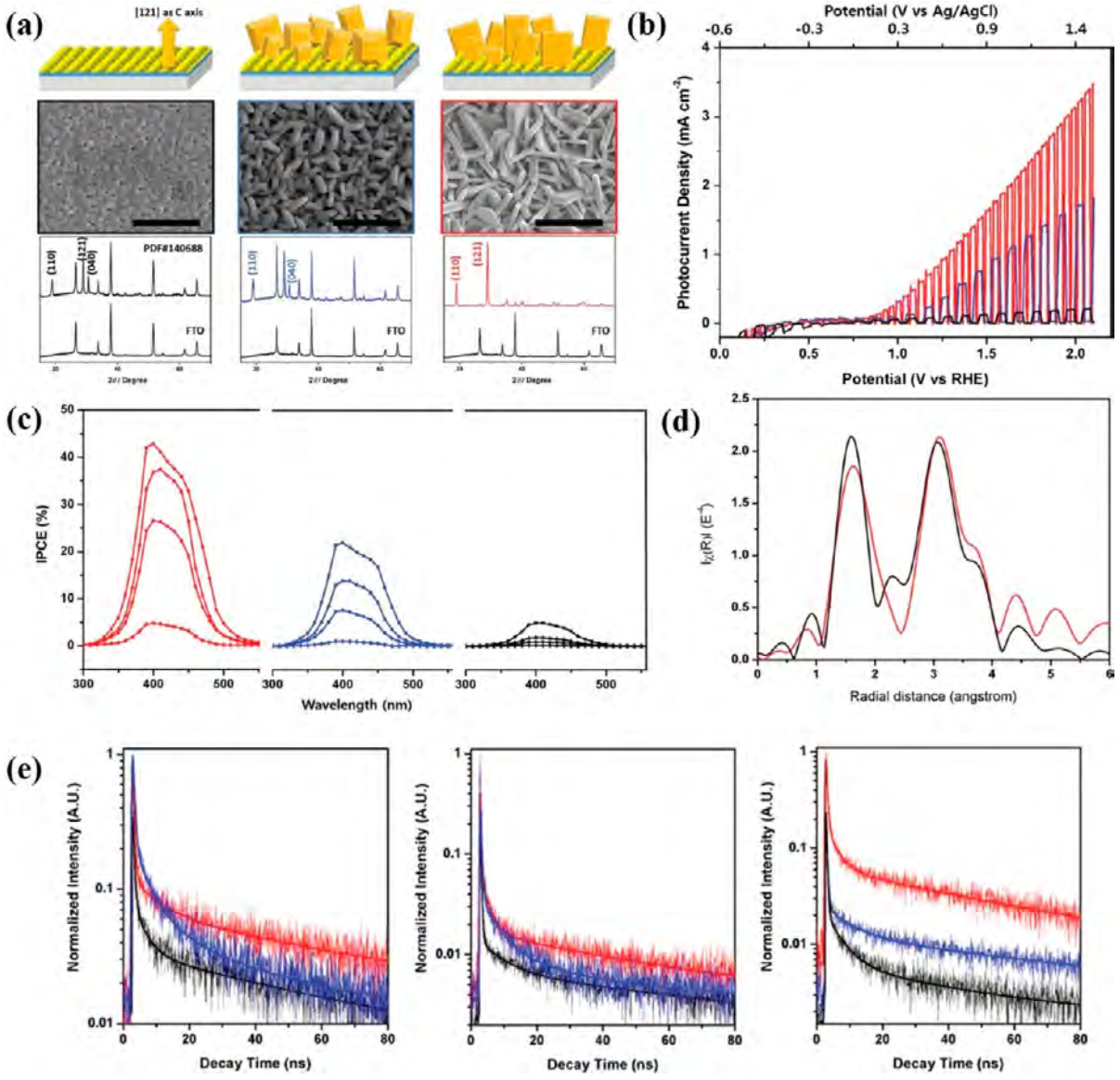

Figure 10. (a) Scheme of the top-viewed FESEM images and XRD pattern of the SL-BVO, PF-BVO and (040)-BVO. PEC characteristics and H_2/O_2 evolution measurement as a function of bias: (b) $I-V$ curves, (c) IPCE of the SL-BVO (black), PF-BVO (blue), and (040)-BVO (red). (d) EXAFS of a single individual plate of the (040) facet engineered $BiVO_4$ film (dark condition; black, illumination, red). (e) TRPL of the $BiVO_4$ seed layer (black), $BiVO_4$ plate film (blue), and (040) facet engineered $BiVO_4$ film (red). Transient emission observed at 406, 550, and 600 nm at an excitation of 375 nm at room temperature. Reproduced with permission from ref 101. Copyright 2015 Wiley-VCH Verlag GmbH & Co. KGaA, Weinheim.

In terms of photocatalytic reaction, the adsorption efficiency of the reactant molecules on the surface of the catalyst determines the amount of molecules available for subsequent participation in the surface redox reaction. Hence, the efficient adsorption of reactant molecules on the surface facilitates the enhancement of photocatalytic activity. For instance, Ravidhas et al. reported the highly oriented {040} facet had a relatively high specific surface area and a larger atom density to adsorb more dye molecules on the surface of $m$$BiVO_4$, resulting in an enhanced photocatalytic performance for RhB degradation.[97] Thalluri et al. reported that the highly exposed {040} facet increased the O−H species that directly participated in the adsorption of ethylene on the surface of $m$$BiVO_4$ catalyst as well as the generation of hydroxyl radicals, thereby significantly improving the photocatalytic performance.[76]

In addition to the difference in molecular adsorption associated with surface facets, the separation and transfer of photogenerated charge carriers is also related to the physicochemical properties and surface states of the faceted semiconductors, which is another factor that can affect the photocatalytic activity. Since only when photogenerated carriers are transferred to the surface of the catalyst to participate in the surface reaction before recombination can lead to an increase in photocatalytic activity, a short charge transfer distance is favorable. Hence, the construction of nanostructured $m$$BiVO_4$ with optimized microtopography, especially two-dimensional (2D) laminar structured to shorten the transfer distance of photogenerated charge carriers to the surface, and preferential exposure to highly active facets would be an effective way to promote the charge separation. Example such as shuriken-like $m$$BiVO_4$ with exposed {010} facet were

DOI: 10.1021/acscatal.9b03411
ACS Catal. 2020, 10, 1024−1059

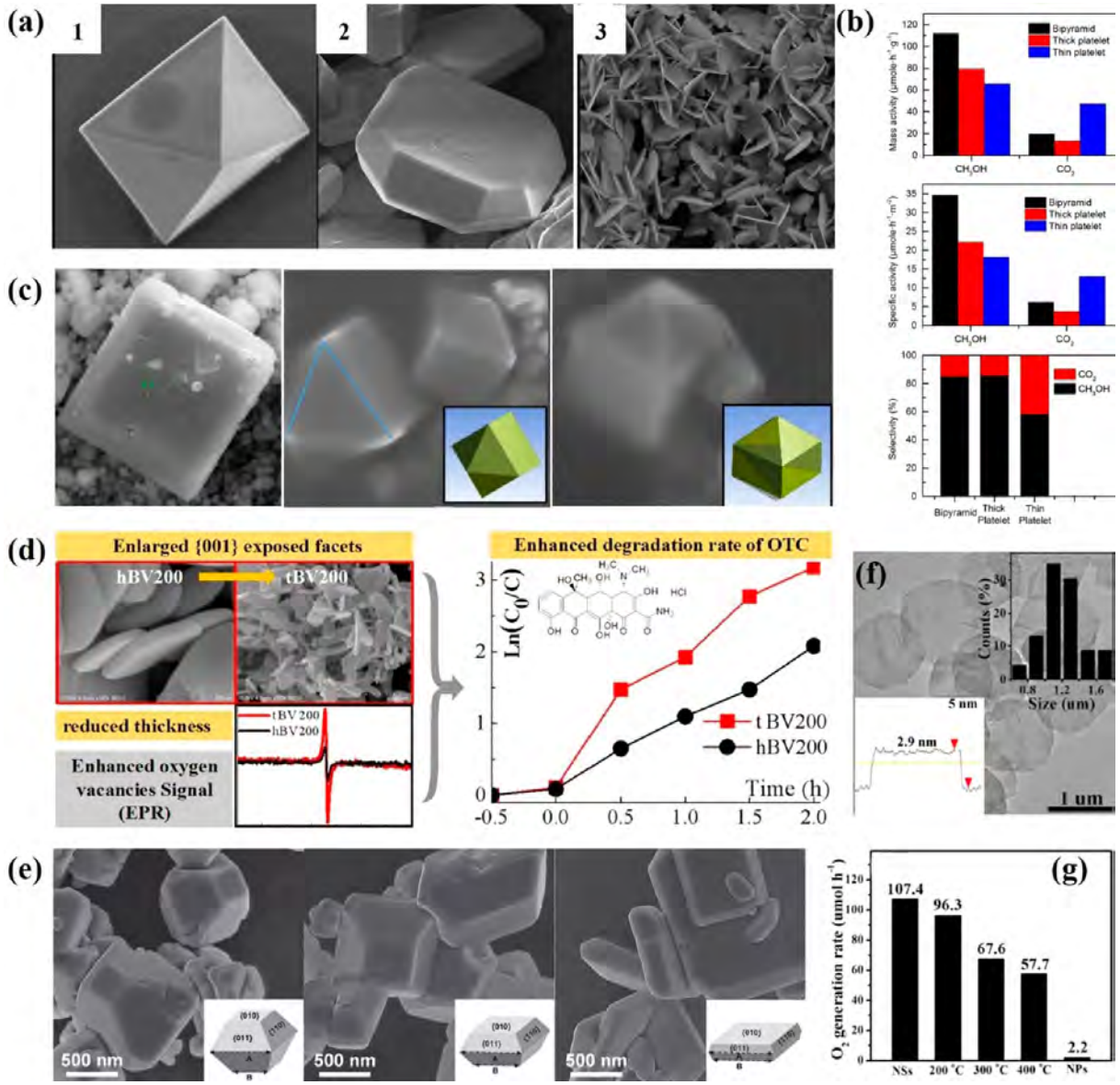

Figure 11. (a) High magnification images of $BiVO_4$ (1) bipyramid, (2) thick platelets, (3) thin platelets. (b) Mass activity for the conversion of CH_4 to CH_3OH and CO_2 measured for different $BiVO_4$ morphologies after 60 min of reaction, the specific activity for the same samples using the BET method to measure the surface area for powders of each sample, and the selectivity for producing CH_3OH and CO_2 after 60 min of reaction for the same samples. Reproduced with permission from ref 104. Copyright 2018 American Chemical Society. (c) SEM images of the decahedron $BiVO_4$ prepared by high-temperature hydrothermal procedure, the dodecahedron $Bi_{0.3}Y_{0.7}VO_4$ prepared by low-temperature hydrothermal method. Reproduced with permission from ref 105. Copyright 2017 Elsevier. (d) The relationship between morphology and surface OVs and corresponding photocatalytic performance for tBV200 and hBV200. Reproduced with permission from ref 106. Copyright 2018 Elsevier. (e) SEM images of $BiVO_4$ prepared using different concentrations of nitric acid as the reaction medium: (a) 1.00 M, (b) 0.75 M, and (c) 0.50 M. The insets present the schematic morphology of each $BiVO_4$ with the assigned {010} and {110} facets. Reproduced with permission from ref 82. Copyright 2016 Wiley-VCH Verlag GmbH & Co. KGaA, Weinheim. (f) TEM image of ultrathin 2D $BiVO_4$ NSs. (g) O_2 generation rates of $BiVO_4$ NSs, $BiVO_4$ NPs, and $BiVO_4$ NSs after annealed at different temperatures in air in $AgNO_3$ aqueous solution (50 mM). Reproduced with permission from ref 110. Copyright 2018 American Chemical Society.

prepared using ethylenediamine tetraacetic acid disodium (EDTA) as a structure-directing agent.[96] When the amount of EDTA added was in the range of 0.2 to 0.4 mmol, the aggregation of *m*$BiVO_4$ nanocrystals simultaneously occurred along two axes perpendicular to each other, and finally large number of swords with a 2D layered morphology were formed by self-assembly (Figure 9c). Such inorganic superstructure agglomerates not only retain the advantages of building blocks with shorter charge transport paths but also obtain photogenerated electrons and holes with long lifetime and high transfer rate. Therefore, *m*$BiVO_4$ samples with the highest exposed degree of {040} facet and shuriken-like shape at the optimum addition amount of EDTA exhibited the best photocatalytic performance for MB degradation (Figure 9d).

After the available photogenerated electrons and/or holes reach the surface of the catalyst, the final step in determining the photocatalytic activity is the surface reaction efficiency. Since high-index facets have a high density of low-coordinated atoms, including steps, edges, and kinks that can be used as highly active catalytic sites, semiconductors with exposure of

DOI: 10.1021/acscatal.9b03411
ACS Catal. 2020, 10, 1024−1059

high-index facets can obtain more highly active sites for chemical reactions. Inspired by this, the synthesis of mBiVO$_4$ with high-index facets exposure is a fantastic method to obtain improved photocatalytic performance. For instance, with the photocatalytic oxygen evolution as a reaction model, the photocatalytic performance of 30-faceted BiVO$_4$ polyhedron enclosed by high-index {132}, {321}, and {121} facets was much higher than that of decahedral BiVO$_4$ and truncated decahedral BiVO$_4$ (Figure 9e,f).[98] This enhanced photocatalytic performance was attributed to the fact that the overpotential for oxygen evolution reaction on high-index facets was about 0.77−1.14 V less than that of on the low-index surfaces, and the high-index facets were energetically favorable for water dissociation. Likewise, 24-faceted concave BiVO$_4$ with exposed multiple high-index {012}, {210}, {115}, and {511} facets were prepared by Zou et al., which exhibited an excellent photocatalytic performance, with 2 orders of magnitude larger oxygen production rate than that of the bulk BiVO$_4$.[99] Interestingly, Zhai et al. reported that the BiVO$_4$ polyhedron surrounded by 42 low- and high- index facets showed improved photocatalytic performance for RhB degradation compared to the BiVO$_4$ octahedral crystals without truncation (Figure 9g,h).[100] This enhanced photocatalytic performance was attributed to a higher charge separation efficiency on the coexposed low- and high- index facets, as demonstrated by the facet-dependent photodeposition of Au and MnO$_x$ NPs on the electron- and hole-accumulated facets, respectively.

However, it should be noted that the facet-dependent performance of mBiVO$_4$ is affected by a mix of different catalytic mechanisms, such as charge separation efficiency, light absorption capacity, band structure, and so on. For instance, mBiVO$_4$ plate with {040} facet exposed was hydrothermally synthesized through a seed layer method using TiCl$_3$ as structure directing agent.[101] Various samples, BiVO$_4$ seed layer (SL-BVO), BiVO$_4$ plate film (PF-BVO), and {040} facet BiVO$_4$ film ({040}-BVO), were prepared by controlling the amount of added TiCl$_3$ (Figure 10a). Compared with PF-BVO, {040}-BVO showed a relatively high photocurrent density (Figure 10b) and incident photon to current conversion efficiency (Figure 10c), indicating a faster charge separation efficiency and higher solar light absorption, respectively. In addition, extended X-ray absorption fine structures (EXAFS) analysis showed that two major peaks appearing at 1.60 and 3.07 Å in dark were slightly shifted to 1.63 Å and to 3.10 Å during the water oxidation, suggesting an increase in the distance of Bi−O and Bi−V in {040}-BVO sample, which provided more favorable local bonding geometry for water molecules adsorption (Figure 10d). Time-resolved photoluminescence (TRPL) calculation showed that the {040}-BVO had a longer average decay time of the charge carriers at the emitted 406, 550, and 600 nm compared with SL-BVO and PF-BVO, which suggested a long-lived charge accumulation at the interface between {040} facet and water molecules, thereby greatly improving the photocatalytic performance of water oxidation (Figure 10e).

To sum up, facet-dependent adsorption can provide guidance for improving the selectivity of photocatalytic reactions, and facet-dependent photocatalytic reaction facilitates the design of bifunctional photocatalysts. Selective exposure of certain facets will result in different photocatalytic activities, and in general, semiconductors with high active facet exposure will result in high photocatalytic activity. In order to take advantage of the positive effects of high activity facet on overall photocatalytic activity, the next challenge in the surface facet design of single mBiVO$_4$ is how to increase the proportion of these highly active facets.

4.2. Large Proportion of Surface Facets with High Photocatalytic Activity. On the one hand, the surface of mBiVO$_4$ covered by one facet as much as possible facilitates the investigation of the underling mechanisms of facet-dependent performance. On the other hand, the understanding obtained from the mechanism investigation can give guidance for tailoring the facets to obtain an improved photocatalytic performance. In order to increase the percentage of highly active facets, an ideal strategy is to prepare symmetric polyhedral photocatalysts surrounded by highly active facets, such as Ag$_3$PO$_4$ rhombohedral dodecahedron composed of {110} facets and CoO octahedrons surrounded by polar {111} facets.[102,103] Similarly, bipyramidal BiVO$_4$ microcrystals enclosed with {102} and {012} facets were prepared, which exhibited higher activity and selectivity in the conversion of methane to methanol compared to BiVO$_4$ platelet with exposed {001} facet at the top and bottom (Figure 11a,b).[104] This excellent performance was attributed to the fact that the surface energy of {001} facet (0.349 J m^{-2}) was much lower than that of {102} (0.662 J m^{-2}) and {012} facets (0.660 J m^{-2}), and the extraction efficiency of photoexcited holes from the surface was much higher in bipyramidal than that in platelet sample. In addition, Fang et al. successfully prepared dodecahedron BiVO$_4$:YVO$_4$ solid solution with only two facets exposure, {101} and {100}.[105] SEM images showed that the crystal system of decahedron BiVO$_4$ was changed to dodecahedron Bi$_x$Y$_{1-x}$VO$_4$ after doping with Y (Figure 11c). Due to the different surface energy of (100), (010), and (001) facets, only two facets, {010} and {110}, were exposed in decahedron BiVO$_4$. However, doping with Y greatly improved the symmetry of the crystal, making the (010) and (100) faces identical, resulting in four facets, that were (100), (−100), (010) and (0−10), were exposed in dodecahedron Bi$_x$Y$_{1-x}$VO$_4$ and an increased percentage of reactive surface. Moreover, a surface heterojunction was formed between {100} and {101} facet owing to the slight inconsistency in their band energy, resulting in an efficient spatial charge separation on adjacent exposed facets. With the photocatalytic overall water splitting as a reaction model, a high production of hydrogen and oxygen with a stoichiometric ratio was obtained.

Compared with a symmetrical structure, more research interest and efforts are focused on design 2D mBiVO$_4$ to expose its flat surface to highly active facets. For instance, with the photocatalytic degradation of oxytetracycline (OTC) as a reaction model, the degradation efficiency decreased from 62.33% to 10.39% when the exposure ratio of {001} facet of mBiVO$_4$ decreased from 89.28% in the 10 nm (tBV160) to 84.21% in the 100 nm (hBV160) composite (Figure 11d).[106] This drop in photocatalytic performance was attributed to a decreased exposed proportion of {001} facet, resulting in a relatively poor internal electric field, which in turn reduced the charge separation efficiency. Similarly, different morphology and size samples having various exposure extension of {040} facets were obtained with a hydrothermal method by adjusting the molar ratios of Br to V.[107] The sample with Br:V molar ratio of 3:1 exhibited the optimal photocatalytic performance for RhB degradation, with a degradation efficiency of 98.9% within 30 min, which was attributed to a higher exposure ratio of high-active {040} facets and a larger specific surface area.

DOI: 10.1021/acscatal.9b03411
ACS Catal. 2020, 10, 1024−1059

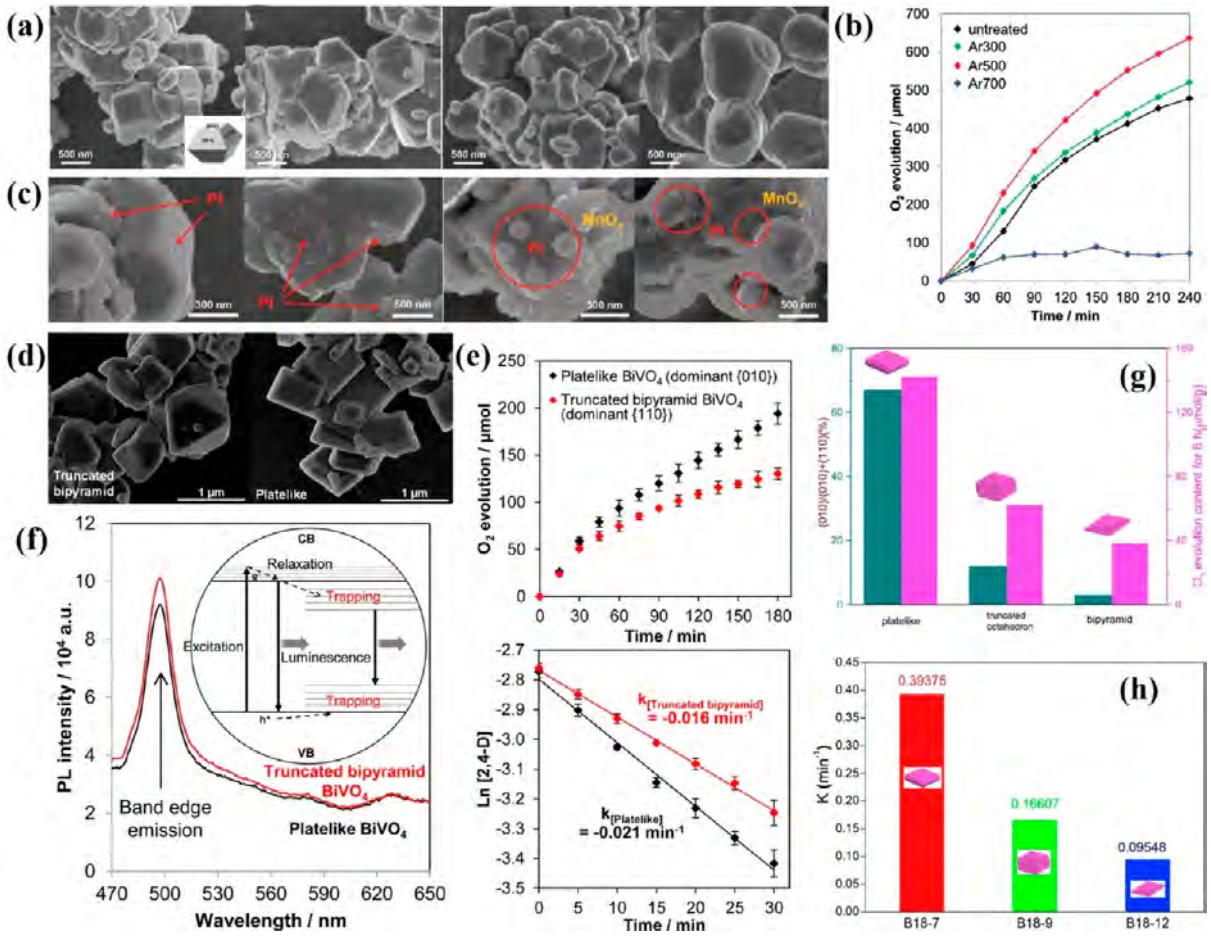

Figure 12. (a) SEM images of the untreated $BiVO_4$ and Ar-treated $BiVO_4$ samples prepared at 300, 500, and 700 °C. (b) photocatalytic O_2 evolution from $BiVO_4$ samples annealed at 300, 500, and 700 °C under Ar atmosphere in comparison to the untreated sample. (c) SEM images of the Pt-loaded untreated $BiVO_4$, Pt-loaded Ar 700 and Pt/MnO_x-loaded untreated $BiVO_4$, Pt/MnOx-loaded Ar 700. Reproduced with permission from ref 116. Copyright 2016 Wiley-VCH Verlag GmbH & Co. KGaA, Weinheim. (d) SEM micrographs of bare truncated bipyramid and platelike $BiVO_4$ (obtained using 1.0 and 0.5 M of nitric acid, respectively). (e) Photocatalytic O_2 evolution from aqueous $AgNO_3$ solution and pseudo-first-order-fitted 2,4-D decay curves of the initial 30 min illumination of truncated bipyramid (red) and platelike $BiVO_4$ (black) under visible light. (f) Steady-state fluorescence spectra of truncated bipyramid and platelike $BiVO_4$. Inset displays the mechanism of photoluminescence. Reproduced with permission from ref 117. Copyright 2016 American Chemical Society. (g) The relationship between photocatalytic activities of O_2 evolution and ratio of {010} facet for *m*$BiVO_4$ samples. (h) The reaction rate of O_2 evolution. Reproduced with permission from ref 118. Copyright 2019 Elsevier.

Moreover, Tan et al. found that a higher exposed area of {010} facet resulted in a greater enhancement in photocurrent in GO/$BiVO_4$, which was attributed to the fact that the Schottky barrier at GO/$BiVO_4${010} interface was smaller than GO/$BiVO_4${110} interface (Figure 11e).[82] Therefore, the optimal photocatalytic performance was obtained by increasing the exposure ratio of {010} to {110} facet.

More recently, ultrathin 2D materials with the thickness less than 5 nm have attracted an increasing attention due to their relatively high specific surface area, vast number of unsaturated coordinated surface atoms, and short transfer distance for charge carriers.[108] Previous studies have demonstrated that the {010} facet of *m*$BiVO_4$ mainly undergoes the reduction; however, the {110} facet prefers an oxidation reaction, and the photocatalytic performance of *m*$BiVO_4$ is mainly dependent on the exposure ratio of the high-active {010} facet.[109] Therefore, it is rational to construct ultrathin *m*$BiVO_4$ with exposed {010} facet to optimize the adsorption of reactant molecule, the separation efficiency of photogenerated charge carriers and the reaction processes. As a typical example, ultrathin 2D *m*$BiVO_4$ nanosheets with the thickness of no more than 3 nm and the diameter greater than 1.2 μm was prepared by a colloidal two-phase method (Figure 11f), which exhibited an excellent photocatalytic performance for water oxidation with the oxygen evolution rate of 107.4 μmol h^{-1}.[110] This enhancement in photocatalytic performance was attributed to the fact that the ultrathin 2D *m*$BiVO_4$ nanosheets with increased specific surface area could increase the number of surface atoms as active sites to accelerate the progress of the reaction. The thickness at the atomic scale shortened the transfer distance of photogenerated electrons from the bulk to the {010} facet of *m*$BiVO_4$ (Figure 11f inset), and the spatial separation of photogenerated charge between the {010} and {110} facet resulted in more available electrons accumulation on the {010} facet (Figure 11g). Also, the dissociation energies of H_2O into H and O atoms were remarkably deduced from 4.562 to 2.455 eV due to the existence of surface oxygen vacancies (V_o) on the {010} facet, and the electronic DOS at CBM and VBM were increased, which promoted the photon conversion and the photogenerated charge separation, leading to an improved

DOI: 10.1021/acscatal.9b03411
ACS Catal. 2020, 10, 1024−1059

the photocatalytic performance. Similarly, Zhu et al. reported that the thin mBiVO$_4$ platelets with exposed {001} facet as their top and bottom surface exhibited higher photocatalytic CH_4 conversion efficiency compared with the thick platelets surrounded by {102} and {012} facets with a thickness about 1 μm, which was due to the different distance for electrons transfer.[104] That was, the distance required for electrons transfer to the surface in thin platelets was relatively short compared to thick platelets, which resulted in more available photoexcited electrons for surface reactions.

As mentioned above, it is widely accepted that the photogenerated holes are preferentially accumulated on the {110} facet while electrons on the {010} facet within mBiVO$_4$ semiconductor, which caused the {110} facet to function as the active oxidation site. However, many previously reported studies have proposed a contradicting conclusion that mBiVO$_4$ exhibited {010} facet-dependent performance in photocatalytic organic degradation and oxygen evolution.[56,68,80] A further theoretical investigation performance by Yang et al. reported that the {010} facet of mBiVO$_4$ was more favorable for the water oxidation reaction than the {110} facet because the former had higher carrier mobility, easier water adsorption and lower energy barrier.[67] These contradictory conclusions may be due to the fact that the influence of facets on the separation and migration of photogenerated charge carriers is only one of the factors of facet-dependent photocatalytic performance, which motivates researchers to project the focus to the exposure ratio of different facets.

4.3. Synergism between Different Surface Facets with Optimal Ratios. As demonstrated above, increasing the proportion of highly active facet on the surface of mBiVO$_4$ can significantly improve its photocatalytic performance. Nevertheless, previous works showed that TiO_2 and CeO_2 photocatalysts with two facets coexisting in an appropriate ratio exhibited improved photocatalytic performance for CO_2 reduction.[111,112] In the case of mBiVO$_4$, the spatial separation of charge carriers on different facets of mBiVO$_4$ results in the accumulation of photogenerated electrons and holes in the {010} and {110} facet of mBiVO$_4$, respectively. Therefore, the coexistence of {010} and {110} facets with rational exposure ratio is expected to be beneficial to the separation of photogenerated electrons and holes. An excellent evidence was that mBiVO$_4$ with an equal fraction of exposed {010} and {110} facets exhibited highest charge separation efficiency and C2-compound yield (mainly ethylene glycol and glycolaldehyde).[75] It was found that the photocatalytic performance increased as the fraction of the {010} facet increased from 25% to 50%, and a further increase would result in a decrease in the yield of C2-compound. More importantly, all mBiVO$_4$ with different fraction of {010} facet exhibited higher photocatalytic performance for HCHO conversion than BiVO$_4$-010 and BiVO$_4$-110 samples with predominantly exposed {010} and {110} facet, respectively, demonstrating that both {010} and {110} facet are required for obtaining a high activity. Likewise, Yuan et al. reported that mBiVO$_4$ with almost a 1:1 ratio of {040}to {110} facet exhibited the highest activity in the amine photooxidation with 94% selectivity.[113] Another example, Tan et al. applied annealing, a postsynthesis method that adjusts the crystal morphological through minimizing the surface free energy,[114,115] to synthesize dual-faceted mBiVO$_4$ under Ar atmosphere at different temperatures ranging from 300 to 700 °C.[116] It was found that the well-defined crystal facet of mBiVO$_4$ was gradually diminished as the temperatures increased (Figure 12a). Despite that mBiVO$_4$ annealed at 700 °C exhibited better crystallinity, greater orbital overlap, and smaller bandgap, the photocatalytic performance for oxygen evolution was lower than other samples owing to the destruction of the active crystal facets (Figure 12b). Photodeposition experiments showed that Pt particles and MnO_x were selectively deposited on the {010} and {110} facet of the well-defined mBiVO$_4$, respectively. While the surface of mBiVO$_4$ annealed at 700 °C was completely covered by spongy-like MnO_x and agglomerated Pt particles, indicating poor charge separation efficiency (Figure 12c). Therefore, the presence of well-developed {010} and {110} facet is essential for efficient charge separation.

Because the transfer efficiency of photogenerated electrons and holes to the corresponding electron acceptors and donors is an important indicator for evaluating photocatalytic activity, the accumulation of either photogenerated electrons or holes will lead to an increase in the probability of charge recombination and a decrease in quantum yield, thereby resulting in poor photocatalytic performance. Given the importance of efficient charge transfer in photocatalysis, the investigation on the relationship between the relative exposure extent of redox functional facets and the charge transfer kinetics of the photocatalyst is critical for designing highly efficient photocatalysts. For example, Tan et al. prepared a thickness-controlled decahedron mBiVO$_4$ samples by varying the concentrations of nitric acid during the synthesis.[117] A relatively low concentration of nitric acid resulted in a markedly thinner mBiVO$_4$ with a higher ratio of {010} to {110} facet, denoted as plate-like mBiVO$_4$. Whereas a thick mBiVO$_4$ with a relatively small ratio of {010} to {110} facet, denoted as truncated bipyramid mBiVO$_4$ (Figure 12d). With photocatalytic water oxidation and 2,4-dichlorophenoxyacetic acid degradation as a model reaction, it demonstrated that the photocatalytic performance of plate-like mBiVO$_4$ was higher than that of truncated bipyramid mBiVO$_4$ (Figure 12e). This phenomenon was mainly ascribed to the fact that plate-like mBiVO$_4$ with relatively large {010} facet exposed endowed it with more available photogenerated electrons on the surface, as demonstrated by photoluminescence (PL) quenching effect (Figure 12f). Conversely, the greater thickness resulted in longer transfer distance for photogenerated electrons and holes from bulk to the surface in the truncated bipyramid mBiVO$_4$, which increased the possibility that photogenerated electrons would encounter and be captured by crystal defects, resulting in limited electrons available on the {010} facet. In addition, compared to plate-like mBiVO$_4$, truncated bipyramid mBiVO$_4$ exhibited a better electron trapping capacity due to the shorter fluorescence lifetime, the trapped electrons would recombine with the holes, leading to fewer holes available for oxidation reactions. Overall, a relatively large exposure ratio of {010} to {110} facet endowed plate-like mBiVO$_4$ a superior photooxidation activities than truncated bipyramid mBiVO$_4$. Similar conclusions were also revealed by Shan et al., that is, a positive relationship between the photocatalytic activity for oxygen evolution and the exposure ratio of {010} and {110} facets in mBiVO$_4$ (Figure 12g,h).[118] This difference in oxygen evolution rate was attributed to the fact that {110} facet with high energy level had a highly tight-binding effect for photogenerated carrier, which may increase the possibility of carrier recombination. Furthermore, mBiVO$_4$ with different proportions of {101} to {010} facet was precisely synthesized and the morphology of mBiVO$_4$ varied from decahedron crystals to

DOI: 10.1021/acscatal.9b03411
ACS Catal. 2020, 10, 1024−1059

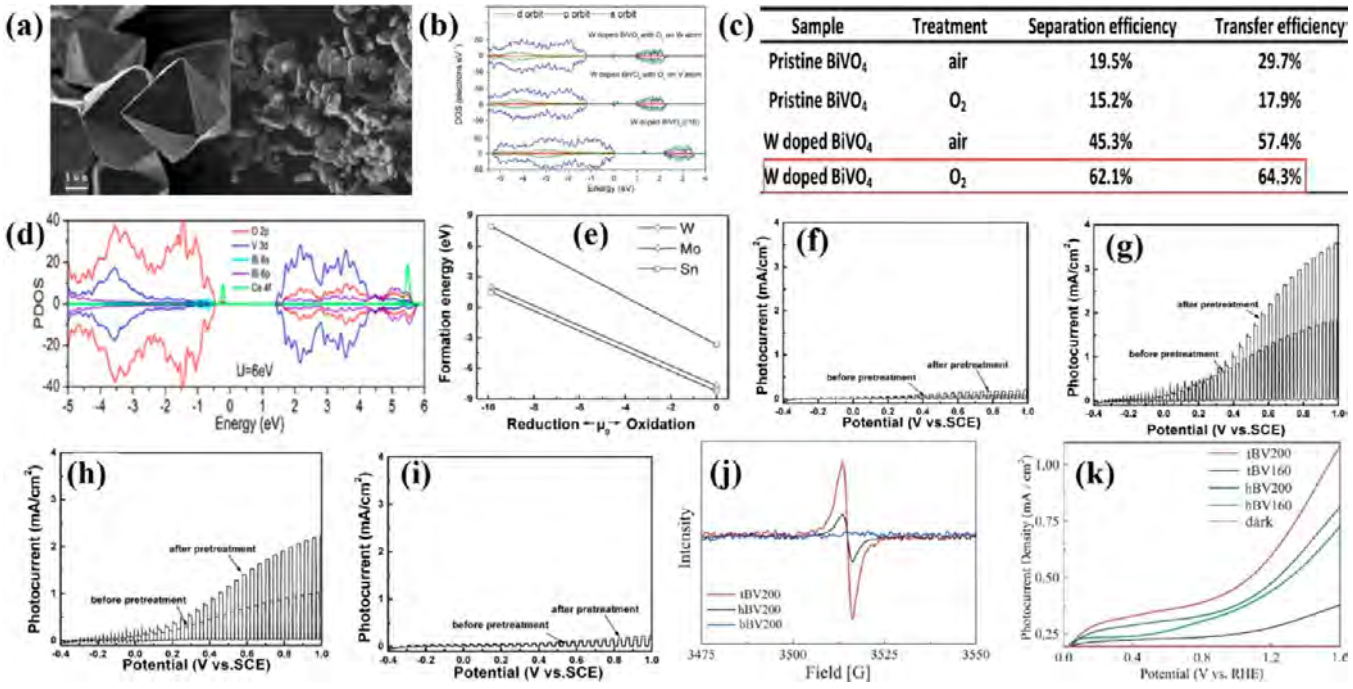

Figure 13. (a) SEM image of pure $BiVO_4$ and N-doped $BiVO_4$ nanoplates. Reproduced with permission from ref 134. Copyright 2014 Elsevier. (b) DOS of W-doped $BiVO_4$, W-doped $BiVO_4$ with oxygen vacancy (O_v) on V atom, and W-doped $BiVO_4$ with oxygen vacancy (O_v) on W atom. (c) Calculated charge separation efficiency and water oxidation charge transfer efficiency of pristine and W-doped $BiVO_4$ annealed in air and O_2 gas respectively at 1.23 V vs RHE. Reproduced with permission from ref 135. Copyright 2018 American Chemical Society. (d) PDOS plots of Ce-$BiVO_4$ calculated using U(Ce) = 6 eV. Reproduced with permission from ref 140. Copyright 2016 American Chemical Society. (e) Formation energy of doping ions in the $BiVO_4$ crystal lattice. The photocurrent from the front side before and after the pretreatment of (f) pure, (g) Mo^{6+}, (h) W^{6+}, (i) Sn^{4+}-doped $BiVO_4$. Reproduced with permission from ref 142. Copyright 2013 Elsevier. (j) OVs EPR signal of tBV200, hBV200 and bBV200. (k) LSV curves (under the irradiation of one 500W Xe lamp) of tBV200, tBV160, hBV200, and hBV160, respectively. Reproduced with permission from ref 106. Copyright 2018 Elsevier.

short-rod like particles with the increasing pH.[81] The decahedron $BiVO_4$ sample exhibited the best photocatalytic oxygen evolution performance, with 50 times oxygen evolution rate oxygen evolution rate that of tetragonal $BiVO_4$ particles, which was ascribed to the optimized reduction and oxidation reaction rates by controlling the exposure ratio of {010} to {011} facets.

It is worth mentioning that another contribution of the coexposure of adjacent facets is the formation of homojunctions in the same *m*$BiVO_4$ semiconductor, which results in the photogenerated holes and electrons diffusing from the inside of *m*$BiVO_4$ toward the opposite direction, thereby being captured by the topmost exposed atoms. Additionally, the photoexcited electrons and holes can be separated at two adjacent facets, which greatly lower the possibility of bulk recombination of photogenerated electrons and holes. In this regard, Wang et al. applied an additive-free low-temperature aqueous method to synthesize *m*$BiVO_4$ with {010} and {110} coexposed which underwent the nucleation and Ostwald growth process.[95] The growth rate of the high-energy {010} facet determined by the pH values, a relatively low H^+ resulted in a lower concentration of the free BiO^+ ions in the solution, which slowed the nucleation rate of *m*$BiVO_4$ crystals and promoted the formation of the highly active crystal facets. Moreover, the surface free energy through Ostwald ripening of the {010} facet of *m*$BiVO_4$ was reduced after adsorption with appropriate H^+, which also facilitated the formation of {010} facet. In contrast, a lower or higher H^+ concentration would destroy the {010} crystal facets. DFT calculation showed that a surface heterojunction was generated between {010} and {110} facet due to energy level mismatch, resulting in the transfer of photogenerated electrons and holes to the {010} and {110} facet, respectively. Therefore, *m*$BiVO_4$ with the optimized exposure ratio of {010} to {110} facet exhibited the optimal photocatalytic performance for RhB and MB degradation among all the samples. In a similar case, Yu et al. synthesized *m*$BiVO_4$ with {010} facet orientation growth through two methods, aqueous process (AP-BVO), and one-step hydrothermal method (HT-BVO).[119] The XRD pattern showed that the HT-BVO had relatively high crystallinity and peak intensity corresponding to {040} facet compared with AP-BVO, indicating the preferential crystal growth along the {010} facet in HT-BVO samples, resulting in the photocatalytic performance of HT-BVO of 1.75 times that of AP-BVO in the coexistence system of Cr(VI) and phenol. This enhancement was related to the generation of surface heterojunction in HT-BVO, which improved the charge separation efficiency between adjacent {010} and {110} facet, leaving strong reduction electrons to participate in Cr(VI) reduction on {010} facets and the strong oxidation holes to oxidize phenol on {110} facets.

In summary, increasing the exposure ratio of highly active facet is a feasible measure to design highly efficient *m*$BiVO_4$ catalysts, which requires the fundamental investigation on facet-dependent photocatalytic performance and related mechanism. Typically, designing *m*$BiVO_4$ semiconductor with most of the highly reactive surface covered can be done from two perspectives. One is to synthesize symmetrical polyhedral *m*$BiVO_4$ crystals surrounded by highly active crystal facets, whereas there are few reports in this direction currently.

DOI: 10.1021/acscatal.9b03411
ACS Catal. 2020, 10, 1024−1059

The other and currently the most widely studied is the synthesis of 2D ultrathin *m*$BiVO_4$ nanosheets whose flat surfaces are designed as highly active crystal facets. Moreover, when *m*$BiVO_4$ is surrounded by multiple crystal facets, the exposure ratio of different surface facets is another significant parameter that needs to be considered. Not only the high-active facets but also the electronic band structures of surface facets should be rationally designed.

5. FACET ENGINEERING FOR MODIFICATION OF CHARGE CARRIER BEHAVIOR IN *M*$BIVO_4$-BASED PHOTOCATALYTIC SYSTEM

Although the facet engineering with respect to surface design of single *m*$BiVO_4$ do achieve improved photocatalytic performance to a certain extent, the obtained photocatalytic performance of *m*$BiVO_4$ is still far below its theoretical maximum, which is mainly limited by poor electron transport and slow hole transfer. Therefore, taking into account the unique crystal structure of *m*$BiVO_4$, the modification of *m*$BiVO_4$ based on facet engineering is desirable to solve the above-mentioned two limitations.

5.1. Heteroatom Doping for Improved Electron Transport. The poor electron transport performance may be attributed to the unconnected VO_4 tetrahedral unit in the crystal structure of *m*$BiVO_4$, which indicated that the photoexcited electrons in the V 3d CB have to hop between the VO_4 tetrahedra.[33] As demonstrated by Rettie and co-worker, the charge transfer in *m*$BiVO_4$ from 250 to 400 K was governed by a small polaron hopping mechanism associated with low electron mobility.[120] In theory, low wave function overlap between V 3d and Bi 6p orbitals in the CB of *m*$BiVO_4$ results in electron localization.[58] Given that, efforts with respect to electron transport have demonstrated that doping heteroatom into the lattice or lattice gap of semiconductor can change the geometry and electronic structure of the intrinsic matrix, as well as the carrier density, which is a highly feasible strategy to enhance the photocatalytic performance.[121]

At present, the most widely studied on this subject are nonmetal doping such as N,[122] C,[123−126] B,[127−129] S,[130,131] F,[132,133] and P,[44] which can not only introduce an impurity level in the unaltered band gap by replacing the O site in the crystal lattice but also narrow the forbidden bandwidth by the hybridization of the p-orbital in nonmetallic elements with the O 2p orbital in *m*$BiVO_4$. For instance, the polyhedrons $BiVO_4$ with smooth surface and long sharp edges was transferred into plate-like structure with relative short length after doping with nitrogen (Figure 13a), and this decrease in the particle size remarkably shortened the charge transfer distance.[134] Most importantly, plate-like *m*$BiVO_4$ with high {040} facet exposure ratio provided more multiatomic BiV_4 centers for multielectron transfer. The surface V_o originated from the incorporation of nitrogen in N-doped *m*$BiVO_4$ can trap the holes, which remarkably promoted the separation of photogenerated electrons and holes. Moreover, the band gap of pure *m*$BiVO_4$ was reduced from 2.2 to 2.0 eV after doping with nitrogen, which greatly improved the light absorption ability. Therefore, the photocatalytic performance of N-doped *m*$BiVO_4$ for RhB degradation was much higher than that of pure *m*$BiVO_4$.

In terms of substituted sites, V, Bi, and O atoms are all possible substitution sites in *m*$BiVO_4$. Among them, the substitution of doping agent for V-sites is the most common case. For instance, Zhao and his co-workers introduced W^{6+} to substitute V-sites, accompanying with the introduction of V_o on V-sites of {010} facet in *m*$BiVO_4$.[135] As W^{6+} had relatively higher valence states compared with V^{5+}, the phase transition from the monoclinic to tetragonal was greatly suppressed, resulting in less distortion in the [VO_4] tetrahedron chains. Moreover, DFT calculations demonstrated that there were two different states in the bandgap with the V_o on V-sites, while only one different state presented for V_o on W-sites or without V_o, indicating more active sites formed in W-doped {010}-*m*$BiVO_4$ with V_o on V-sites, thereby increasing the number of surface reaction sites (Figure 13b). The generated V_o on the surface can serve as the recombination center for undesired photogenerated electrons and holes to promote the charge separation and also facilitate the charge transfer (Figure 13c), leaving the highly reductive electrons and oxidized holes to participate in the redox reaction on the surface of catalysts.[136−139] Therefore, W-doped {010}-*m*$BiVO_4$ exhibited an improved photocatalytic performance for water splitting compared with that of nondoping samples.

However, the substitution of V-sites still easily causes the distortion of [VO_4] tetrahedral chains, which have negative effects on photocatalytic water splitting. In view of that, the Bi^{3+}-sites substitution is another effective method to protect the [VO_4] tetrahedral chains from distortion. For instance, trivalent cation Ce^{3+} with the similar ionic radius to that of Bi^{3+} was used to substitute Bi^{3+}-sites in *m*$BiVO_4$ by Jiang et al.[140] GGA+U calculation of Ce-$BiVO_4$ exhibited that the values of U(Ce) was 6 eV, indicating that the up-spin f^1 level of Ce^{3+} slightly lay above the VBM of *m*$BiVO_4$ (Figure 13d). Therefore, Ce^{3+} ions as holes traps not only maintained complete [VO_4] tetrahedron but also prolonged the lifetime of photogenerated holes, eventually resulting in an enhanced photocatalytic performance for water oxidation. Also, Wang et al. applied In^{3+} ions to substituted Bi^{3+}-sites in *m*$BiVO_4$ to evaluate the influences of In^{3+} ions on the morphology and photocatalytic performance.[141] XRD pattern showed that the peak intensity corresponding to {121} facet gradually decreased with the increase of In^{3+} content because of the distortion of the {121} facet. Further Raman analysis confirmed that the V−O stretching mode exhibited a slight shift to higher wavenumber, suggesting that the bond length of the V−O was decreased resulting from the {121} facet distortion. Hence, a short distance for photogenerated electrons and holes to active sites was favorable for the improvement of photocatalytic performance.

As above, doping *m*$BiVO_4$ with higher valence metal ions can remarkably increase the carrier density. However, the difference in photocatalytic performance between the V-sites and Bi^{3+}-sites is still ambiguous. With that in mind, Luo et al. used high-valence ions (Mo^{6+}, W^{6+}) and relatively low-valence ion (Sn^{4+}) to respectively substitute V^{5+}-sites and Bi^{3+}-sites to investigate the doping effect at these two sites.[142] The formation energy of Mo/W-$BiVO_4$ samples was similar, which was much lower than that of Sn-$BiVO_4$ owing to a larger radius mismatch between Sn^{4+} and Bi^{3+} than that of Mo^{6+}/W^{6+} and V^{5+} as well as a different outer shell electron distribution (Figure 13e). In addition, the photocurrent potential curves exhibited an obvious increase for Mo/W-$BiVO_4$ while just a slight enhancement for Sn-$BiVO_4$, which was attributed to the serious surface segregation of SnO_2 (Figure 13f−i). Therefore, only doping *m*$BiVO_4$ with suitable high-valence metal ions can significantly improve the photocatalytic performance.

DOI: 10.1021/acscatal.9b03411
ACS Catal. 2020, 10, 1024−1059

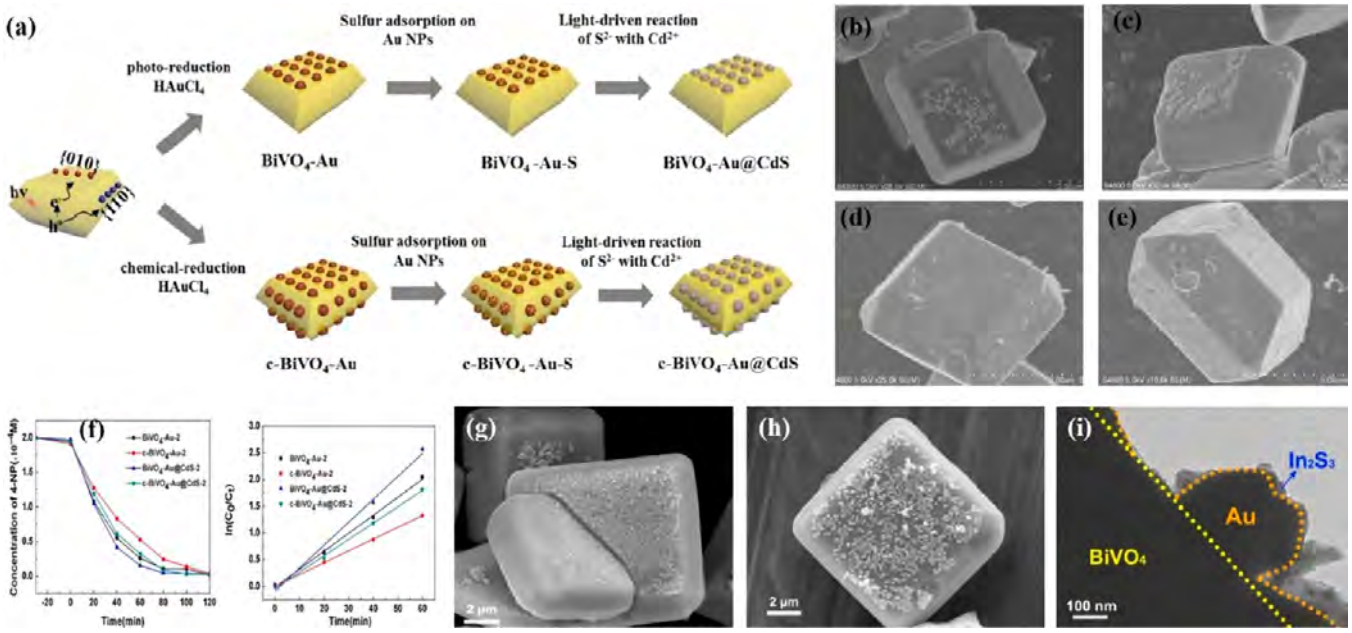

Figure 14. (a) Schematic illustration for preparation of $BiVO_4$−Au@CdS. SEM images of (b) $BiVO_4$−Au, (c) $BiVO_4$−Au@CdS, (d) c-$BiVO_4$−Au, (e) c-$BiVO_4$−Au@CdS. Reproduced with permission from ref 158. Copyright 2017 Elsevier. (f) Concentration of 4-NP versus time plots and degradation kinetics of 4-NP during the photocatalytic process on different photocatalysts under visible light irradiation ($\lambda \geq 420$ nm). SEM image of (g) Au-$BiVO_4$, (h) In_2S_3−Au-$BiVO_4$ and (i) HR-TEM image of In_2S_3−Au-$BiVO_4$. Reproduced with permission from ref 159. Copyright 2018 Wiley-VCH Verlag GmbH & Co. KGaA, Weinheim.

Certainly, it cannot be ignored that there are O-sites consisting of $[VO_4]$ and $[BiO_8]$ in *m*$BiVO_4$. Given that the *m*$BiVO_4$ matrix has highly or even preferentially exposed {010} facet and the introduction of V_o can increase the electron density, the composite materials constructed by element doping and V_o decorated on the highly active {010} facet exhibited a more excellent photocatalytic performance than those composites based on randomly oriented *m*$BiVO_4$. A typical example, as the surface oxygen atom of {001} faceted-$BiVO_4$ had a strong hydrogen bonding with the hydrogen atoms of adsorbed water molecules, taking this advantage, Ullah et al. prepared {001} faceted-$BiVO_4$ film with oxygen defective and Se-doped to investigate the photocatalytic performance for water splitting.[143] The electronic band structure and the partial density of states plot of *m*$BiVO_4$-{001}@H_2O demonstrated that the band gap of $BiVO_4$-{001} was reduced from 2.24 to 1.74 eV, suggesting that water molecules were preferentially adsorbed on the surface of {001} facets, thereby promoting the efficiency of photocatalytic water splitting.

Similar to heteroatom doping, the self-doping is considered as an effective strategy to finely tune the energy band structure and electronic structures of the semiconductors, as it can eliminate the recombination effect from doped impurities defects energy level and simultaneously enhance the redox reactivity of semiconductors. Simultaneously, the self-doped strategy can introduce oxygen vacancy defects on the surface/bulk of oxygen-containing semiconductors. For instance, the V^{4+} self-doped *m*$BiVO_4$ samples with a specific growth and self-assemble direction of [010] were successfully prepared by a one-step hydrothermal route,[144] which exhibited a high charge separation efficiency by accumulating electrons on {010} facet. However, an improved photocatalytic activity with a decreased adsorption ability was obtained after further low-temperature treatment, which was attributed to elevated crystallinity and decreased V_o. As demonstrated by the Gaussian−Lorentzian fitting results, the doping amount of the V^{4+} species was decreased from 31 at% to less than 10 at%. Therefore, V_o is a double-edged sword, only appropriate V_o can serve as an electron capture center to effectively promote charge separation, resulting in improved photocatalytic performance. An excellent example is that the *m*$BiVO_4$ nanosheet with reduced thickness, enlarged dominant {001} facet, and enhanced V_o was prepared through hydrothermal method.[106] By increasing the synthesis temperature of *m*$BiVO_4$ with exposed {001} facet, the V_o peaks and the exposure ratio of {001} facet of *m*$BiVO_4$ (160 °C) were obviously increased compared with those of their counterparts (160 °C) (Figure 13j), which increased the photocurrent density by approximately 1.33 times compared to its counterpart treated by 160 °C (Figure 13k). The use of V_o as photoinduced electron trapping sites can inhibit the recombination of electrons and holes and provide more active sites for photocatalytic reactions, thereby resulting in an improved photocatalytic performance toward OTC degradation.

5.2. Heterojunction Construction for Improved Interfacial Charge Separation and Transfer. Apart from poor electron transport, another limiting factor for the photocatalytic performance of *m*$BiVO_4$ is slow hole transfer (slow water oxidation kinetics), as demonstrated by about 3-fold enhancement of the photocurrent density of *m*$BiVO_4$ in the presence of H_2O_2.[34,145,146] A large number of studies have shown that the modification of *m*$BiVO_4$ with an oxidation cocatalyst such as IrO_2, RuO_2, and Co_3O_4 can promote the hole transfer.[147−149] However, follow-up studies reported by Zhong et al. proposed that the primary bottleneck limiting the photocatalytic performance of *m*$BiVO_4$ was bulk charge carrier recombination.[145] Therefore, further research with respect to developing highly efficient *m*$BiVO_4$ catalysts should focus on how to promote charge separation and transfer. In view of the

DOI: 10.1021/acscatal.9b03411
ACS Catal. 2020, 10, 1024−1059

synergy between the different components can enlarge the light absorption range, decrease the charge recombination possibility, or improve the adsorption and activation of the reactants, coupling mBiVO$_4$ with other components to form hybrid structures is an effective approach to promoting the charge transfer and separation.[150−154] It is worth noting that in the hybrid structure, in addition to the properties of the coupled materials, the facet of mBiVO$_4$ used to form the interfaces in the heterojunction also needs to be rationally designed as the interface properties directly determine the charge separation and transfer.[155] Given that, the main mission for facet-engineered modification of mBiVO$_4$ is to select suitable facets to form favorable interfaces with the coupling materials, with the aim to promote the charge separation and transfer across the interface.

In general, interface charge transfer efficiency is affected by a number of factors, the first of which is the ability to accept photogenerated electrons or holes associated with mBiVO$_4$ facets. This correlation is resulted from the spatial charge separation between adjacent facets or the internal electronic field along a particular crystal orientation. Moreover, the cocatalysts not only further promote the spatial charge separation between adjacent facets but also prevent the back reactions, and the interface between cocatalysts and mBiVO$_4$ provides a channel for charge transfer from mBiVO$_4$ to cocatalysts. Therefore, the selective deposition of reduction and/or oxidation cocatalysts on the electron- and/or hole-accumulated facets is expected to improve photocatalytic performance. Of the cocatalysts, plasmonic NPs are the most widely used reduction cocatalysts, which can achieve efficient charge transfer and separation because of their ability to confine light in the vicinity of their surface and strong surface plasmon resonance (SPR).[156,157] For instance, Cao et al. reported that the photocatalytic performance of mBiVO$_4$ was greatly improved after in situ growth of Au NPs on the surface of mBiVO$_4$, which was attributed to the enhanced charge separation efficiency due to electron sinks and SPR-effect of Au NPs.[41] Interestingly, recent work showed that cocatalysts with core−shell structure can further improve the charge separation efficiency. For example, Ye et al.[158] prepared BiVO$_4$−Au@CdS ternary composite with Au@CdS selectively deposited on the {010} facet through a two-step photoreduction method (Figure 14a,c). With the photocatalytic degradation of RhB as a reaction model, the optimal BiVO$_4$−Au@CdS exhibited 6.11, 3.03, and 2.95 times higher photocatalytic performance to those of mBiVO$_4$, BiVO$_4$−Au, and BiVO$_4$−CdS, which was attributed to the fact that more available Au NPs deposited on the {010} facets of mBiVO$_4$ (Figure 14b) were used to transfer the photogenerated electrons from mBiVO$_4$ to CdS, leading to an efficient charge separation. In contrast, BiVO4-Au@CdS with the randomly deposited Au (Figure 14d) and Au@CdS NPs (Figure 14e) on both {010} and {110} facet prepared by the chemical reduction method exhibited a relatively poor photocatalytic performance for 4-nonylphenol degradation compared with the selectively prepared BiVO4-Au@CdS, demonstrating the important role of facet-induced carrier separation in achieving excellent photocatalytic activity (Figure 14f). Likewise, as reported by Wu et al.,[159] Au^{3+} ions were deposited on the electron-rich BiVO$_4${010} facets through a photoreduction process (Figure 14g), followed by the deposition of In$_2$S$_3$ on Au NPs to form In$_2$S$_3$−Au-BiVO$_4$ (Figure 14h,i). In this ternary system, Au NPs severed as the recombination center of photogenerated electrons from the CB of {010}-BiVO$_4$ and the holes from the VB of In$_2$S$_3$, which not only greatly facilitated the charge separation of individuals but also remained the strongly reductive electrons in the CB of In$_2$S$_3$ and strongly oxidized holes in the VB of {110} facet mBiVO$_4$, leading to the optimal photocatalytic performance for RhB and phenol degradation.

For practical applications, Ag NPs is another alternative to Au plasmonic metal that can improve the photocatalytic performance of mBiVO$_4$. Example such as Ag NPs were selectively deposited on the surface of mBiVO$_4$ by photoreduction with AgNO$_3$ as the precursor,[160] accompanied by the formation of Schottky barrier at the interface of Ag NPs and BiVO$_4${010} facet. As a result, the photogenerated electrons in the CB of BiVO$_4${010} facet would be naturally transferred to the Ag NPs because the work function of metal was much higher than that of semiconductors, leading to an efficient charge separation in the photocatalytic process. Hence, the photocatalytic disinfection performance of mBiVO$_4$ was greatly enhanced after loading with Ag NPs. Furthermore, Ag$_2$O−Ag/BiVO$_4$ photocatalyst with Ag$_2$O−Ag as an electron cocatalyst selectively deposited on the {010} facet of mBiVO$_4$ was prepared by photodepositing metallic Ag and then partially oxidizing Ag to Ag$_2$O under low-temperature calcination, which showed a comparable photocatalytic performance with Pt/BiVO$_4$ but was significantly higher than that of Ag/BiVO$_4$ or mBiVO$_4$.[161] In Ag$_2$O−Ag/BiVO$_4$ hybrid structure, Ag can extract the photogenerated electrons of mBiVO$_4$ and then acted as an electron transporter to transfer electrons to Ag$_2$O, which can provide an active site for surface reaction.

Moreover, taking advantage of the anisotropic facets of mBiVO$_4$, the simultaneous deposition of reduction and reduction cocatalysts on the electron- and/or hole-accumulated facets is expected to further promote the separation of photogenerated electron−hole pairs. For example, metal Pt NPs and Co$_3$O$_4$ species were selectively deposited on the {010} and {110} facets of mBiVO$_4$ by the photodeposition method, denoted as Pt(P.D.)/BiVO$_4$ and Co$_3$O$_4$(P.D.)/BiVO$_4$, respectively.[85] For comparison, Pt(imp)/BiVO$_4$ and Co$_3$O$_4$(imp)/BiVO$_4$ photocatalysts were prepared by the impregnation of Pt NPs or Co$_3$O$_4$ species on the surface of mBiVO$_4$. With the photocatalytic oxygen evolution as a reaction model, Pt(P.D.)/BiVO$_4$ or Co$_3$O$_4$(P.D.)/BiVO$_4$ photocatalysts exhibited the optimal photocatalytic performance in all catalysts, especially far exceeding the composites where the cocatalysts were randomly distributed throughout the surface of mBiVO$_4$ by impregnation method. This improved photocatalytic performance was attributed to the fact that the photogenerated electrons and holes can be trapped by cocatalysts first and then used for the subsequent redox reaction. Further investigation on the deposition of dual cocatalysts also obtained the similar results, that is, Pt/MnO$_x$ and Pt/Co$_3$O$_4$, were selectively deposited on {010} and {110} facets of mBiVO$_4$ by respective photooxidation of Mn^{2+} and photooxidation of Co^{2+}, followed by the photoreduction of $PtCl_6^{2-}$. For comparison, Pt/MnO$_x$/BiVO$_4$ and Pt/Co$_3$O$_4$/BiVO$_4$ photocatalysts were also synthesized through impregnation methods. As expected, Pt/MnO$_x$/BiVO$_4$ and Pt/Co$_3$O$_4$/BiVO$_4$ with dual-cocatalysts selective deposition showed the highest photocatalytic performance for organic degradation and oxygen evolution among all the catalysts. More importantly, it was also confirmed that the photocatalytic performance was greatly enhanced only via depositing the

DOI: 10.1021/acscatal.9b03411
ACS Catal. 2020, 10, 1024−1059

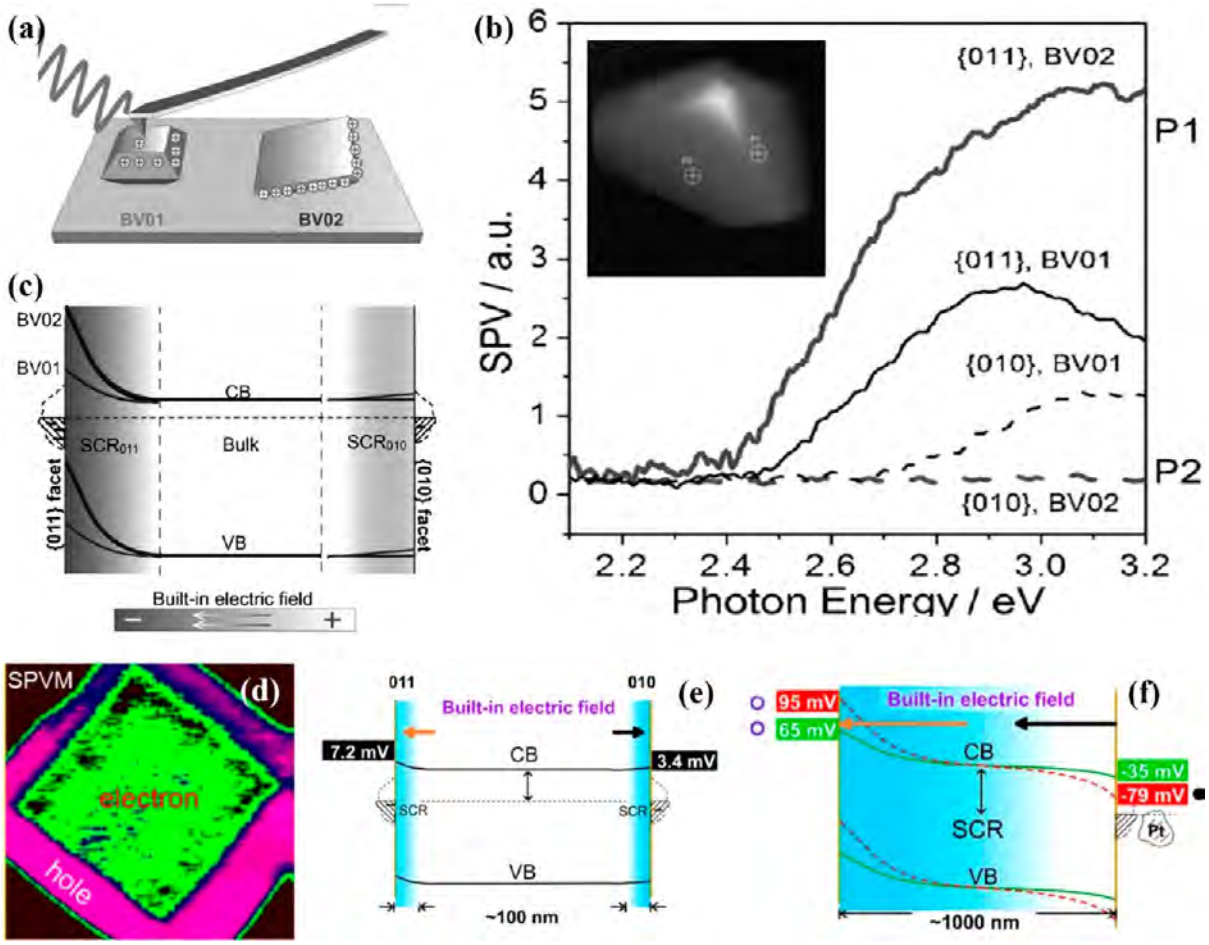

Figure 15. (a) Schematic of the anisotropic charge distributions on a single $BiVO_4$ photocatalyst with different morphologies. (b) Spatially resolved SPV spectra obtained at different locations on BV02 (inset of topology image of BV02 and schematic of the anisotropic charge distributions on a single $BiVO_4$ photocatalyst with different morphologies). (c) Schematic of the built-in electric field with relative strength in the SCR of different facets. Reproduced with permission from ref 162. Copyright 2015 Wiley-VCH Verlag GmbH & Co. KGaA, Weinheim. (d) Spatial distribution of the SPV signals. Pink and green colors correspond to holes and electrons separated toward the external surface, respectively. Schematic band diagrams across the border between the {011} and {010} facets of (e) a bare single $BiVO_4$ photocatalyst particle and of (f) a single $BiVO_4$ photocatalyst particle with MnO_x cocatalyst selectively deposited at {011} facets (green line) and with MnO_x and Pt nanoparticles selectively deposited at {011} and {010} facets, respectively (dashed pink line). Reproduced with permission from ref 163. 2017 American Chemical Society.

reduction and oxidation cocatalysts on the designated facets of the semiconductor.

Although charge separation on different facets of semiconductors can be inferred according to selective photodeposition of metals and metal oxides as well as DFT calculations, there is still no direct evidence to demonstrate anisotropic charge transfer and separation on the surface of semiconductors. In this regard, Zhu et al. applied spatially resolved surface photovoltage spectroscopy (SRSPS) to investigate the surface charge dynamics of single *m*$BiVO_4$, and the results showed that the surface photovoltage (SPV) signals of the {011} facet was much stronger than that of the {010} facet, suggesting the difference in the surface band bending in the space charge region between the {011} and {010} facet (Figure 15a,b).[162] As a result, the built-in electric fields caused by the band bending between these facets was different (Figure 15c), thereby leading to the spatial transfer of photogenerated electrons and holes to a different facet of *m*$BiVO_4$. By increasing the exposure ratio of the {010} to the {011} facet, the {011} facet exhibited 70 times stronger SPS signal compared with that of the {010} facet. Further studies on *m*$BiVO_4$ with selective deposition of MnO_x and Pt NPs on {011} and {010} facets confirmed that cocatalysts can greatly increase the upward band bending and increase the downward band bending, providing an additional driving force as the same direction of the built-in fields for charge transfer to active surface sites beyond their diffusion lengths (Figure 15d,e).[163] More importantly, an additional strong driving force of about 174 mV was obtained after further depositing Pt on the {010} facet, which was much higher than the 3.8 mV of the single *m*$BiVO_4$ (Figure 15f), suggesting that the selective deposition of dual cocatalysts can obtain a significantly increased driving force for charge separation and transfer. The above results can theoretically explain experimental phenomena.[27,41,65,85,93,104]

Another critical factor that affects the charge transfer efficiency across the interface is the electronic band structure since coupling the two components to generate the interface is accompanied by energy band alignment. For instance, $BiVO_4$-TiO_2 heterojunctions were prepared by selectively growing TiO_2 on the {110} and {010} facet of *m*$BiVO_4$, denoted as $BiVO_4$-010-TiO_2 and $BiVO_4$-110-TiO_2, respectively.[92] According to the calculation results reported by Hu and his co-worker, the CBM and VBM of $BiVO_4$ {010} facet was lower than that of $BiVO_4${110} facet.[164] Therefore, the interfacial CB energy

DOI: 10.1021/acscatal.9b03411
ACS Catal. 2020, 10, 1024−1059

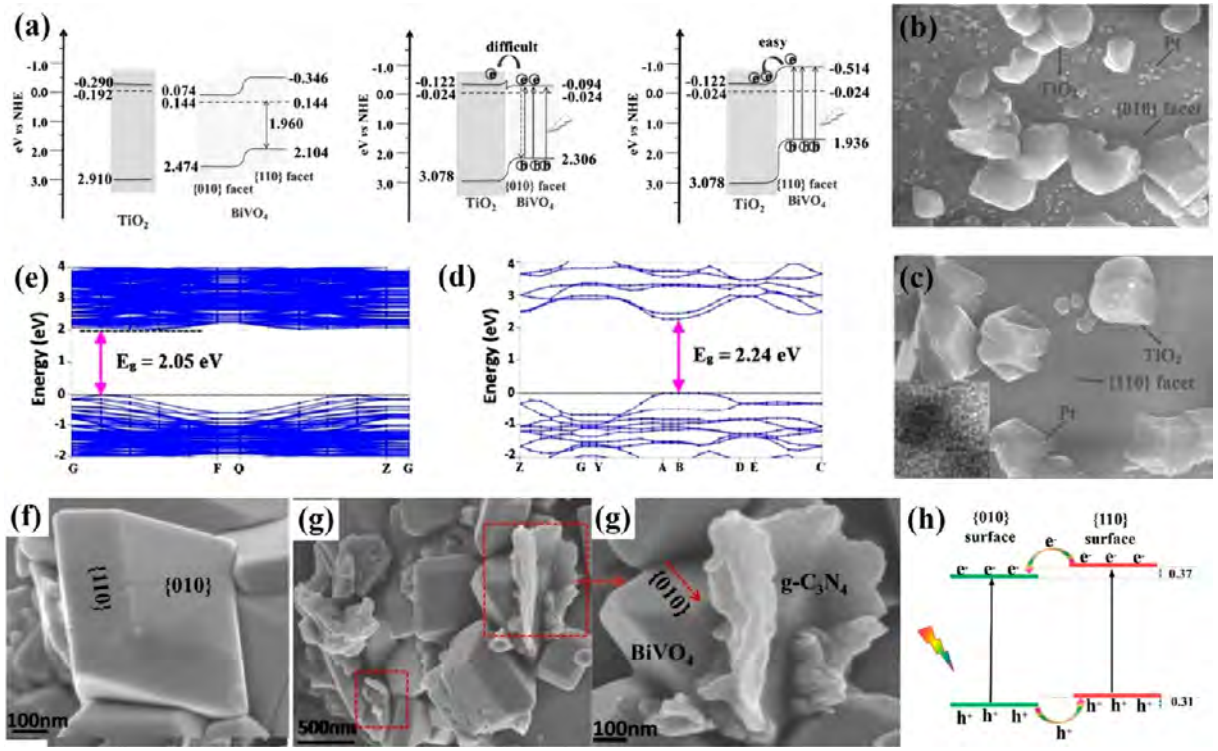

Figure 16. (a) Relative energy band levels of TiO_2, $BiVO_4${010}facet, $BiVO_4${110}facet, and two kinds of $BiVO_4$−TiO_2 heterojunctions by different contact facets. Photoreduction deposition of Pt on (b) $BiVO_4$-110-TiO_2 heterojunction and (c) $BiVO_4$-010-TiO_2 heterojunction under visible light irradiation; the inset image in panel a is the lattice spacing of Pt on TiO_2 surface by HRTEM. Reproduced with permission from ref 92. 2015 Wiley-VCH Verlag GmbH & Co. KGaA, Weinheim. Calculated band structure of (d) *m*$BiVO_4$(010) and (e) MoS_2/m-$BiVO_4$(010). Reproduced with permission from ref 165. Copyright 2017 Royal Society of Chemistry and the Centre National de la Recherche Scientifique. SEM images of (f) $BiVO_4$ and (g) g-C_3N_4/{010} $BiVO_4$. (h) the surface heterojunction formed by {010} and {110} facets of $BiVO_4$. Reproduced with permission from ref 166. Copyright 2018 Elsevier.

barrier at $BiVO_4${010}-TiO_2 interface was much higher than that of $BiVO_4${110}-TiO_2 interface, which greatly hindered the electron transfer from $BiVO_4${110} to TiO_2 (Figure 16a). As a result, the photocatalytic performance for RhB and 4-nonylphenol degradation in $BiVO_4$-110-TiO_2 was 4.09 and 1.33 times higher than that in *m*$BiVO_4$ and $BiVO_4$-010-TiO_2. More surprisingly, metallic Pt was preferentially deposited on the TiO_2 surface instead of the {110} facet of *m*$BiVO_4$ for $BiVO_4$-110-TiO_2 (Figure 16b), while in contrast for $BiVO_4$-010-TiO_2, Pt particles tended to deposit on the {010} facet rather than TiO_2 surface (Figure 16c), which further proved that a lower-energy barrier height facilitated the interfacial charge transfer. Furthermore, a larger contact surfaces on the interface provide more channels for the separation and transfer of photogenerated charge carriers. In order to achieve optimal contact, 2D material with excellent carrier mobility, special surface area, good stability, and controllable interfaces might be an ideal candidate. For example, 2D MoS_2 monolayer was covered on the {010} facets of *m*$BiVO_4$ to form the MoS_2/$BiVO_4$ hybrid.[165] Because of the introduced interface of the MoS_2(001), the band gap of MoS_2/$BiVO_4$ (010) was narrowed to 2.05 eV, and the direct band gap of *m*$BiVO_4$ turned into indirect band gaps (Figure 16d,e); therefore, the former greatly improved the visible light adsorption, and the latter resulted in a wave function overlap to transfer the electrons form the CB of MoS_2 to the surface of *m*$BiVO_4$. Work function calculation showed a similar result—that the photogenerated electrons of MoS_2 with a relative low work function of 5.79 eV can be transferred to the {010}$BiVO_4$ surface with a relative high work function of 5.25 eV, resulting in the formation of Schottky barrier and a built-in potential with the direction from the layered MoS_2 to the {010}$BiVO_4$ surface. Moreover, the charge redistribution occurred at the interface between MoS_2 and $BiVO_4${010} facet, causing the photogenerated electrons and holes to accumulate in the $BiVO_4${010} facet and monolayered MoS_2, respectively. Therefore, an optimal photocatalytic performance for hydrogen evolution and degradation of pollutants was obtained after the introduction of the MoS_2 monolayer.

It is worth noting that the band alignment occurs not only at the interface formed between different semiconductors but also at the interface between different facets of *m*$BiVO_4$ because of its anisotropic surface band edge position. Herein, *m*$BiVO_4$ acts as a preseparation channel to achieve the spatial charge separation, which promotes the charge transfer from *m*$BiVO_4$ to another semiconductor. For instance, based on DFT calculation, Wang et al.,[166] reported that the difference in energy levels between {010} and {110} facet induced the transfer of bulk photogenerated electrons and holes to {010} and {110} facets of *m*$BiVO_4$, respectively (Figure 16h). The layered g-C_3N_4 with positive charge can be anchored on the {010} facet of *m*$BiVO_4$ through an electrostatic self-assembly process (Figure 16f,g), resulting in a built-in electric field formed between {010} facet and g-C_3N_4 with the direction from g-C_3N_4 to {010} facet of *m*$BiVO_4$ because the work function of the former was lower than that of the latter, which promoted the electron transfer from the CB of {010} facet to VB of g-C_3N_4 and then combined with the holes therein.

DOI: 10.1021/acscatal.9b03411
ACS Catal. 2020, 10, 1024−1059

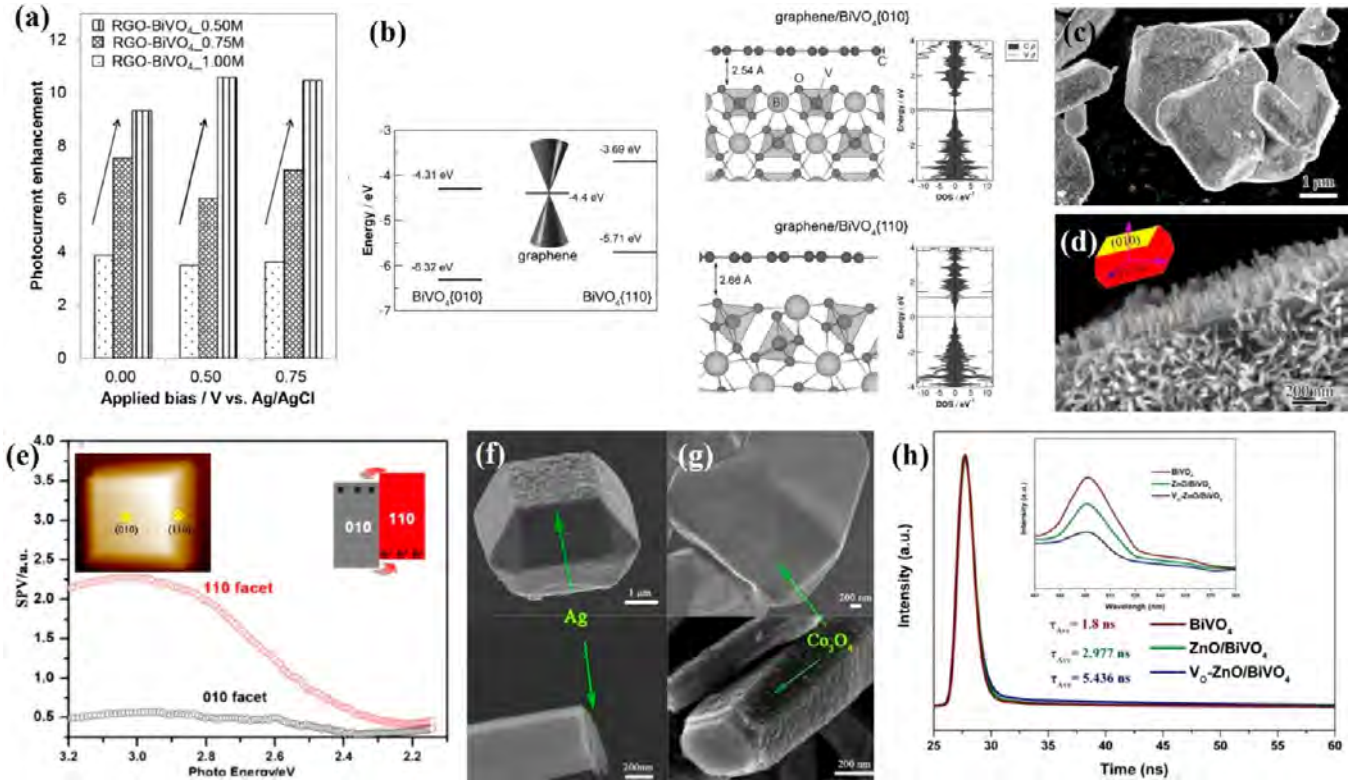

Figure 17. (a) Degree of photocurrent enhancement by coupling RGO with the three $BiVO_4$ samples, determined using three applied biases, namely 0, 0.50, and 0.75 V. (b) The band positions of graphene, {010} and {110} facets of $BiVO_4$ with respect to vacuum (graphene/$BiVO_4${010} and graphene/$BiVO_4${110} interfaces showing the optimized separations along with the DOS). Reproduced with permission from ref 82. Copyright 2016 Wiley-VCH Verlag GmbH & Co. KGaA, Weinheim. (c,d) SEM image of ZnO/$BiVO_4$. (e) Spatially resolved surface photovoltage spectra obtained at different locations on a single $BiVO_4$ crystal (inset is KPFM image of a single $BiVO_4$ crystal). SEM images of (f) Ag-$BiVO_4$ and Ag-ZnO nanorods (g) Co_3O_4–$BiVO_4$ and Co_3O_4–ZnO nanorods. (h) TRPL of $BiVO_4$, ZnO/$BiVO_4$ and V_o-ZnO/$BiVO_4$ (inset of the PL emission spectra with excited at 400 nm). Reproduced with permission from 169. Copyright 2018 Elsevier.

Therefore, the strongly reductive photogenerated electrons and strongly oxidized holes were respectively accumulated in the CB of g-C_3N_4 and the VB of {010} facet to participate in the surface redox reaction. The hybrid structure between layered g-C_3N_4 and the {010} facet of *m*$BiVO_4$ exhibited an optimal photocatalytic degradation efficiency and mineralization capacity compared with single g-C_3N_4 and *m*$BiVO_4$. Similar work was also reported by Li et al.[167] A homojunction was formed between the {040} and {110} facet of *m*$BiVO_4$ based on the driving force of a built-in electric field, followed by coupling *m*$BiVO_4$ with Bi_2WO_6 NPs to form a heterojunction. The photogenerated electrons on the {040} facet with relatively negative potential were transferred to the CB of Bi_2WO_6, and the photogenerated holes in the VB of Bi_2WO_6 were transferred to the {110} facet, which greatly promoted the charge separation, leading to an enhanced photocatalytic performance.

More recently, conductive materials with excellent electron transfer ability have been shown to play an important role in promoting charge transfer and separation. Of these conductive materials, graphene with $\pi-\pi$ conjugation structure is regarded as a good electron acceptor and transporter, showing great potential for suppressing the undesirable charge recombination in a semiconductor. For instance, Tan et al. found that the improvement degree of electron transfer efficiency in RGO/$BiVO_4$ was highly dependent on the exposure ratio of the {010} to {110} facet (Figure 17a).[82] A reliable explanation based on DFT calculation was the different electronic structures of GO/$BiVO_4${010} and GO/$BiVO_4${110} interface. Specifically, a relatively small Schottky barrier and high binding energy at GO/$BiVO_4${010} interface than that of GO/$BiVO_4${110} interface promoted the electron transfer from {010} facet to RGO sheet (Figure 17b), thereby resulting in an improved photocatalytic performance. Wang et al. reported that the photocatalytic performance of *m*$BiVO_4$ with exposed {040} facets was greatly improved after covering by thin RGO sheets,[89] which was attributed to the fact that RGO with high electrical conductivity can be served as an electron acceptor to capture the photogenerated electrons in the CB of *m*$BiVO_4$, thereby promoting the charge separation. Based on similar interface fine-tuning between *m*$BiVO_4$ and RGO, thin RGO sheets were covered on the specific facets of *m*$BiVO_4$, which was an electron-rich {010} facet.[168] During the photocatalytic reaction, the excited electrons in the CB of {010}-$BiVO_4$ can be effectively trapped by RGO, leaving more available holes in the VB of {110}-$BiVO_4$ to participate in the oxygen evolution reaction.

In addition, since the anisotropic built-in electric fields on different facets of *m*$BiVO_4$ can provide an intrinsic driving force for charge separation and transfer and the facet-dependent dipolar field can cause band bending to improve charge separation performance, it might be a feasible method to construct multielectric field to induce an additional driving force for charge transfer and separation. For example, 3D nanoarchitectures ZnO/$BiVO_4$ composite with *m*$BiVO_4$ as substrates for the heteroepitaxial growth of oriented ZnO

DOI: 10.1021/acscatal.9b03411
ACS Catal. 2020, 10, 1024−1059

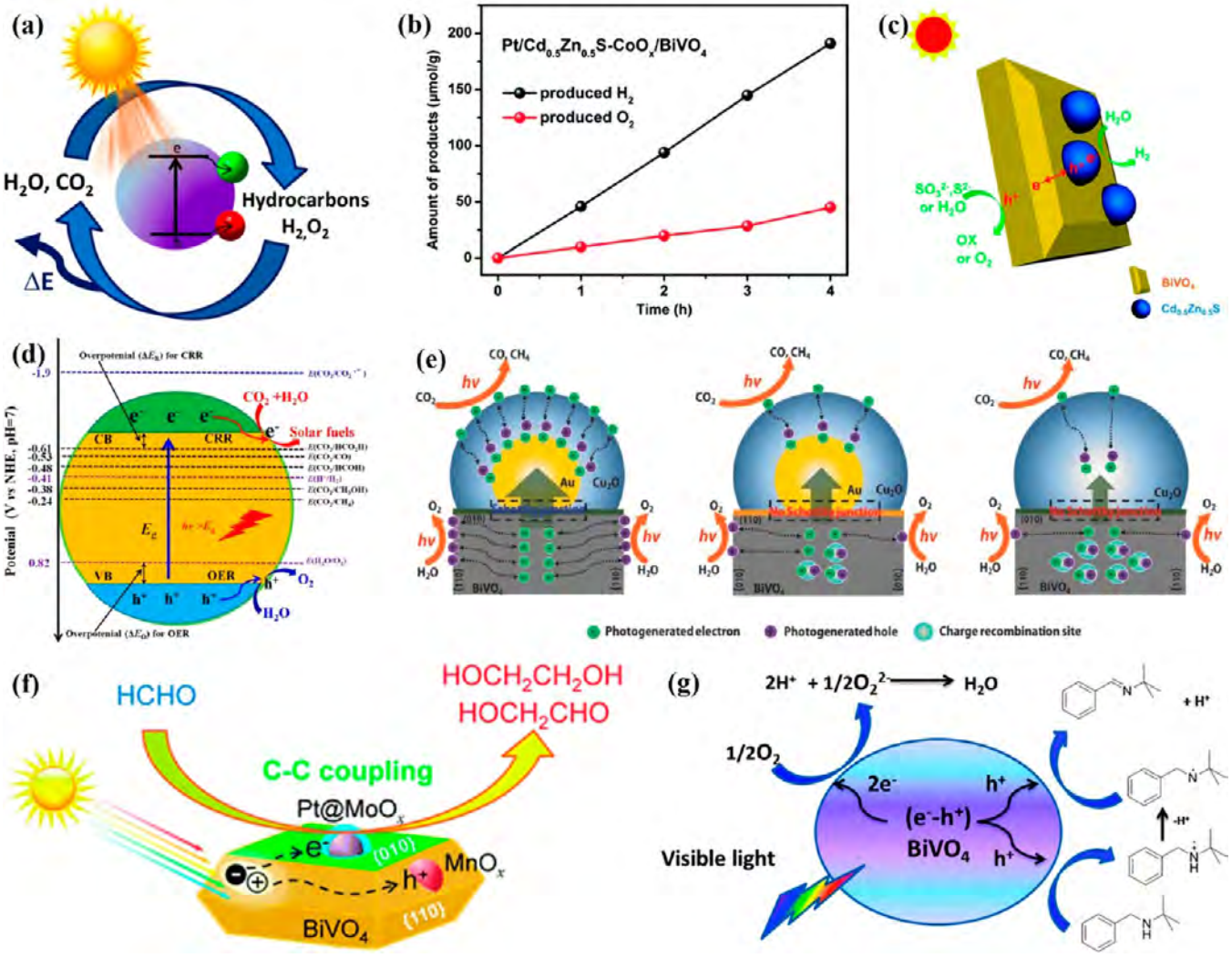

Figure 18. (a) Closed cycle of solar energy storage by conversion of H_2O and CO_2 into chemical fuels. The energy can be released on demand by a reverse reaction. Reproduced with permission from ref 170. Copyright 2018 American Chemical Society. (b) Time course of H_2 and O_2 production using Pt (3%)/$Cd_{0.5}Zn_{0.5}S$-CoO_x (0.5%)/$BiVO_4$ under visible light illumination. (c) Schematic illustration of photocatalytic water splitting for core−satellite structured Z-scheme CZS-$BiVO_4$. Reproduced from ref 172. Copyright 2018 Royal Society of Chemistry. (d) Schematic illustration of CO_2 photoreduction on a semiconductor. Reproduced with permission from ref 176. Copyright 2019 American Chemical Society. (e) Scheme to describe the carrier migration behavior from $BiVO_4$ to Cu_2O with and without Au particles deposited on the different facets of $BiVO_4$. Reproduced with permission from ref 90. Copyright 2018 Wiley-VCH Verlag GmbH & Co. KGaA, Weinheim. (f) The proposed mechanism of photocatalytic coupling of formaldehyde to ethylene glycol and glycolaldehyde over $BiVO_4$ with controllable facets and cocatalysts. Reproduced with permission from ref 75. Copyright 2017 Royal Society of Chemistry. (g) The proposed mechanism of photooxidation of amine catalyzed by $BiVO_4$. Reproduced with permission from ref 113. Copyright 2014 Royal Society of Chemistry.

nanorods on the {010} facet was prepared by Wei et al. (Figure 17c,d).[169] The Kelvin Probe Force Microscopy (KPFM) measurements demonstrated that the thermodynamically spontaneous built-in electric field drove the bulk photogenerated charge carriers to different facet, with the electrons and holes accumulated on the {010} and {110} facets of *m*$BiVO_4$, respectively (Figure 17e). The alternate stacking of positively charged cations and negatively charged anions along the *c* axis in wurtzite ZnO also led to the formation of internal electric field, resulting in the accumulation of photogenerated electrons and holes on the polar facets and nonpolar facets, respectively. Moreover, the formation energy calculation of V_o showed that the interfacial V_o were generated in the ZnO top layer when the bottom of ZnO nanorods were coupled with {110} facet of *m*$BiVO_4$, while they were in the top layer of {010} facet when ZnO nanorods grew on the {010} facet of *m*$BiVO_4$. Hence, the electrons in the bottom of ZnO would combine with the holes in {110} facet of *m*$BiVO_4$ following a Z-scheme mechanism. Such spontaneous charge separation in the interface of *m*$BiVO_4$ and ZnO can be demonstrated by the selective photoreduction of $AgNO_3$ and photooxidation of $Co(NO_3)_2$. For pure *m*$BiVO_4$, the reduction product Ag NPs and oxidation product Co_3O_4 were selectively deposited on the {010} and {110} facets, respectively. While for ZnO/$BiVO_4$ hybrid, the Ag NPs were generated on the top of ZnO nanorods (Figure 17f), and the Co_3O_4 NPs were selectively grown on the lateral {010} facets (Figure 17g). The formation of dual built-in electric field greatly promoted the separation of photogenerated charge carriers, as confirmed by the TRPL and surface photovoltage spectroscopies (Figure 17h), eventually

DOI: 10.1021/acscatal.9b03411
ACS Catal. 2020, 10, 1024−1059

resulting in an optimal photocatalytic performance for oxygen evolution.

In general, the design of the surface and interface of mBiVO$_4$ based on facet engineering represents a guiding and significant development direction in the improvement of photocatalytic performance. The major task is to facilitate the charge separation in mBiVO$_4$ and improve the charge transfer efficiency across the contact interface, whereas there is still a long way to go. First, the synthesis methods should be further optimized to achieve high controllability of the secondary parameters that might interfere with the control of the facets. Second, the contact interface formed between the new component and the existing mBiVO$_4$ is derived from the surface of mBiVO$_4$, the surface design of mBiVO$_4$ not only determines the facet structure of interface but also guides the growth of new component, which should be precisely controlled using theoretical calculations and model predictions. Finally, in mBiVO$_4$-based composites, some surfaces that are not used as active sites and interfaces that do not contribute to charge carrier transfer channels may not promote the dynamic migration of charge carriers, so the facet-engineered should be performed on a suitable surface and interface.

6. ENERGY AND ENVIRONMENTAL APPLICATIONS OF MBIVO$_4$-BASED PHOTOCATALYTIC SYSTEM

The adsorption and activation of reactant molecules as well as the charge separation and transfer efficiency depend on the arrangement of surface atoms and the crystal orientation. The surface facets determine the electronic band structures and the surface states, which offers photogenerated charge carriers with adjustable redox capabilities for photocatalytic reactions. Given that, the photocatalytic performance of the mBiVO$_4$ photocatalytic system can be improved by rationally designing the surface and interface structure, and significant progress has been made. Nevertheless, the design is not the end of facet engineering, which has to be evaluated by various photocatalytic reactions. In this section, the facet-dependent photocatalytic performance of mBiVO$_4$-based photocatalytic system for energy and environment application, and the relationship between their structures and properties will be presented.

6.1. Energy Conversion. Compared to batteries, chemical fuels with high specific energy are considered to be very promising energy storage media. Solar energy, an inexhaustible energy, has attracted an increasing attention, especially the use of this energy to induce the energetically uphill reactions to produce fuels (Figure 18a).[170] Of these reactions, the two most prominent reactions are photocatalytic water splitting and CO_2 reduction under light irradiation. In this section, we will focus on the practical application of faceted mBiVO$_4$ photocatalysts in photocatalytic hydrogen/oxygen evolution and CO_2 reaction, as well as directional synthesis of high-value-added products.

6.1.1. Photocatalytic Hydrogen Evolution. Hydrogen is recognized as a great alternative for future energy sustainability because of its high energy capacity and environmental friendliness. Photocatalytic hydrogen evolution has shown great potential for alleviating the energy crisis by converting solar energy to hydrogen. Because of coupling between V 3d, Bi 6p, and O 2p orbitals, the CB edge is also lowered (around 0 V vs NHE at pH 0), borderline for water reduction.[53] Therefore, mBiVO$_4$ cannot simultaneously reduce water and needs to operate with an electron scavenger or as part of a larger structure where the reduction proceeds elsewhere. However, the use of a scavenger will result in a decrease in the energetic benefit of the reaction, and the transfer of charge carrier to the scavenger may be prevented if their surface is occupied by large molecules as an obstacle.

Fortunately, this limitation can be ameliorated by constructing Z-scheme photocatalytic system, in which charge carriers are transferred to the second semiconductor rather than being wasted by the scavenger. Most importantly, the Z-scheme photocatalytic system is suitable for the semiconductor that can only be used for one-half-reaction. Given that, most investigation on the photocatalytic hydrogen evolution using mBiVO$_4$ is focused on the construction of Z-scheme photocatalytic system. As reported by Dong et al.,[110] the Z-scheme photocatalytic system with mBiVO$_4$, Ru-SrTiO$_3$:Rh and Fe^{3+}/Fe^{2+} as oxidation side, reduction side, and redox mediator was successfully constructed to achieve overall water splitting, with hydrogen and oxygen evolution rate of 16.7 and 8.0 μmol h^{-1}, respectively. To circumvent the limitation of liquid phase redox pairs, solid-state Z-scheme photocatalytic system exhibits more excellent potential. For instance, $La_5Ti_2CuS_5O_7$ as hydrogen photocatalyst and mBiVO$_4$ as the oxygen evolution photocatalyst were used to construct Z-scheme photocatalytic system without redox mediator for water splitting, with a solar to hydrogen energy conversion efficiency of 0.11% and apparent quantum yield of 4.9% at 420 nm.[171] In this system, the photogenerated electrons in the CB of mBiVO$_4$ were transferred to VB of $La_5Ti_2CuS_5O_7$ and combined with the holes therein with Au layer as an electron transporter. Subsequently, a direct Z-scheme photocatalyst $Cd_{0.5}Zn_{0.5}S$-BiVO$_4$ with in situ crystallized $Cd_{0.5}Zn_{0.5}S$ nanospheres on the surface of mBiVO$_4$ was constructed by charge induction assembly, which exhibited a 7.13 times higher hydrogen evolution rate than that of $Cd_{0.5}Zn_{0.5}S$ (Figure 18b).[172] This enhanced photocatalytic performance was attributed to the Z-scheme charge transfer mechanism between $Cd_{0.5}Zn_{0.5}S$ and BiVO$_4$ (Figure 18c). More importantly, with CoO_x as oxygen evolution cocatalyst, an overall water splitting was achieved without addition of any sacrificial agent.

6.1.2. Photocatalytic Oxygen Evolution. Although hydrogen evolution is the main focus of photocatalytic water splitting, the oxygen evolution half-reaction plays an equally important role in determining the efficiency of the water splitting reaction because it provides the electrons required for the hydrogen evolution reaction. However, because of the complex redox process involving four electrons, the oxygen evolution reaction is the bottleneck of photocatalytic water splitting. Surprisingly, the VB edge of mBiVO$_4$ is located at a more positive position than the potential of the oxidation half reaction and the oxygen evolution reaction is an absolute hole-involved reaction; therefore, mBiVO$_4$ exhibited an excellent potential for oxygen production from water. In addition, previous theoretical research has demonstrated that the photocatalytic performance on different facets is different because of the difference in light absorption, charge mobility, energy barrier, and water absorption.[67] Given that, facet engineering with respect to improve the utilization of favorable facet of mBiVO$_4$ is expected to obtain more excellent photocatalytic performance for oxygen evolution. For instance, Li et al. prepared Pt/Co_3O_4/BiVO$_4$ photocatalysts by selective deposition of Pt and Co_3O_4 on the {010} and {110} facet of mBiVO$_4$ for photocatalytic oxygen evolution under 300 W Xe lamp irradiation with IO_3^- as electron acceptors.[85] Due to the

DOI: 10.1021/acscatal.9b03411
ACS Catal. 2020, 10, 1024−1059

Table 1. List of Facet-Dependent Photocatalytic Performance of *m*$BiVO_4$-Based Photocatalysts for Oxygen Evolution

photocatalyst	reaction condition (light source, sacrificial agent, concentration of photocatalyst)	performance (μmol h^{-1}) AQY	ref
Pt/MnO_x/$BiVO_4$	300 W Xe lamp ($\lambda \geq 420$ nm); 0.02 M $NaIO_3$; 1 g L^{-1}	97.5	65
$BiVO_4$ with different exposure ratio of {040} to {110} facets	300 W Xe lamp ($\lambda > 420$ nm); 0.05 M $AgNO_3$; 1.5 g L^{-1}	310	68
$BiVO_4$ with exposed {001} facets	300 W Xe lamp ($\lambda > 420$ nm); 0.05 M $AgNO_3$; 0.37 g L^{-1}	559	80
$BiVO_4$ with different {010}/{011} ratio	300 W Xe lamp ($\lambda \geq 420$ nm); 10 mM $Fe(NO_3)_3$; 0.67 g L^{-1}	280	81
Pt/Co_3O_4/$BiVO_4$	300 W Xe lamp ($\lambda \geq 420$ nm); 0.02 M $NaIO_3$; 1 g L^{-1}	160.3	85
30-faceted $BiVO_4$	300 W Xe lamp ($\lambda > 420$ nm); 0.02 M $NaIO_3$; 0.625 g L^{-1}	57.0 18.3% at 430 nm	98
$Bi_xY_{1-x}VO_4$	300 W Xe lamp ($\lambda > 400$ nm);1 M $NaNO_2$; 2.5 g L^{-1}	0.6	105
2D $BiVO_4$	300 W Xe lamp ($\lambda > 420$ nm); 0.05 M $AgNO_3$; 0.4 g L^{-1}	107.4 26.1% at 420 nm	110
$BiVO_4$	300 W Xe lamp ($\lambda > 420$ nm); 0.05 M $AgNO_3$; 2 g L^{-1}	162.5	116
$BiVO_4$ with different {010} and {110} facets ratio	300 W Xe lamp; 0.02 M $AgNO_3$; 0.33 g L^{-1}	O_2: 2.333	118
{040}$BiVO_4$/Ag_2O	UV: 500 W Hg lamp, vis: 350 W Xe lamp ($420 < \lambda < 780$ nm), NIR: 300 W Xe lamp ($\lambda > 800$ nm); 0.01 M $AgNO_3$; 0.5 g L^{-1}	vis: 71.47 solar light: 7.76	161
ZnO/$BiVO_4$	300 W Xe lamp ($\lambda > 420$ nm); 0.05 M $AgNO_3$; 0.5 g L^{-1}	68 5.0% at 450 nm	169
g-C_3N_4@Ag/{040}$BiVO_4$	350 W Xe lamp (λ>420 nm); 0.2 M $NaIO_3$; 1 g L^{-1}	14.68	173
W- and Mo-doped $BiVO_4$ oriented along {040} facet	plasma lamp (100 mW cm^{-2}); 50 mM $AgNO_3$; 0.91 g L^{-1}	W-$BiVO_4$: 0.686 Mo-$BiVO_4$: 0.942	174
FeO_x/{110}$BiVO_4$	LED light source ($\lambda \geq 460$ nm);10.0 mM $NaIO_3$; 5 g L^{-1}	3.1	175

synergistic utilization of Schottky junctions on {010} facets of *m*$BiVO_4$ to facilitate the charge separation and the hole trapping of Co_3O_4 on {110} facets, the oxygen evolution rate was dramatically improved than that with randomly deposited cocatalysts, with an oxygen production rate of more than 160 μmol h^{-1}. Wei et al. prepared ZnO/$BiVO_4$ hierarchical nanoarchitectures for photocatalytic oxygen evolution under a 300 W Xe lamp irradiation with $AgNO_3$ solution as the electron sacrificial agent.[169] Because of the facet-dependent multielectric field effect between ZnO nanorods and $BiVO_4$-{010} facets, a remarkable oxygen evolution rate of 68 μmol·h^{-1} was achieved, corresponding to more than 1 order of magnitude improved apparent quantum yield (AQY, 5.0% at 450 nm) compared with single *m*$BiVO_4$. Moreover, 30-faceted $BiVO_4$ composed of {132}, {321}, and {121} high-index facets exhibited a 3−5 fold improvement in oxygen production compared with its low-index counterparts, and the AQY without an external electron supply (18.3% at 430 nm) was an order of magnitude higher than that of the catalysts reported hitherto.[98] This excellent photocatalytic oxygen evolution performance was attributed to the energetically favorable water dissociation on the high-index surfaces and the notable reduction in the overpotential of oxygen evolution reaction relative to that of the low-index surfaces. Furthermore, other investigation on facet-dependent photocatalytic performance of *m*$BiVO_4$-based photocatalysts for oxygen evolution are listed in Table 1.

6.1.3. Photocatalytic CO_2 Reduction. Photocatalytic CO_2 reduction into carbon-containing fuels based on semiconductor photocatalysts, a multielectron transfer process, is regarded as a sustainable, economical technique for settling the global energy crisis and reducing the greenhouse effect. Whether the reduction product is CO, CH_4, HCHO, CH_3OH, or HCOOH depends on the reduction potentials (Figure 18d).[176] Example such as the minimum reduction potentials of −0.24 is required for the photocatalytic CO_2 reduction into CH_4, while −0.38, −0.48, −0.53, and −0.61 V are needed for the generation of CH_3OH, CH_4, CO, and HCOOH, respectively. Although the CB potential of *m*$BiVO_4$ is too low to reduce CO_2 under light irradiation, the preparation of *m*$BiVO_4$ with a suitable nanosized structure has proven to be a highly selective photocatalyst for photocatalytic CO_2 reduction as the CB potential can be effectively upshifted due to quantum size effects. A good demonstration was the selective production of ethanol by photocatalytic reduction of CO_2 in water in the presence of *m*$BiVO_4$ photocatalyst. The conversion of CO_2 to CO_3^{2-} results in a lower potential of about 0.7 eV, which makes it possible to anchor CO_3^{2-} on the surface of Bi^{3+} sites by forming Bi−O bond.[177] Therefore, these CO_3^{2-} adsorbed on the surface can efficiently receive photogenerated electrons from the V 3d-block bands of *m*$BiVO_4$, eventually leading to the generation of ethanol. Based on a similar mechanism, Mao et al. reported the selective generation of methanol by photocatalytic reduction of CO_2 with lamellar $BiVO_4$ as a photocatalyst under visible light irradiation.[178] Interestingly, the methanol yield was greatly increased after adding NaOH solution in the photocatalytic system, which was attributed to the fact that the solubility of CO_2 in caustic solution was significantly higher than in water, and OH^- can be used as a stronger hole scavenger.

However, the efficiency of photocatalytic CO_2 reduction by single *m*$BiVO_4$ is still relatively poor, which has spurred more research to focus on the development of *m*$BiVO_4$-based composites. Similar to photocatalytic hydrogen evolution, the Z-scheme photocatalytic system is also widely used to enhance the photocatalytic performance of CO_2 reduction. For instance, Zhou and co-worker reported that the $BiVO_4$−Au-Cu_2O composites prepared by anchoring the Au−Cu_2O composite onto the {010} facet of *m*$BiVO_4$ exhibited an excellent photocatalytic performance toward CO_2 reduction, with 3 and 5 times greater CH_4 production rate than that of

DOI: 10.1021/acscatal.9b03411
ACS Catal. 2020, 10, 1024−1059

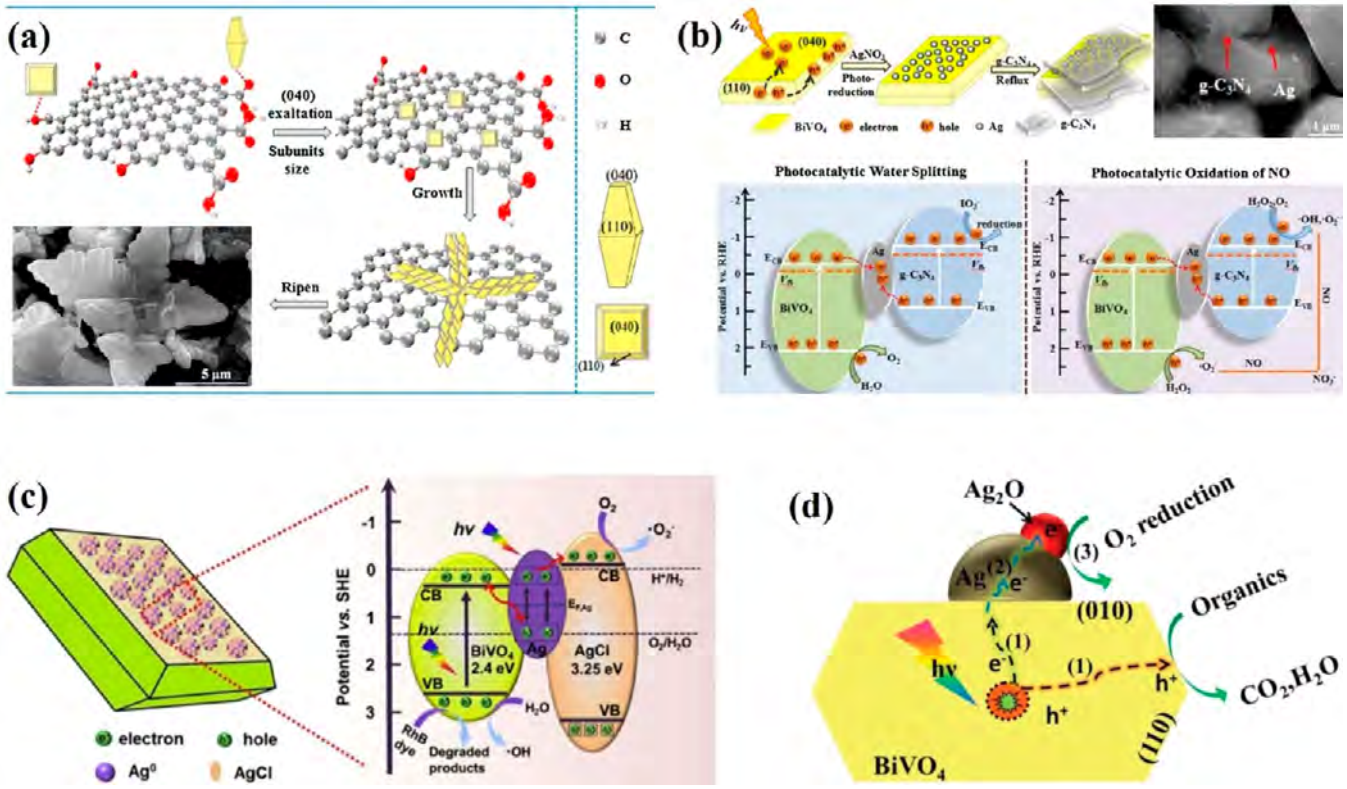

Figure 19. (a) Schematic illustration of the proposed formation mechanism of 3D flower-like *m*$BiVO_4$/reduced graphene oxide nanosheets superstructure. Reproduced with permission from ref 183. Copyright 2016 Elsevier. (b) Schematic illustration of the formation process of the Z-scheme g-C_3N_4@Ag/$BiVO_4$ photocatalysts, typical SEM images of the as-synthesized g-C_3N_4@Ag/$BiVO_4$ photocatalysts, and energy band diagrams and proposed Z-scheme schematic descriptions of the mechanisms of the g-C_3N_4@Ag/$BiVO_4$ photocatalyst for the photocatalytic oxidation of (left) water and (right) NO under visible light irradiation. Reproduced with permission from ref 173. Copyright 2018 Elsevier. (c) The schematic diagram illustration of Ag@AgCl decorated on the {040} crystal facet of $BiVO_4$ and the proposed Z-scheme mechanism photodegradation of RhB dye over Ag@AgCl/$BiVO_4$ heterostructure photocatalyst under visible light irradiation. Reproduced with permission from ref 27. Copyright 2015 Elsevier. (d) Schematic drawing illustrating the possible photocatalytic mechanism of Ag_2O−Ag/$BiVO_4$ photocatalyst: (1) orientation transport of photogenerated carriers; (2) interfacial transfer and (3) interfacial catalytic reaction of photogenerated electrons. Reproduced with permission from ref 187. 2018 Royal Society of Chemistry.

$BiVO_4${110}−Au-Cu_2O and $BiVO_4${010}-Cu_2O, respectively.[90] This enhanced photocatalytic performance was attributed to the efficient charge separation and transfer, as shown in Figure 18e. In $BiVO_4${010}−Au-Cu_2O, the Schottky junction at the interface of $BiVO_4${010} and Au accelerated the electrons transfer from $BiVO_4${010} to Cu_2O, resulting in the photogenerated electrons and holes with prolonged lifetime were accumulated in the CB of Cu_2O and the VB of $BiVO_4$, respectively. While there is an electron diffusion layer instead of Schottky junction was formed in $BiVO_4${110}-Au-Cu_2O and $BiVO_4${010}-Cu_2O, which resulted in slow and inefficient electron transfer at the interface. Interestingly, Iwase and co-workers constructed a RGO-bridged Z-scheme photocatalytic system to achieve photocatalytic overall water splitting and CO_2 reduction, in which CoO_x-loaded *m*$BiVO_4$ was used as oxygen evolution photocatalyst and metal sulfides were used to induce the hydrogen evolution and CO_2 reduction reaction.[179]

In theory, the band structure of semiconductor needs to have two characteristics in order to achieve photocatalytic CO_2 reduction by water: (i) the CB potential must be much higher than the proton-assisted multielectron reduction potential of CO_2, (ii) the VB edge should be much more positive than the four-electron water oxidation potentials. Compared with two electron-involved water reduction reactions, CO_2 reduction reactions involving multielectrons and protons are more favorable because of the lower thermodynamic barriers, especially CO_2 reduction to methanol and methane because their reduction potentials are even lower than that of photocatalytic hydrogen evolution.[180] In principle, all photocatalysts used for photocatalytic hydrogen evolution should be suitable for photocatalytic reduction of CO_2 to methanol and methane. However, since the thermodynamic potentials of the products of photocatalytic CO_2 reduction are very similar, one difficulty is how to obtain a target product with high selectivity. To overcome the above limitations, the two-electron participating H^+ reduction reaction as a main hydrogen evolution reaction pathway must be suppressed, which can be achieved by using a multifunctional cocatalyst and selecting a multiple electron reduction pathway instead of a single electron process.[181]

Apart from above energy application, *m*$BiVO_4$ is also regarded as a promising photocatalyst in the conversion of low value-added products into high value-added products. For instance, Zhu et al. investigated the selective conversion of methane to methanol using two $BiVO_4$ microcrystals, bipyramidal $BiVO_4$ composed of {102} and {012} facets and platelet $BiVO_4$ with exposed {001} facets as top and bottom.[104] The bipyramidal samples exhibited higher activity for CH_4 to CH_3OH compared with $BiVO_4$ platelets, with a mass activity 100 μmol h^{-1} g^{-1} and a selectivity above 80%,

DOI: 10.1021/acscatal.9b03411
ACS Catal. 2020, 10, 1024−1059

Table 2. List of Facet-Dependent Photocatalytic Performance of *m*$BiVO_4$-Based Photocatalysts for Organic Degradation

photocatalyst	reaction condition (light source, concentration of pollutants and photocatalyst)	pollutants, photocatalytic degradation efficiency, (reaction time) kinetic rate constant	ref
Ag@AgCl/{040}$BiVO_4$	500 W Xe lamp ($\lambda \geq 420$ nm); 10 mg L^{-1}; 2 g L^{-1}	RhB: 100% (35 min) 0.12 min^{-1}	27
$BiVO_4$ nanosheets with exposed {010} facets	sunlight; 2.09 × 10^{-4} M; 5 g L^{-1}	*N*,*N*,*N*′,*N*′-tetraethylated rhodamine: 100% (3 h)	56
$BiVO_4$ oriented along {040} facets	500 W Xe lamp ($\lambda \geq 420$ nm); 10 mg L^{-1}; 1 g L^{-1}	MB: 96.97% (3 h)	70
$BiVO_4$ with exposed {040} facets	300 W Xe lamp ($420<\lambda<800$ nm); 3.1 × 10^{-5} M; 1 g L^{-1}	MB: 100% (1 h)	78
Pt/Co_3O_4/$BiVO_4$	300 W Xe lamp ($\lambda \geq 420$ nm); 10 mg L^{-1}; 0.5 g L^{-1}	RhB: 0.0631 min^{-1} MO: 0.0462 min^{-1}	85
{040}$BiVO_4$/$BiPO_4$	500 W Xe lamp ($\lambda \geq 420$ nm); RhB:10 mg L^{-1}; MNZ:5 mg L^{-1}; 0.5 g L^{-1}	RhB: 85.5% (6 h) 0.2981 h^{-1} MNZ: 75.5% (2 h) 0.062 h^{-1}	88
rGO/{040}$BiVO_4$	300 W Xe lamp (λ>420 nm); 10 mg L^{-1}; 0.5 g L^{-1}	MB: 94% (2 h) 0.021 min^{-1}	89
Ag_3PO_4/{040}$BiVO_4$	300 W Xe lamp ($\lambda \geq 420$ nm); 10 mg L^{-1}; 0.5 g L^{-1}	MB: 75% (0.5 h) 0.269 min^{-1}	91
$BiVO_4$-110-TiO_2	500 W Xe lamp ($\lambda \geq 422$ nm); RhB:10 mg L^{-1}, 3 g L^{-1}; 4-nonylphenol:1 × 10^{-4} M, 1.5 g L^{-1}	RhB: 1.19 h^{-1} 4-nonylphenol: 3.07 h^{-1}	92
Ag@AgBr/$BiVO_4$/Co_3O_4	350 W Xe lamp (λ>420 nm); 10 mg L^{-1}; 1 g L^{-1}	RhB: 0.1112 min^{-1}	93
$BiVO_4$ with exposed {111} facets	300 W Xe lamp (λ > 420 nm); 1 × 10^{-5} M; 0.1 g L^{-1}	RhB: 55.1% (75 min) 10.75 × 10^{-3} min^{-1}	94
$BiVO_4$ with coexposed {010} and {110} facets	500 W Xe lamp ($\lambda \geq 420$ nm); RhB:5 mg L^{-1}; MB:10 mg L^{-1};	RhB: 53.8% (3 h) 0.00376 min^{-1} MB: 70.2% (3 h) 0.00561 min^{-1}	95
$BiVO_4$ with exposed {010} facets	300 W Xe lamp; 10 mg L^{-1}; 1 g L^{-1}	MB: 97.13% (4h) 2.301 × 10^{-4} s^{-1}	96
{040}$BiVO_4$/{001}BiOBr	500 W Xe lamp (λ>420 nm); 10 mg L^{-1}; 0.01 g L^{-1}	RhB: 98.9% (0.5 h)	107
$BiVO_4$ with {010}-dominant	300 W Xe lamp (λ>420 nm); 0.065 mM; 1 g L^{-1}	2,4-D: 0.021 min^{-1}	117
$BiVO_4$ with different {010} and {110} facets ratio	500 W Xe lamp; 4.29 × 10^{-5} M; 0.3 g L^{-1}	Thymol blue: 0.394 min^{-1}	118
N-doped $BiVO_4$ with exposed {040} facets	350 W Xe lamp; 2 × 10^{-5} M; 1 g L^{-1}	RhB: 97% (4 h)	134
$BiVO_4$ nanorods grown along {010} direction	350 W Xe lamp (λ>420 nm); 10 mg L^{-1}; 3.89 g L^{-1} (12 mM)	RhB: 0.141 min^{-1}	144
$BiVO_4$ with exposed {001} facets	500 W Xe lamp; 20 g L^{-1}; 1 g L^{-1}	OTC: 95.83% (0.5 h)	145
{040}$BiVO_4$/Ag_3PO_4/PANI	300 W Xe lamp ($\lambda \geq 420$ nm), 10 mg L^{-1}; 1 g L^{-1}	CIP: 85.92% (1 h) 0.00894 L mg^{-1} min^{-1}	150
$BiVO_4$−Au@CdS	500 W Xe lamp (λ>420 nm); RhB (5 mg L^{-1}); 1 g L^{-1} 4-NP (2 × 10^{-4} M); 0.5 g L^{-1}	RhB: 0.0130 min^{-1} 4-NP: 0.0430 min^{-1}	158
{040}$BiVO_4$/Ag_2O	UV: 500 W Hg lamp, vis: 350 W Xe lamp ($420<\lambda<780$ nm), NIR: 300 W Xe lamp (λ>800 nm); MB: 10 mg L^{-1}; 0.625 g L^{-1}	vis: 94% (40 min) NIR: 91% (80 min)	161
g-C_3N_4/{010} $BiVO_4$	500 W Xe lamp (λ>420 nm); 5 × 10^{-6} M; 1 g L^{-1}	RhB: 96.03% (0.5 h) 0.0673 min^{-1}	166
$BiVO_4$/BiOI	500 W Xe lamp (λ>420 nm); 0.02 mM; 0.6 g L^{-1}	RhB: 97% (3 h) 1.104 h^{-1}	188
$BiVO_4$/Bi_2WO_6	500 W Xe lamp (λ>270 nm); 10 mg L^{-1}; 1 g L^{-1}	MO: 87% (2 h) 0.0046 min^{-1}	189
Ag_3PO_4/Ag/$BiVO_4${040}	300 W Xe lamp ($\lambda \geq 420$ nm); 10 mg L^{-1}; 0.5 g L^{-1}	TC: 94.96% (1 h)	190
{010}$BiVO_4$/Ag/CdS	500 W Xe lamp ($\lambda \geq 420$ nm); 5 mg L^{-1}; 1 g L^{-1}	RhB: 90% (2.5 h) 0.0145 min^{-1}	191
Ag-RGO@{010}$BiVO_4$/ RGO@{110} $BiVO_4$	UV: 500 W Xe lamp, Vis: 300 W Xe lamp ($420<\lambda<780$ nm), NIR: 300 W Xe lamp (λ>800 nm); RhB (10 mg L^{-1}); 1 g L^{-1}	vis: 98.3% (1.5 h) 0.02409 min^{-1} NIR: 66.1% (3 h) 0.00524 min^{-1}	192

which was attributed to the fact that bipyramidal $BiVO_4$ with well-defined facets can provide a larger surface to extract holes for CH_4 oxidation. Interestingly, $BiVO_4$ platelets showed the highest activity for total oxidation activity, the CO_2 yield was higher than that of bipyramidal $BiVO_4$, but CH_3OH yield was lower, owing to more efficient collection of electrons by the {001} facets in $BiVO_4$ platelets. The facet-dependent photocatalytic activity of *m*$BiVO_4$ was also been reported by Xie et

DOI: 10.1021/acscatal.9b03411
ACS Catal. 2020, 10, 1024−1059

al.,[75] and $BiVO_4$ with an equal fraction of {010} and {110} facets showed the highest performance for photocatalytic coupling of formaldehyde to ethylene glycol and glycoaldehyde (Figure 18f). Likewise, Yuan et al. reported that the photocatalytic performance of $m$$BiVO_4$ for oxidation of amines was highly dependent on the exposure ratio of {040} to {110} facet, of which $BiVO_4$ with aliquots of {040} and {110} facet showed the highest activity and selectivity for the oxidation of amines to imines (Figure 18g).[113]

6.2. Environmental Restoration. The task of applying photocatalysis for environmental remediation is to achieve air purification and wastewater decontamination. In terms of air purification, $m$$BiVO_4$ with strong photo-oxidation ability have been demonstrated to exhibit great performance for high concentration NO oxidation with the help of H_2O_2 under visible light irradiation (Figure 19a).[182,183] The excellent performance promoted Ou and co-worker to use $m$$BiVO_4$ to investigate the oxidation of water to produce oxygen and NO in flue gas to NO_3^- under visible light irradiation, making the material possess versatility.[173] They prepared g-C_3N_4@Ag/$BiVO_4$ photocatalyst by selectively depositing Ag on the {040} facet of $m$$BiVO_4$ and then covering it with g-C_3N_4 (Figure 19b). The prepared sample exhibited an improved photocatalytic performance for water and NO oxidation, with the oxygen evolution rate of 14.68 μmol h^{-1} and NO removal ratio of 83% after 150 min light irradiation, respectively. More importantly, no NO_2 was detected in the photocatalytic process. In addition, the removal of another type of atmospheric environmental pollutants, volatile organic compounds, can also be achieved by photocatalysis with $m$$BiVO_4$ or $m$$BiVO_4$-based composites as photocatalyst. Recent work reported by Chen et al. demonstrated that gaseous benzene can be efficiently degraded by $m$$BiVO_4$/$\alpha$-$Fe_2O_3$ photocatalyst, with the degradation and the mineralization rate of 66.87% and 76.5%, respectively.[184] Sun et al. reported that coral-like $m$$BiVO_4$/g-$C_3N_4$ composite exhibited improved photocatalytic performance for toluene removal under visible light, with a 3.2 and 4.5 times greater degradation rate constant and mineralization rate than g-C_3N_4, respectively.[185] To solve the limitation of reutilization of powder photocatalyst, $BiVO_4$ quantum tubes/reduced graphene oxide aerogel with $BiVO_4$ quantum tubes loaded on reduced graphene oxide (RGO) aerogel was prepared, which showed excellent photocatalytic performance for formaldehyde degradation.[186]

Apart from air purification, photocatalysis is also recognized as a promising technology for organic removal in water since the functional groups of organic compounds may be oxidized, allowing transformation or degradation of the organic pollutants into less harmful substances. $m$$BiVO_4$ with a lower VB potential of +2.5 eV due to the hybridization of Bi 6s−O 2p orbitals can provide sufficient potential not only to water oxidization but also to various organic compounds degradation.[56] Most importantly, faceted $m$$BiVO_4$ can act as preseparation channel to achieve spatial separation of photogenerated charge carriers, which can increase the number of available photogenerated carriers to directly oxidize the organic or participate in the generation of reactive oxygen species such as superoxide ($\cdot O_2^-$) and hydroxyl ($\cdot$OH) radicals, thereby improving the photocatalytic performance. For example, Li et al. prepared Ag@AgCl/$BiVO_4$ composites with Ag@AgCl decorated on {040} facet of $m$$BiVO_4$, which exhibited a 300 times higher photocatalytic performance for RhB degradation compared with single $m$$BiVO_4$.[27] This improved performance was attributed to the synergistic effect of the active facets and the Z-scheme heterojunction as well as the SPR-effect of Ag NPs (Figure 19c). Likewise, Wang et al. reported that the photocatalytic performance of $m$$BiVO_4$ was greatly improved after selective deposition of Ag_2O−Ag on the {010} facet of $m$$BiVO_4$.[187] In this hybrid structure, Ag NPs can effectively extract the photogenerated electrons from the {010} facet of $m$$BiVO_4$ and then transfer to Ag_2O, while the holes in the {110} facet of $m$$BiVO_4$ can directly oxidize the organics, thereby resulting in an optimal photocatalytic performance (Figure 19d). Furthermore, other investigation on facet-dependent photocatalytic performance of $m$$BiVO_4$-based photocatalysts for organic removal are listed in Table 2.

Overall, both air purification and wastewater decontamination can be achieved by semiconductor photocatalysis, but the following considerations remain. Although organic can be efficiently degraded by photocatalysis, incomplete mineralization of organic leads to the production of various byproducts, and one problem that should be paid attention to is the ecotoxicity of these byproducts. To lower the environmental risks of byproducts, the following two aspects should be considered: first, the degree of oxidation of byproducts gradually increases as the reactions proceeds, it is best to determine whether these byproducts can be oxidized by radicals in the photocatalytic system according to the oxidation potential of the pollutants; next, the possible attack sites of radicals should be determined on the basis of the molecular structure of the target pollutants, and the mineralization pathway should be analyzed to assess the toxicity of byproducts. What's more, in term of applicability of water decontamination by photocatalysis, several factors should be considered, such as the real water environment, the activity and recyclability of photocatalyst, operation costs, and technological process.

7. CONCLUSIONS AND PERSPECTIVES

In the past few decades, an increasing number of studies with respect to the $m$$BiVO_4$ semiconductor have laid a rich theoretical foundation for its design, development, and application. The continuous breakthrough in the synthesis and modification of $m$$BiVO_4$ photocatalysts has undoubtedly brought about more optimized design and enhanced photocatalytic performance, of which surface and interface design of $m$$BiVO_4$ based on facet engineering is a promising and instructive development direction toward the enhancement of photocatalytic performance. In this Review, some of latest advances in facet engineering that have been performed to control the surface of single $m$$BiVO_4$ semiconductor systems and to design the surface/interface structures of $m$$BiVO_4$-based composites, including element doping and heterojunction construction, are systematically elaborated, which facilitates an in-depth understanding of the underlying relationship between facet-dependent semiconductors and photocatalytic performance. Moreover, the design is not the end of facet engineering, which has to be evaluated by various photocatalytic reactions. Therefore, the photocatalytic application achievements of $m$$BiVO_4$ photocatalytic system in energy conversion and environmental remediation are also summarized. We hope that this comprehensive Review with respect to the facet engineering of $m$$BiVO_4$ can provide guidance for further exploring the great potential of $m$$BiVO_4$-based photocatalytic system in energy and environment-related applications.

DOI: 10.1021/acscatal.9b03411
ACS Catal. 2020, 10, 1024−1059

Since the photocatalytic reaction is a process in which photogenerated electron and holes participate in the oxidation and reduction reactions on the catalyst surface. The facets forming the surface of single mBiVO$_4$ is a key parameter that should be considered because the surface facet affects the adsorption and activation of reactants, and the redox ability of photogenerated carriers is largely determined by the electronic band structure of facets. When single mBiVO$_4$ is coupled with another component such as a semiconductor, metal, or carbon material, the situation becomes complicated as the existence of coexisting component. In such hybrid structure, the excited electrons and holes will be transferred from the bulk to the interface and accumulate therein, which further determines the charge transfer across the interface. More importantly, since the driving force of the interface charge transfer is derived from the potential difference of the contact facets, the compatibility of contact facet determines the degree of interface electronic coupling associated with charge transfer efficiency. Therefore, based on the complexity of the case, it is not enough to just expatiate into being advanced synthesis methods, facet-engineered surface, and interface design. As for single mBiVO$_4$, the photocatalytic performance can be remarkably improved by selectively exposing high-active facet, enlarging the proportion of highly active facet or optimizing the ratio of adjacent facet. While for the modification of single mBiVO$_4$ semiconductor, the major target of facet engineering is to facilitate the charge transfer across the interface. In addition to rationally exposing the crystal facets with the optimal photocatalytic performance on the surface of mBiVO$_4$, selecting suitable crystal facets to form an interface with other components to promote charge transfer across the interface is another promising and important development direction. However, the current research in this direction is still immature, mainly because the mechanism of interface charge transfer and the specific role of exposed crystal faces cannot be clearly explained at the atomic level.

Although theoretical design and experimental studies based on facet-dependent mBiVO$_4$ have evolved considerably, studies in this field are still in tehir infancy, giving full play to the role of facet engineering in the field of photocatalysis remains a problem that overwhelming the scientific community. For one thing, the narrow visible light response region and low charge separation efficiency are always the primary factors limiting photocatalytic performance. In order to achieve extensive breakthrough in photocatalytic performance for practical environmental and energy application, element doping along the oriented facet and constructing heterojunction provide promising directions to solve the aforementioned problems. Additionally, element doping can improve the absorption region of visible light by altering the surface atomic structure of mBiVO$_4$, and previous studies have demonstrated that the photogenerated electrons and holes are transferred to the {010} and {110} facets, respectively. Therefore, element doping along the oriented facet can not only reduce the band gap but also maximize oxidation ability of holes or reduction ability of electrons based on facet engineering. For another thing, constructing heterojunction is favorable for the efficient charge transfer through forming an interface between different facets to prolong the lifetime of photogenerated electrons and holes, resulting in more available electrons and holes participating in the surface redox reaction. To achieve the above goal, advanced synthesis techniques that take into account secondary factors affecting the surface facet exposure of mBiVO$_4$ are paramount. It is important to note that the new component should be coupled to the suitable surface facet of mBiVO$_4$ to form a rational interface.

The major challenge that advanced synthesis techniques need to overcome is the lattice mismatch in the interface formation process because the interface determines the interfacial structure and electronic coupling. Nonepitaxial growth method involving both nucleation and growth processes is a development direction worthy of further exploration because these two processes require existing components to provide strong binding sites to form new components, which greatly decreases the possibility of lattice mismatch. In the next place, the current synthetic approaches are limited by the morphology-controlling agents, up to now, the use of capping agents on some facets of mBiVO$_4$ is still a conventional method to achieve selective exposure of facets. However, the capping agent remaining on the surface of mBiVO$_4$ will inevitably affect the interface structure. In addition, current studies have neither determined whether the active crystal facet is highly exposed nor clarified the mechanism by which high active crystal facet preferentially grow. It is still a challenge to predict the outcome of the chemical synthesis of mBiVO$_4$. Given that, the theoretical prediction on the exposed facets of mBiVO$_4$, especially those related to photocatalytic performance, are critical to the microscopic mechanism of experimental observation.

Once more, the fundamental understanding of the transfer process of photogenerated carriers across the interface in the heterostructure is the most important, in order to maximize the reducing ability of photogenerated electrons and the oxidizing ability of holes. In situ observation is critical for investigating interfacial charge kinetics on surface faceted photocatalyst, which requires the characterization techniques with high spatial, spectral, and temporal resolutions. Moreover, the combination of theoretical simulation and calculation can analyze various factors affecting photocatalytic performance, which provides important guidance for the design of faceted-materials and greatly improve the efficiency in the design and synthesis of photocatalyst. At length, given the multi-disciplinary nature of research in this area, collaborative research across different disciplines, namely materials science, physical chemistry, and surface science, is also critical to transcending its knowledge boundaries to develop efficient and sustainable photocatalytic systems.

AUTHOR INFORMATION

Corresponding Author

*Tel.: +86-731-88822829. Fax: +86-731-88822829. E-mail: huangdanlian@hnu.edu.cn.

ORCID

Danlian Huang: 0000-0003-4955-5755

Notes

The authors declare no competing financial interest.

ACKNOWLEDGMENTS

This study was financially supported by the Program for the National Natural Science Foundation of China (51879101, 51579098, 51779090, 51709101, 51521006, 51809090, 51278176, 51378190), the National Program for Support of Top-Notch Young Professionals of China (2014), the Program for Changjiang Scholars and Innovative Research Team in University (IRT-13R17), and Hunan Provincial Science and

DOI: 10.1021/acscatal.9b03411
ACS Catal. 2020, 10, 1024−1059

Technology Plan Project (2018SK20410, 2017SK2243, 2016RS3026), and the Fundamental Research Funds for the Central Universities (531109200027, 531107051080, 531107050978, 531107051205).

REFERENCES

(1) Snyder, E. G.; Watkins, T. H.; Solomon, P. A.; Thoma, E. D.; Williams, R. W.; Hagler, G. S. W.; Shelow, D.; Hindin, D. A.; Kilaru, V. J.; Preuss, P. W. The Changing Paradigm of Air Pollution Monitoring. *Environ. Sci. Technol.* **2013**, *47*, 11369−11377.

(2) Xie, G.; Zhang, K.; Guo, B.; Liu, Q.; Fang, L.; Gong, J. Graphene-Based Materials for Hydrogen Generation from Light-Driven Water Splitting. *Adv. Mater.* **2013**, *25*, 3820−3839.

(3) Wang, R.-Z.; Huang, D.-L.; Liu, Y.-G.; Zhang, C.; Lai, C.; Zeng, G.-M.; Cheng, M.; Gong, X.-M.; Wan, J.; Luo, H. Investigating the Adsorption Behavior and the Relative Distribution of Cd^{2+}, Sorption Mechanisms on Biochars by Different Feedstock. *Bioresour. Technol.* **2018**, *261*, 265−271.

(4) Xue, W.; Peng, Z.; Huang, D.; Zeng, G.; Wan, J.; Xu, R.; Cheng, M.; Zhang, C.; Jiang, D.; Hu, Z. Nanoremediation of Cadmium Contaminated River Sediments: Microbial Response and Organic Carbon Changes. *J. Hazard. Mater.* **2018**, *359*, 290−299.

(5) Huang, D.; Wang, X.; Zhang, C.; Zeng, G.; Peng, Z.; Zhou, J.; Cheng, M.; Wang, R.; Hu, Z.; Qin, X. Sorptive Removal of Ionizable Antibiotic Sulfamethazine from Aqueous Solution by Graphene Oxide-Coated Biochar Nanocomposites: Influencing Factors and Mechanism. *Chemosphere* **2017**, *186*, 414−421.

(6) Kim, D. S.; Park, Y. S. Comparison Study of Dyestuff Wastewater Treatment by the Coupled Photocatalytic Oxidation and Biofilm Process. *Chem. Eng. J.* **2008**, *139*, 256−263.

(7) Hu, C.; Huang, D.; Zeng, G.; Cheng, M.; Gong, X.; Wang, R.; Xue, W.; Hu, Z.; Liu, Y. The Combination of Fenton Process and Phanerochaete Chrysosporium for the Removal of Bisphenol A in River Sediments: Mechanism Related to Extracellular Enzyme, Organic Acid and Iron. *Chem. Eng. J.* **2018**, *338*, 432−439.

(8) Huang, D.; Guo, X.; Peng, Z.; Zeng, G.; Xu, P.; Gong, X.; Deng, R.; Xue, W.; Wang, R.; Yi, H.; Liu, C. White rot fungi and Advanced Combined Biotechnology with Nanomaterials: Promising Tools for Endocrine-Disrupting Compounds Biotransformation. *Crit. Rev. Biotechnol.* **2018**, *38*, 671−689.

(9) Gong, X.; Huang, D.; Liu, Y.; Zeng, G.; Wang, R.; Wan, J.; Zhang, C.; Cheng, M.; Qin, X.; Xue, W. Stabilized Nanoscale Zerovalent Iron Mediated Cadmium Accumulation and Oxidative Damage of Boehmerianivea (L.) Gaudich Cultivated in Cadmium Contaminated Sediments. *Environ. Sci. Technol.* **2017**, *51*, 11308−11316.

(10) Gong, X.; Huang, D.; Liu, Y.; Zeng, G.; Wang, R.; Wei, J.; Huang, C.; Xu, P.; Wan, J.; Zhang, C. Pyrolysis and Reutilization of Plant Residues after Phytoremediation of Heavy Metals Contaminated Sediments: For Heavy Metals Stabilization and Dye Adsorption. *Bioresour. Technol.* **2018**, *253*, 64−71.

(11) Lenzi, G.G.; Evangelista, R.F.; Duarte, E.R.; Colpini, L.M.S.; Fornari, A.C.; Menechini Neto, R.; Jorge, L.M.M.; Santos, O.A.A. Photocatalytic Degradation of Textile Reactive Dye Using Artificial Neural Network Modeling Aapproach. *Desalin. Water Treat.* **2016**, *57*, 14132−14144.

(12) Cao, J.; Sun, S.; Li, X.; Yang, Z.; Xiong, W.; Wu, Y.; Jia, M.; Zhou, Y.; Zhou, C.; Zhang, Y. Efficient Charge Transfer in Aluminum-Cobalt Layered Double Hydroxide Derived from Co-ZIF for Enhanced Catalytic Degradation of Tetracycline through Peroxymonosulfate Activation. *Chem. Eng. J.* **2020**, *382*, 122802.

(13) Liu, J.; Liu, Y.; Liu, N.; Han, Y.; Zhang, X.; Huang, H.; Lifshitz, Y.; Lee, S.-T.; Zhong, J.; Kang, Z. Metal-Free Efficient Photocatalyst for Stable Visible Water Splitting via a Two-Electron Pathway. *Science* **2015**, *347*, 970−974.

(14) Hoffmann, M. R.; Martin, S. T.; Choi, W.; Bahnemann, D. W. Environmental Applications of Semiconductor Photocatalysis. *Chem. Rev.* **1995**, *95*, 69−96.

(15) Wang, Y.; Huang, Y.; Ho, W.; Zhang, L.; Zou, Z.; Lee, S. Biomolecule-Controlled Hydrothermal Synthesis of C-N-S Tri-Doped TiO_2 Nanocrystalline Photocatalysts for NO Removal Under Simulated Solar Light Irradiation. *J. Hazard. Mater.* **2009**, *169*, 77−87.

(16) Huang, D.; Chen, S.; Zeng, G.; Gong, X.; Zhou, C.; Cheng, M.; Xue, W.; Yan, X.; Li, J. Artificial Z-scheme Photocatalytic System: What have been Done and Where to Go? *Coord. Chem. Rev.* **2019**, *385*, 44−80.

(17) Fujishima, A.; Honda, K. Electrochemical Photolysis of Water at a Semiconductor Electrode. *Nature* **1972**, *238*, 37−38.

(18) Frank, S. N.; Bard, A. J. Heterogeneous Photocatalytic Oxidation of Cyanide Ion in Aqueous Solutions at Titanium Dioxide Powder. *J. Am. Chem. Soc.* **1977**, *99*, 303−304.

(19) Huang, D.; Li, Z.; Zeng, G.; Zhou, C.; Xue, W.; Gong, X.; Yan, X.; Chen, S.; Wang, W.; Cheng, M. Megamerger in Photocatalytic Field: 2D g-C_3N_4 Nanosheets Serve as Support of 0D Nanomaterials for Improving Photocatalytic Performance. *Appl. Catal., B* **2019**, *240*, 153−173.

(20) Chen, S.; Huang, D.; Zeng, G.; Gong, X.; Xue, W.; Li, J.; Yang, Y.; Zhou, C.; Li, Z.; Yan, X.; Li, T.; Zhang, Q. Modifying delafossite silver ferrite with polyaniline: visible-light-response Z-scheme heterojunction with charge transfer driven by internal electric field. *Chem. Eng. J.* **2019**, *370*, 1087−1100.

(21) Hu, Y. A Highly Efficient Photocatalyst–Hydrogenated Black TiO_2 for the Photocatalytic Splitting of Water. *Angew. Chem., Int. Ed.* **2012**, *51*, 12410−12412.

(22) Huang, D.; Yan, X.; Yan, M.; Zeng, G.; Zhou, C.; Wan, J.; Cheng, M.; Xue, W. Graphitic Carbon Nitride-Based Heterojunction Photoactive Nanocomposites: Applications and Mechanism Insight. *ACS Appl. Mater. Interfaces* **2018**, *10*, 21035−21055.

(23) Kim, D.; Sakimoto, K. K.; Hong, D.; Yang, P. Artificial Photosynthesis for Sustainable Fuel and Chemical Production. *Angew. Chem., Int. Ed.* **2015**, *54*, 3259−3266.

(24) Zhao, Y.; Jia, X.; Waterhouse, G. I.N.; Wu, L.-Z.; Tung, C.-H.; O'Hare, D.; Zhang, T. Layered Double Hydroxide Nanostructured Photocatalysts for Renewable Energy Production. *Adv. Energy. Mater.* **2016**, *6*, 1501974.

(25) Hu, Z.; Yuan, L.; Liu, Z.; Shen, Z.; Yu, J. An Elemental Phosphorus Photocatalyst with a Record High Hydrogen Evolution Efficiency. *Angew. Chem., Int. Ed.* **2016**, *55*, 9793−9793.

(26) Xiao, B.; Lin, L.; Hong, J.; Lin, H.; Song, Y. Synthesis of a Monoclinic $BiVO_4$ Nanorod Array as the Photocatalyst for Efficient Photoelectrochemical Water Oxidation. *RSC Adv.* **2017**, *7*, 7547−7554.

(27) Li, H.; Sun, Y.; Cai, B.; Gan, S.; Han, D.; Niu, L.; Wu, T. Hierarchically Z-scheme Photocatalyst of Ag@AgCl Decorated on $BiVO_4$(040) with Enhancing Photoelectrochemical and Photocatalytic Performance. *Appl. Catal., B* **2015**, *170-171*, 206.

(28) Lu, N.; Su, Y.; Li, J.; Yu, H.; Quan, X. Fabrication of Quantum-Sized CdS-Coated TiO_2 Nanotube Array with Efficient Photoelectrochemical Performance Using Modified Successive Ionic Layer Absorption and Reaction (SILAR) Method. *Sci. Bull.* **2015**, *60*, 1281−1286.

(29) Kudo, A.; Omori, K.; Kato, H. A Novel Aqueous Process for Preparation of Crystal Form-Controlled and Highly Crystalline $BiVO_4$ Powder from Layered Vanadates at Room Temperature and Its Photocatalytic and Photophysical Properties. *J. Am. Chem. Soc.* **1999**, *121*, 11459−11467.

(30) Meng, X.; Zhang, Z. Bismuth-Based Photocatalytic Semiconductors: Introduction, Challenges and Possible Approaches. *J. Mol. Catal. A: Chem.* **2016**, *423*, 533−549.

(31) Liu, G.; Yu, J. C.; Lu, G. Q.; Cheng, H. M. Crystal Facet Engineering of Semiconductor Photocatalysts: Motivations, Advancesand Unique Properties. *Chem. Commun.* **2011**, *47*, 6763−6783.

(32) Samsudin, M.; Sufian, S.; Hameed, B. Epigrammatic Progress and Perspective on the PhotocatalyticProperties of $BiVO_4$-Based Photocatalyst in Photocatalytic Water Treatment Technology: A review. *J. Mol. Liq.* **2018**, *268*, 438−459.

DOI: 10.1021/acscatal.9b03411
ACS Catal. 2020, 10, 1024−1059

(33) Liang, Y.; Tsubota, T.; Mooij, L. P.; van de Krol, R. Highly Improved Quantum Efficiencies for Thin Film $BiVO_4$ Photoanodes. *J. Phys. Chem. C* **2011**, *115*, 17594−17598.
(34) Abdi, F. F.; van de Krol, R. Nature and Light Dependence of Bulk Recombination in Co-Pi-Catalyzed $BiVO_4$ Photoanodes. *J. Phys. Chem. C* **2012**, *116*, 9398−9404.
(35) Abdi, F. F.; Savenije, T. J.; May, M. M.; Dam, B.; van de Krol, R. The Origin of Slow Carrier Transport in $BiVO_4$ Thin Film Photoanodes: A Time-Resolved Microwave Conductivity Study. *J. Phys. Chem. Lett.* **2013**, *4*, 2752−2757.
(36) Berglund, S. P.; Flaherty, D. W.; Hahn, N. T.; Bard, A. J.; Mullins, C. B. Photoelectrochemical Oxidation of Water using Nanostructured $BiVO_4$ Films. *J. Phys. Chem. C* **2011**, *115*, 3794−3802.
(37) Yu, J.; Kudo, A. Effects of Structural Variation on the Photocatalytic Performance of Hydrothermally Synthesized $BiVO_4$. *Adv. Funct. Mater.* **2006**, *16*, 2163−2169.
(38) Park, H. S.; Kweon, K. E.; Ye, H.; Paek, E.; Hwang, G. S.; Bard, A. J. Factors in the Metal Doping of $BiVO_4$ for Improved Photoelectrocatalytic Activity as Studied by Scanning Electrochemical Microscopy and First-Principles Density-Functional Calculation. *J. Phys. Chem. C* **2011**, *115*, 17870−17879.
(39) Lv, C.; Chen, G.; Sun, J.; Zhou, Y.; Fan, S.; Zhang, C. Realizing Nanosized Interfacial Contact via Constructing $BiVO_4/Bi_4V_2O_{11}$ Element-Copied Heterojunction Nanofibres for Superior Photocatalytic Properties. *Appl. Catal., B* **2015**, *179*, 54−60.
(40) Wetchakun, N.; Chaiwichain, S.; Inceesungvorn, B.; Pingmuang, K.; Phanichphant, S.; Minett, A. I.; Chen, J. $BiVO_4/CeO_2$ Nanocomposites with High Visible-Light-Induced Photocatalytic Activity. *ACS Appl. Mater. Interfaces* **2012**, *4*, 3718−3723.
(41) Cao, S.; Yin, Z.; Barber, J.; Boey, F.; Loo, S.; Xue, C. Preparation of Au-$BiVO_4$ Heterogeneous Nanostructures as Highly Efficient Visible-Light Photocatalysts. *ACS Appl. Mater. Interfaces* **2012**, *4*, 418−423.
(42) Zhang, K.; Liu, Y.; Deng, J.; Xie, S.; Zhao, X.; Yang, J.; Han, Z.; Dai, H. Co-Pd/$BiVO_4$: High-Performance Photocatalysts for the Degradation of Phenol under Visible Light Irradiation. *Appl. Catal., B* **2018**, *224*, 350−359.
(43) Shi, C.; Dong, X.; Wang, X.; Ma, H.; Zhang, X. Ag Nanoparticles Deposited on Oxygen-Vacancy-Containing $BiVO_4$ for Enhanced Near-Infrared Photocatalytic Activity. *Chin. J. Catal.* **2018**, *39*, 128−137.
(44) Jo, W. J.; Jang, J.-W.; Kong, K.-j.; Kang, H. J.; Kim, J. Y.; Jun, H.; Parmar, K. P. S.; Lee, J. S. Phosphate Doping into Monoclinic $BiVO_4$ for EnhancedPhotoelectrochemical Water Oxidation Activity. *Angew. Chem.* **2012**, *124*, 3201−3205.
(45) Malathi, A.; Madhavan, J.; Ashokkumar, M.; Arunachalam, P. A Review on $BiVO_4$ Photocatalyst: Activity Enhancement Methods for Solar Photocatalytic Applications. *Appl. Catal., A* **2018**, *555*, 47−74.
(46) Tan, H.; Amal, R.; Ng, Y. Alternative Strategies in Improving the Photocatalytic and Photoelectrochemical Activities of Visible Light-Driven $BiVO_4$: a Review. *J. Mater. Chem. A* **2017**, *5*, 16498−16521.
(47) Martin, D. J.; Liu, G.; Moniz, S. J. A.; Bi, Y.; Beale, A. M.; Ye, J.; Tang, J. Efficient Visible Driven Photocatalyst, Silver Phosphate: Performance, Understanding and Perspective. *Chem. Soc. Rev.* **2015**, *44*, 7808−7828.
(48) Martin, D.; Umezawa, N.; Chen, X.; Ye, J.; Tang, J. Facet Engineered Ag_3PO_4 for Efficient Water Photooxidation. *Energy Environ. Sci.* **2013**, *6*, 3380−3386.
(49) Hong, S.; Lee, S.; Jang, J.; Lee, J. Heterojunction $BiVO_4/WO_3$ Electrodes for Enhanced Photoactivity of Water Oxidation. *Energy Environ. Sci.* **2011**, *4*, 1781−1787.
(50) Zhao, Z.; Li, Z.; Zou, Z. Electronic Structure and Optical Properties of Monoclinic Clinobisvanite $BiVO_4$. *Phys. Chem. Chem. Phys.* **2011**, *13*, 4746−4753.
(51) Bierlein, J. D.; Sleight, A. W. Ferroelasticity in $BiVO_4$. *Solid State Commun.* **1975**, *16*, 69−70.
(52) Bhattacharya, A. K.; Mallick, K. K.; Hartridge, A. Phase Transition in $BiVO_4$. *Mater. Lett.* **1997**, *30*, 7−13.
(53) Tokunaga, S.; Kato, H.; Kudo, A. Selective Preparation of Monoclinic and Tetragonal $BiVO_4$ with Scheelite Structure and Their Photocatalytic Properties. *Chem. Mater.* **2001**, *13*, 4624−4628.
(54) Zhao, Z.; Luo, W.; Li, Z.; Zou, Z. Density Functional Theory Study of Doping Effects in Monoclinic Clinobisvanite $BiVO_4$. *Phys. Lett. A* **2010**, *374*, 4919−4927.
(55) Park, Y.; Mcdonald, K.; Choi, K. Progress in Bismuth Vanadate Photoanodes for Use in Solar Water Oxidation. *Chem. Soc. Rev.* **2013**, *42*, 2321−2337.
(56) Zhang, L.; Chen, D.; Jiao, X. Monoclinic Structured $BiVO_4$ Nanosheets: Hydrothermal Preparation, Formation Mechanism, and Coloristic and Photocatalytic Properties. *J. Phys. Chem. B* **2006**, *110*, 2668−2673.
(57) Walsh, A.; Yan, Y.; Huda, M.; Al-Jassim, M.; Wei, S. Band Edge Electronic Structure of $BiVO_4$: Elucidating the Role of the Bi s and V d Orbitals. *Chem. Mater.* **2009**, *21*, 547−551.
(58) Payne, D.; Robinson, M.; Egdell, R.; Walsh, A.; McNulty, J.; Smith, K.; Piper, L. The Nature of Electron Lone Pairs in $BiVO_4$. *Appl. Phys. Lett.* **2011**, *98*, 212110−212113.
(59) Cooper, J. K.; Gul, S.; Toma, F. M.; Chen, L.; Glans, P.-A.; Guo, J.; Ager, J. W.; Yano, J.; Sharp, I. D. Electronic Structure of Monoclinic $BiVO_4$. *Chem. Mater.* **2014**, *26*, 5365−5373.
(60) Yang, J.; Wang, D.; Han, H.; Li, C. Roles of Cocatalysts in Photocatalysis and Photoelectrocatalysis. *Acc. Chem. Res.* **2013**, *46*, 1900−1909.
(61) Hua, Q.; Cao, T.; Gu, X. K.; Lu, J.; Jiang, Z.; Pan, X.; Luo, L.; Li, W. X.; Huang, W. Crystal-Plane-Controlled Selectivity of Cu_2O Catalysts in Propylene Oxidation with Molecular Oxygen. *Angew. Chem., Int. Ed.* **2014**, *53*, 4856−4861.
(62) Yao, K. X.; Yin, X. M.; Wang, T. H.; Zeng, H. C. Synthesis, Self-Assembly, Disassembly, and Reassembly of Two Types of Cu_2O Nanocrystals Unifaceted with {001} or {110} Planes. *J. Am. Chem. Soc.* **2010**, *132*, 6131−6144.
(63) Xiong, Z.; Zhao, X. Nitrogen-Doped Titanate-Anatase Core-ShellNanobelts with Exposed {101} Anatase Facets and Enhanced Visible LightPhotocatalytic Activity. *J. Am. Chem. Soc.* **2012**, *134*, 5754−5757.
(64) Jiang, J.; Zhao, K.; Xiao, X.; Zhang, L. Synthesis and Facet-DependentPhotoreactivity of BiOCl Single Crystalline Nanosheets. *J. Am. Chem. Soc.* **2012**, *134*, 4473−4476.
(65) Li, R.; Zhang, F.; Wang, D.; Yang, J.; Li, M.; Zhu, J.; Zhou, X.; Han, H.; Li, C. Spatial Separation of Photogenerated Electrons and Holes among {010} and {110} Crystal Facets of $BiVO_4$. *Nat. Commun.* **2013**, *4*, 1432.
(66) Liu, T.; Zhou, X.; Dupuis, M.; Li, C. The Nature of Photogenerated Charge Separation among Different Crystal Facets of $BiVO_4$ Studied by Density Functional Theory. *Phys. Chem. Chem. Phys.* **2015**, *17*, 23503−23510.
(67) Yang, J.; Wang, D.; Zhou, X.; Li, C. A Theoretical Study on the Mechanism of Photocatalytic Oxygen Evolution on $BiVO_4$ in Aqueous Solution. *Chem. - Eur. J.* **2013**, *19*, 1320−1326.
(68) Wang, D.; Jiang, H.; Zong, X.; Xu, Q.; Ma, Y.; Li, G.; Li, C. Crystal Facet Dependence of Water Oxidation on $BiVO_4$ Sheets under Visible Light Irradiation. *Chem. - Eur. J.* **2011**, *17*, 1275−1282.
(69) Yang, H. G.; Sun, C. H.; Qiao, S. Z.; Zou, J.; Liu, G.; Smith, S. C.; Cheng, H. M.; Lu, G. Q. Anatase TiO_2 Single Crystals with a Large Percentage of Reactive Facets. *Nature* **2008**, *453*, 638−641.
(70) Chen, L.; Wang, J.; Meng, D.; Wu, X.; Wang, Y.; Zhong, E. The pH-Controlled {040} Facets Orientation of $BiVO_4$ Photocatalysts with Different Morphologies for Enhanced Visible Light Photocatalytic Performance. *Mater. Lett.* **2016**, *162*, 150−153.
(71) Wu, B.; Zheng, N. Surface and Interface Control of Noble Metal Nanocrystals for Catalytic and Electrocatalytic Applications. *Nano Today* **2013**, *8*, 168−197.
(72) Liu, W.; Zhao, G.; An, M.; Chang, L. Solvothermal Synthesis of Nanostructured $BiVO_4$ with Highly Exposed {010} Facets and

DOI: 10.1021/acscatal.9b03411
ACS Catal. 2020, 10, 1024−1059

Enhanced Sunlight-Driven Photocatalytic Properties. *Appl. Surf. Sci.* **2015**, *357*, 1053−1063.
(73) Meng, X.; Zhang, L.; Dai, H.; Zhao, Z.; Zhang, R.; Liu, Y. Surfactant-Assisted Hydrothermal Fabrication and Visible-Light-Driven Photocatalytic Degradation of Methylene Blue over Multiple Morphological $BiVO_4$ Single-Crystallites. *Mater. Chem. Phys.* **2011**, *125*, 59−65.
(74) Chen, M.; Wu, B.; Yang, J.; Zheng, N. Small Adsorbate-Assisted Shape Control of Pd and Pt Nanocrystals. *Adv. Mater.* **2012**, *24*, 862−879.
(75) Xie, S.; Shen, Z.; Zhang, H.; Cheng, J.; Zhang, Q.; Wang, Y. Photocatalytic Coupling of Formaldehyde to Ethylene Glycol and Glycoaldehyde over Bismuth Vanadate with Controllable Facets and Cocatalysts. *Catal. Sci. Technol.* **2017**, *7*, 923−933.
(76) Thalluri, S.; Hussain, M.; Saracco, G.; Barber, J.; Russo, N. Green-Synthesized $BiVO_4$Oriented along {040} Facets for Visible-Light-Driven Ethylene Degradation. *Ind. Eng. Chem. Res.* **2014**, *53*, 2640−2646.
(77) Zhang, J.; Du, J.; Han, B.; Liu, Z.; Jiang, T.; Zhang, Z. Sonochemical Formation of Single-Crystalline Gold Nanobelts. *Angew. Chem., Int. Ed.* **2006**, *45*, 1116−1119.
(78) Wang, Z.; Li, W.; Kong, D.; Du, Y.; Yan, T.; Kong, D.; You, J. Amino Acid-Assisted Hydrothermal Synthesis of $BiVO_4$ with Highly Exposed {040} Facets and Enhanced Visible-Light-Driven Photocatalytic Properties. *J. Nanosci. Nanotechnol.* **2017**, *17*, 5391−5399.
(79) Dong, S.; Feng, J.; Li, Y.; Hu, L.; Liu, M.; Wang, Y.; Pi, Y.; Sun, J.; Sun, J. Shape-controlled synthesis of $BiVO_4$ hierarchical structures withunique natural-sunlight-driven photocatalytic. *Appl. Catal., B* **2014**, *152*−*153*, 413−424.
(80) Xi, G.; Ye, J. Synthesis of Bismuth Vanadate Nanoplates with Exposed {001} Facets and Enhanced Visible-Light Photocatalytic Properties. *Chem. Commun.* **2010**, *46*, 1893−1895.
(81) Zhao, Y.; Li, R.; Mu, L.; Li, C. Significance of Crystal Morphology Controlling in Semiconductor-Based Photocatalysis: A Case Study on $BiVO_4$ Photocatalyst. *Cryst. Growth Des.* **2017**, *17*, 2923−2928.
(82) Tan, H. L.; Tahini, H. A.; Wen, X.; Wong, R. J.; Tan, X.; Iwase, A.; Kudo, A.; Amal, R.; Smith, S. C.; Ng, Y. H. Interfacing $BiVO_4$ with Reduced Graphene Oxide for Enhanced Photoactivity: a Tale of Facet Dependence of Electron Shuttling. *Small* **2016**, *12*, 5295−5302.
(83) Zhao, Z.; Li, Z.; Zou, Z. Structure and Energetics of Low-Index Stoichiometric Monoclinic ClinobisvaniteBiVO$_4$ Surfaces. *RSC Adv.* **2011**, *1*, 874−883.
(84) Li, G. First-Principles Investigation of the SurfaceProperties of Fergusonite-Type Monoclinic $BiVO_4$Photocatalyst. *RSC Adv.* **2017**, *7*, 9130−9140.
(85) Li, R.; Han, H.; Zhang, F.; Wang, D.; Li, C. Highly Efficient Photocatalysts Constructed by Rational Assembly of Dual-Cocatalysts Separately on Different Facets of $BiVO_4$. *Energy Environ. Sci.* **2014**, *7*, 1369−1376.
(86) Wang, Y.; He, J.; Liu, C.; Chong, W. H.; Chen, H. Thermodynamics versus Kinetics in Nanosynthesis. *Angew. Chem., Int. Ed.* **2015**, *54*, 2022−2051.
(87) Yamada, Y.; Tsung, C. K.; Huang, W.; Huo, Z.; Habas, S. E.; Soejima, T.; Aliaga, C. E.; Somorjai, G. A.; Yang, P. Nanocrystal Bilayer for Tandem Catalysis. *Nat. Chem.* **2011**, *3*, 372−376.
(88) Yan, Y.; Ni, T.; Du, J.; Li, L.; Fu, S.; Li, K.; Zhou, J. Green Synthesis of Balsam Pear-Shaped $BiVO_4$/$BiPO_4$ Nanocomposite for Degradation of Organic Dye and Antibiotic Metronidazole. *Dalton Trans.* **2018**, *47*, 6089−6101.
(89) Wang, T.; Li, C.; Ji, J.; Wei, Y.; Zhang, P.; Wang, S.; Fan, X.; Gong, J. Reduced Graphene Oxide (rGO)/$BiVO_4$ Composites with Maximized Interfacial Coupling for Visible Light Photocatalysis. *ACS Sustainable Chem. Eng.* **2014**, *2*, 2253−2258.
(90) Zhou, C.; Wang, S.; Zhao, Z.; Shi, Z.; Yan, S.; Zou, Z. A facet-Dependent Schottky-junction Electron Shuttlein a $BiVO_4${010}-Au-Cu_2O Z-Scheme Photocatalystfor Efficient Charge Separation. *Adv. Funct. Mater.* **2018**, *28*, 1801214.
(91) Li, C.; Zhang, P.; Lv, R.; Lu, J.; Wang, T.; Wang, S.; Wang, H.; Gong, J. Selective Deposition of Ag_3PO_4 on Monoclinic $BiVO_4$(040) for Highly Efficient Photocatalysis. *Small* **2013**, *9*, 3951−3956.
(92) Li, H.; Yu, H.; Quan, X.; Chen, S.; Zhao, H. Improved Photocatalytic Performance of Heterojunctionby Controlling the Contact Facet: High Electron TransferCapacity between TiO_2 and the {110} Facet of $BiVO_4$Caused by Suitable Energy Band Alignment. *Adv. Funct. Mater.* **2015**, *25*, 3074−3080.
(93) Chen, F.; Wu, C.; Wang, J.; Francois-Xavier, C. P.; Wintgens, T. Highly Efficient Z-scheme Structured Visible-Light Photocatalyst Constructedby Selective Doping of Ag@AgBr and Co_3O_4 Separately on {010} and {110}Facets of $BiVO_4$: Pre-separation Channel and Hole-sink Effects. *Appl. Catal., B* **2019**, *250*, 31−41.
(94) Zhang, Y.; Gong, H.; Zhang, Y.; Liu, K.; Cao, H.; Yan, H.; Zhu, J. The Controllable Synthesis of Octadecahedral $BiVO_4$ with Exposed {111} Facets. *Eur. J. Inorg. Chem.* **2017**, *2017*, 2990−2997.
(95) Wang, Y.; Tan, G.; Ren, H.; Xia, A.; Li, B.; Zhang, D.; Wang, M.; Lv, L. Synthesis of $BiVO_4$ with Surface Heterojunction for Enhancing Photocatalytic Activity by Low Temperature Aqueous Method. *Mater. Lett.* **2018**, *229*, 308−311.
(96) Zhao, G.; Liu, W.; Hao, Y.; Zhang, Z.; Li, Q.; Zang, S. Nanostructured Shuriken-Like $BiVO_4$ with Preferentially Exposed {010} Facets: Preparation, Formation Mechanism, and Enhanced Photocatalytic Performance. *Dalton Trans.* **2018**, *47*, 1325−1336.
(97) Ravidhas, C.; Arivukarasan, D.; Venkatesh, R.; Suresh, E. S. M.; Anitha, B.; Josephine, A. J.; Ezhil Raj, A. A. M.; Ravichandran, K. S.; Gopalakrishnan, C.; Sanjeeviraja, C. Substrate Temperature Induced (020) Growth Facets of Nebulizer Sprayed $BiVO_4$ Thin Films for Effective Photodegradation of Rhodamine B. *Cryst. Res. Technol.* **2019**, *54*, 1700257.
(98) Li, P.; Chen, X.; He, H.; Zhou, X.; Zhou, Y.; Zou, Z. Polyhedral 30□faceted $BiVO_4$ Microcrystals Predominantly Enclosed by High□index Planes Promoting Photocatalytic Water□Splitting Activity. *Adv. Mater.* **2018**, *30*, 1703119.
(99) Hu, J. Q.; He, H. C.; Li, L.; Zhou, X.; Li, Z. S.; Shen, Q.; Wu, C. P.; Asiri, A. M.; Zhou, Y.; Zou, Z. G. Highly Symmetrical, 24-Faceted, Concave $BiVO_4$ Polyhedron Bounded by Multiple High-index Facets for Prominent Photocatalytic O_2 Evolution under Visible Light. *Chem. Commun.* **2019**, *55*, 4777−4780.
(100) Zhai, X. T.; Li, Z. Y.; Lu, Z. C.; Wang, G. L.; Li, P.; Gao, Y. Q.; Huang, X.; Huang, W.; Uji-i, H.; Lu, G. Synthesis of 42-Faceted Bismuth Vanadate Microcrystals for Enhanced Photocatalytic Activity. *J. Colloid Interface Sci.* **2019**, *542*, 207−212.
(101) Kim, C.; Son, Y.; Kang, M.; Kim, D.; Kang, Y. {040}-Crystal Facet Engineering of $BiVO_4$ Plate Photoanodes for Solar Fuel Production. *Adv. Energy Mater.* **2016**, *6*, 1501754.
(102) Bi, Y.; Ouyang, S.; Umezawa, N.; Cao, J.; Ye, J. Facet Effect of Single-Crystalline Ag_3PO_4 Sub-Microcrystals on Photocatalytic Properties. *J. Am. Chem. Soc.* **2011**, *133*, 6490−6492.
(103) Liu, B.; Ma, L.; Ning, L. C.; Zhang, C. J.; Han, G. P.; Pei, C. J.; Zhao, H.; Liu, S. Z.; Yang, H. Q. Charge Separation between Polar {111} Surfaces of CoO Octahedrons and Their Enhanced Visible-Light Photocatalytic Activity. *ACS Appl. Mater. Interfaces* **2015**, *7*, 6109−6117.
(104) Zhu, W.; Shen, M.; Fan, G.; Yang, A.; Meyer, J. R.; Ou, Y.; Yin, B.; Fortner, J.; Foston, M.; Li, Z.; Zou, Z.; Sadtler, B. Facet-Dependent Enhancement in the Activity of Bismuth Vanadate Microcrystals for the Photocatalytic Conversion of Methane to Methanol. *ACS Appl. Nano Mater.* **2018**, *1*, 6683−6691.
(105) Fang, W.; Jiang, Z.; Yu, L.; Liu, H.; Shangguan, W.; Terashima, C.; Fujishima, A. Novel Dodecahedron $BiVO_4$:YVO_4 Solid Solution with Enhanced Charge Separation on Adjacent Exposed Facets for Highly Efficient Overall Water Splitting. *J. Catal.* **2017**, *352*, 155−159.
(106) Xu, J.; Bian, Z.; Xin, X.; Chen, A.; Wang, H. Size Dependence of Nanosheet $BiVO_4$ with Oxygen Vacancies and Exposed {001}-Facets on the Photodegradation of Oxytetracycline. *Chem. Eng. J.* **2018**, *337*, 684−696.

DOI: 10.1021/acscatal.9b03411
ACS Catal. 2020, 10, 1024−1059

(107) Lu, G.; Wang, F.; Zou, X. Hydrothermal Synthesis of m-$BiVO_4$ and m-$BiVO_4$/BiOBr with VariousFacets and Morphologies and their Photocatalytic Performance underVisible Light. *J. Alloys Compd.* **2016**, *25*, 1−10.
(108) Zeng, J.; Zhong, J.; Li, J.; Xiang, Z.; Liu, X.; Chen, J. Improvement of Photocatalytic Activityunder Solar Light of $BiVO_4$ Microcrystals Synthesized by Surfactant-Assisted HydrothermalMethod. *Mater. Sci. Semicond. Process.* **2014**, *27*, 41−46.
(109) Zhu, M.; Sun, Z.; Fujitsuka, M.; Majima, T. Z-Scheme Photocatalytic Water Splitting ona 2D Heterostructure of Black Phosphorus/Bismuth Vanadate using Visible Light. *Angew. Chem., Int. Ed.* **2018**, *57*, 2160−2164.
(110) Dong, C.; Lu, S.; Yao, S.; Ge, R.; Wang, Z.; Wang, Z.; An, P.; Liu, Y.; Yang, B.; Zhang, H. Colloidal Synthesis of Ultrathin Monoclinic $BiVO_4$ Nanosheets for Z-scheme Overall Water Splitting under Visible Light. *ACS Catal.* **2018**, *8*, 8649−8648.
(111) Wilson, J.; Idriss, H. Structure Sensitivity and Photocatalytic Reactions of Semiconductors. Effect of the Last Layer Atomic Arrangement. *J. Am. Chem. Soc.* **2002**, *124*, 11284−11285.
(112) Li, P.; Zhou, Y.; Zhao, Z.; Xu, Q.; Wang, X.; Xiao, M.; Zou, Z. Hexahedron Prism-Anchored Octahedronal CeO_2: Crystal Facet-Based Homojunction Promoting Efficient Solar Fuel Synthesis. *J. Am. Chem. Soc.* **2015**, *137*, 9547−9550.
(113) Yuan, B.; Chong, R.; Zhang, B.; Li, J.; Liu, Y.; Li, C. Photocatalytic Aerobic Oxidation of Amines toImines on $BiVO_4$ under Visible Light Irradiation. *Chem. Commun.* **2014**, *50*, 15593−15596.
(114) Kang, H.; Kang, J.; Kim, J.; Lee, S. Annealing Effect on the Property of Ultraviolet and Green Emissions of ZnO Thin Films. *J. Appl. Phys.* **2004**, *95*, 1246−1250.
(115) Yu, J.; Wang, B. Effect of Calcination Temperature on Morphology and Photoelectrochemical Properties of Anodized Titanium Dioxide Nanotube Arrays. *Appl. Catal., B* **2010**, *94*, 295−302.
(116) Tan, H.; Suyanto, A.; Denko, A.; Saputera, W.; Amal, R.; Osterloh, F.; Ng, Y. Enhancing the Photoactivity of Faceted $BiVO_4$ via Annealing in Oxygen-Deficient Condition. *Part Syst. Char.* **2017**, *34*, 1600290−1600299.
(117) Tan, H.; Wen, X.; Amal, R.; Ng, Y. $BiVO_4$ {010} and {110} relative exposure extent: governing factor of surface charge population and photocatalytic activity. *J. Phys. Chem. Lett.* **2016**, *7*, 1400−1405.
(118) Shan, L.; Lu, C.; Dong, L.; Suriyaprakash, J. Efficient Facet Regulation of $BiVO_4$ and Its Photocatalytic Motivation. *J. Alloys Compd.* **2019**, *804*, 385−391.
(119) Yu, T.; Lv, L.; Wang, H.; Tan, X. Enhanced Photocatalytic Treatment of Cr(VI) and Phenol by Monoclinic $BiVO_4$ with {010}-Orientation Growth. *Mater. Res. Bull.* **2018**, *107*, 248−254.
(120) Rettie, A. J.; Lee, H. C.; Marshall, L. G.; Lin, J. F.; Capan, C.; Lindemuth, J.; McCloy, J. S.; Zhou, J.; Bard, A. J.; Mullins, C. B. Combined Charge Carrier Transport and Photoelectrochemical Characterization of $BiVO_4$ Single Crystals: Intrinsic Behavior of a Complex Metal Oxide. *J. Am. Chem. Soc.* **2013**, *135*, 11389−11396.
(121) Chang, S.; Liu, W. The Roles of Surface-Doped Metal Ions (V, Mn, Fe, Cu, Ce, and W) in the Interfacial Behavior of TiO_2 Photocatalysts. *Appl. Catal., B* **2014**, *156−157*, 466−475.
(122) Wang, M.; Niu, C.; Liu, Q.; Che, Y.; Liu, J. Enhanced Photodegradation Methyl Orange by N-F Co-doped $BiVO_4$ Synthesized by Sol-gel Method. *Mater. Sci. Semicond. Process.* **2014**, *25*, 271−278.
(123) Zhao, D.; Zong, W.; Fan, Z.; Fang, Y.-W.; Xiong, S.; Du, M.; Wu, T.; Ji, F.; Xu, X. Synthesis of Carbon-doped Nanosheets m-$BiVO_4$ with Three-dimensional (3D) Hierarchical Structure by One-step Hydrothermal Method and Evaluation of their High Visible-Light Photocatalytic Property. *J. Nanopart. Res.* **2017**, *19*, 124−132.
(124) Niu, M.; Zhu, R.; Tian, F.; Song, K.; Cao, G.; Ouyang, F. The Effects of Precursors and Loading of Carbon on the Photocatalytic Activity of C-$BiVO_4$ for the Degradation of High Concentrations of Phenol under Visible Light Irradiation. *Catal. Today* **2015**, *258*, 585−594.
(125) Tang, J.; Song, B.; Deng, Q.; Xin, H. Facile Hydrothermal-carbonization Approach to Carbon-Modified $BiVO_4$ Composites with Enhanced Photocatalytic Activity. *Mater. Sci. Semicond. Process.* **2015**, *35*, 90−95.
(126) Wang, Y.; Huang, J.; Tan, G.; Huang, J.; Zhang, L. Controllable Synthesis and Photocatalytic Properties of C-doped $BiVO_4$ with Self-heterostructure under Different Light Sources. *Nano* **2015**, *10*, 1550008.
(127) Wang, M.; Zheng, H.; Liu, J.; Dong, D.; Che, Y.; Yang, C. Enhanced Visible-Light-Driven Photocatalytic Activity of B-doped $BiVO_4$ Synthesized using a Corn Stem Template. *Mater. Sci. Semicond. Process.* **2015**, *30*, 307−313.
(128) Shan, L.; Wang, G.; Suriyaprakash, J.; Li, D.; Liu, L.; Dong, L. Solar Light Driven Pure Water Splitting of B-doped $BiVO_4$ Synthesized via a Sol-gel Method. *J. Alloys Compd.* **2015**, *636*, 131−137.
(129) Li, Y.; Jing, T.; Liu, Y.; Huang, B.; Dai, Y.; Zhang, X.; Qin, X.; Whangbo, M.-H. Enhancing the Efficiency of Water Oxidation by Boron-doped $BiVO_4$ under Visible Light: Hole Trapping by BO_4 tetrahedra. *ChemPlusChem* **2015**, *80*, 1113−1118.
(130) Zhao, Z.; Dai, H.; Deng, J.; Liu, Y.; Au, C. Effect of Sulfur Doping on the Photocatalytic Performance of $BiVO_4$ under Visible Light Illumination. *Chin. J. Catal.* **2013**, *34*, 1617−1626.
(131) Zhao, Z.; Dai, H.; Deng, J.; Liu, Y.; Au, C. Enhanced Visible-Light Photocatalytic Activities of Porous Olive-shaped Sulfur-doped $BiVO_4$-Supported Cobalt Oxides. *Solid State Sci.* **2013**, *18*, 98−104.
(132) Li, J.; Guo, Z.; Liu, H.; Du, J.; Zhu, Z. Two-step hydrothermal process for synthesis of F-doped $BiVO_4$ spheres with enhanced photocatalytic activity. *J. Alloys Compd.* **2013**, *581*, 40−45.
(133) Jiang, H.; Dai, H.; Deng, J.; Liu, Y.; Zhang, L.; Ji, K. Porous F-doped $BiVO_4$: Synthesis and Enhanced Photocatalytic Performance for the Degradation of Phenol under Visible-Light Illumination. *Solid State Sci.* **2013**, *17*, 21−27.
(134) Tan, G.; Zhang, L.; Ren, H.; Huang, J.; Yang, W.; Xia, A. Microwave Hydrothermal Synthesis of N-doped $BiVO_4$ Nanoplates with Exposed {040} Facets and Enhanced Visible-Light Photocatalytic Properties. *Ceram. Int.* **2014**, *40*, 9541−9547.
(135) Zhao, X.; Hu, J.; Yao, X.; Chen, S.; Chen, Z. Clarifying the Roles of Oxygen Vacancy in W-doped $BiVO_4$ for Solar Water Splitting. *ACS Appl. Energy Mater.* **2018**, *1*, 3410−3419.
(136) Steier, L.; Herraiz-Cardona, I.; Gimenez, S.; Fabregat-Santiago, F.; Bisquert, J.; Tilley, S. D.; Gratzel, M. Understanding the Role of Underlayers and Overlayers in Thin Film Hematite Photoanodes. *Adv. Funct. Mater.* **2014**, *24*, 7681−7688.
(137) Yang, T.-Y.; Kang, H.-Y.; Sim, U.; Lee, Y.-J.; Lee, J.-H.; Koo, B.; Nam, K. T.; Joo, Y.-C. A New Hematite Photoanode Doping Strategy for Solar Water Splitting: Oxygen Vacancy Generation. *Phys. Chem. Chem. Phys.* **2013**, *15*, 2117−2124.
(138) Hu, J.; Zhao, X.; Chen, W.; Su, H.; Chen, Z. Theoretical Insight into the Mechanism of Photoelectrochemical Oxygen Evolution Reaction on $BiVO_4$ Anode with Oxygen Vacancy. *J. Phys. Chem. C* **2017**, *121*, 18702−18709.
(139) Yao, X.; Wang, D.; Zhao, X.; Ma, S.; Bassi, P. S.; Yang, G.; Chen, W.; Chen, Z.; Sritharan, T. Scale-up of $BiVO_4$ Photoanode for Water Splitting in a Photoelectrochemical Cell: Issues and Challenges. *Energy Technol.* **2018**, *6*, 100−109.
(140) Jiang, Z.; Liu, Y.; Jing, T.; Huang, B.; Zhang, X.; Qin, X.; Dai, Y.; Whangbo, M.-H. Enhancing the Photocatalytic Activity of $BiVO_4$ for Oxygen Evolution by Ce Doping: Ce^{3+} Ions as Hole Traps. *J. Phys. Chem. C* **2016**, *120*, 2058−2063.
(141) Wang, Z.; Huang, S.; Jian, Z.; Yin, J.; Fei, Z.; Zhang, Y. Hydrothermal Synthesis and Characterization of In^{3+} Modified $BiVO_4$ Nanoparticles with Enhanced Photocatalytic Activity. *Res. Chem. Intermed.* **2016**, *42*, 4147−4519.
(142) Luo, W.; Wang, J.; Zhao, X.; Zhao, Z.; Li, Z.; Zou, Z. Formation Energy and Photoelectrochemical Properties of $BiVO_4$ fter Doping at Bi^{3+} or V^{5+} Sites with Higher Valence Metal Ions. *Phys. Chem. Chem. Phys.* **2013**, *15*, 1006−1013.

DOI: 10.1021/acscatal.9b03411
ACS Catal. 2020, 10, 1024−1059

(143) Ullah, H.; Tahir, A.; Mallick, T. Structural and Electronic Properties of Oxygen Defective and Se-doped p-type $BiVO_4$(001) Thin Film for the Applications of Photocatalysis. *Appl. Catal., B* **2018**, *224*, 895−903.
(144) Zhang, Y.; Guo, Y.; Duan, H.; Li, H.; Sun, C.; Liu, H. Facile synthesis of V^{4+} self-doped, [010] orientedBiVO$_4$ nanorods with highly efficient visible light-induced photocatalytic activity. *Phys. Chem. Chem. Phys.* **2014**, *16*, 24519−24526.
(145) Zhong, D. K.; Choi, S.; Gamelin, D. R. Near-Complete Suppression of Surface Recombination in Solar Photoelectrolysis by "Co-Pi" Catalyst-Modified W: $BiVO_4$. *J. Am. Chem. Soc.* **2011**, *133*, 18370−18377.
(146) Abdi, F. F.; Firet, N.; van de Krol, R. Water□Splitting Catalysis and Solar Fuel Devices: Artificial Leaves on the Move. *ChemCatChem* **2013**, *5*, 490−496.
(147) Luo, W.; Yang, Z.; Li, Z.; Zhang, J.; Liu, J.; Zhao, Z.; Wang, Z.; Yan, S.; Yu, T.; Zou, Z. Solar Hydrogen Generation from Seawater with a Modified $BiVO_4$ Photoanode. *Energy Environ. Sci.* **2011**, *4*, 4046−4051.
(148) Beni, G.; Schiavone, L.; Shay, J.; Dautremont-Smith, W.; Schneider, B. Electrocatalytic Oxygen Evolution on Reactively Sputtered Electrochromic Iridium Oxide Films. *Nature* **1979**, *282*, 281−283.
(149) Harriman, A.; Pickering, I. J.; Thomas, J. M.; Christensen, P. A. Metal Oxides as Heterogeneous Catalysts for Oxygen Evolution under Photochemical Conditions. *J. Chem. Soc., Faraday Trans. 1* **1988**, *84*, 2795−2806.
(150) Chen, S.; Huang, D.; Zeng, G.; Xue, W.; Lei, L.; Xu, P.; Deng, R.; Li, J.; Cheng, M. In-Situ Synthesis of Facet-Dependent $BiVO_4$/Ag_3PO_4/PANI Photocatalyst with Enhanced Visible-light-induced Photocatalytic Degradation Performance: Synergism of Interfacial Coupling and Hole-Transfer. *Chem. Eng. J.* **2020**, *382*, 122840.
(151) Moniz, S. J. A.; Shevlin, S. A.; Martin, D. J.; Guo, Z. X.; Tang, J. W. Visible-Light Driven Heterojunction Photocatalysts for Water-Splitting - a Critical Review. *Energy Environ. Sci.* **2015**, *8*, 731−759.
(152) Qu, Y.; Duan, X. Progress, Challenge and Perspective of Heterogeneous Photocatalysts. *Chem. Soc. Rev.* **2013**, *42*, 2568−2580.
(153) Peerakiatkhajohn, P.; Yun, J. H.; Wang, S. C.; Wang, L. Z. Review of Recent Progress in Unassisted Photoelectrochemical Water Splitting: from Material Modification to Configuration Design. *J. Photonics Energy* **2017**, *7*, 012006.
(154) Wang, S.; He, T.; Yun, J.-H.; Hu, Y.; Xiao, M.; Du, A.; Wang, L. New Iron-Cobalt Oxide Catalysts Promoting $BiVO_4$ Films forPhotoelectrochemical Water Splitting. *Adv. Funct. Mater.* **2018**, *28*, 1802685.
(155) Bai, S.; Wang, L.; Li, Z.; Xiong, Y. Facet-Engineered Surfaceand Interface Design of Photocatalytic Materials. *Adv. Sci.* **2017**, *4*, 1600216.
(156) Jiang, R.; Li, B.; Fang, C.; Wang, J. Metal/Semiconductor Hybrid Nanostructures for Plasmon-Enhanced Applications. *Adv. Mater.* **2014**, *26*, 5274−5309.
(157) Rej, S.; Wang, H. J.; Huang, M. X.; Hsu, S. C.; Tan, C. S.; Lin, F. C.; Huang, J. S.; Huang, M. H. Facet-Dependent Optical Propertiesof Pd-Cu_2O Core-Shell Nanocubes and Octahedra. *Nanoscale* **2015**, *7*, 11135−11141.
(158) Ye, F.; Li, H.; Yu, H.; Chen, S.; Quan, X. Constructing $BiVO_4$-Au@CdS Photocatalyst with Energic Charge-Carrier-Separation Capacity Derived from Facet Induction and Z-scheme Bridge for Degradation of Organic Pollutants. *Appl. Catal., B* **2018**, *227*, 258−265.
(159) Wu, D.; Bao, S.; Wang, Z.; Zhang, Z.; Tian, B.; Zhang, J. Au-mediated Composite In_2S_3-Au-$BiVO_4$ with EnhancedPhotocatalytic Activity for Organic Pollutant Degradation. *Chem. Select.* **2018**, *3*, 4889−4896.
(160) Booshehri, A.; Chun-Kiat Goh, S.; Hong, J.; Jiang, R.; Xu, R. Effect of Depositing Silver Nanoparticles on $BiVO_4$ in Enhancing Visible Light Photocatalytic Inactivation of Bacteria in water. *J. Mater. Chem. A* **2014**, *2*, 6209−6217.
(161) Liu, T.; Zhang, X.; Zhao, F.; Wang, Y. Targeting Inside Charge Carriers Transfer of Photocatalyst: SelectiveDeposition of Ag_2O on $BiVO_4$ with Enhanced UV-vis-NIR PhotocatalyticOxidation Activity. *Appl. Catal., B* **2019**, *251*, 220−228.
(162) Zhu, J.; Fan, F.; Chen, R.; An, H.; Feng, Z.; Li, C. DirectImaging of Highly Anisotropic Photogenerated Charge Separationson Different Facets of a Single $BiVO_4$ Photocatalyst. *Angew. Chem., Int. Ed.* **2015**, *54*, 9111−9114.
(163) Zhu, J.; Pang, S.; Dittrich, T.; Gao, Y.; Nie, W.; Cui, J.; Chen, R.; An, H.; Fan, F.; Li, C. Visualizing the Nano Cocatalyst Aligned Electric Fields on Single Photocatalyst Particles. *Nano Lett.* **2017**, *17*, 6735−6741.
(164) Hu, J.; Chen, W.; Zhao, X.; Su, H.; Chen, Z. Anisotropic Electronic Characteristics, Adsorption, and Stability of Low-index $BiVO_4$ Surfaces for Photoelectrochemical Applications. *ACS Appl. Mater. Interfaces* **2018**, *10*, 5475−5484.
(165) Opoku, F.; Govender, K. K.; van Sittert, C. G. C. E.; Govender, P. P. Role of MoS_2 and WS_2 Monolayers on the Photocatalytic Hydrogen Production andPollutant Degradation of Monoclinic $BiVO_4$: a First-Principles Study. *New J. Chem.* **2017**, *41*, 11701−11713.
(166) Wang, Y.; Tan, G.; Liu, T.; Su, Y.; Ren, H.; Zhang, X.; Xia, A.; Lv, L.; Liu, Y. Photocatalytic Properties of the g-C_3N_4/{010} Facets $BiVO_4$ Interface Z-Scheme Photocatalysts Induced by $BiVO_4$ Surface Heterojunction. *Appl. Catal., B* **2018**, *234*, 37−49.
(167) Li, J.; Zhou, J.; Hao, H.; Li, W.; Liu, G. Exposed Specific {040} and {110} Facets of $BiVO_4$ Modified with Bi_2WO_6 Nanoparticles for Enhanced Photocatalytic Performance. *New J. Chem.* **2017**, *41*, 6922−6927.
(168) Shan, L.; Bi, J.; Lu, C.; Xiao, Y. $BiVO_4$(010)/rGONanocomposite and its PhotocatalysisApplication. *J. Inorg. Organomet. Polym. Mater.* **2018**, *1*, 1−10.
(169) Wei, T.; Zhu, Y.-N.; Gu, Z.; An, X.; Liu, L.-m.; Wu, Y.; Liu, H.; Tang, J.; Qu, J. Multi-electricField Modulation for Photocatalytic Oxygen Evolution: Enhanced Charge Separation by Coupling Oxygen Vacancies with Faceted Heterostructures. *Nano Energy* **2018**, *51*, 764−773.
(170) Stolarczyk, J. K.; Bhattacharyya, S.; Polavarapu, L.; Feldmann, J. Challenges and Prospects in Solar Water Splitting and CO_2 Reductionwith Inorganic and Hybrid Nanostructures. *ACS Catal.* **2018**, *8*, 3602−3635.
(171) Sun, S.; Hisatomi, T.; Wang, Q.; Chen, S.; Ma, G.; Liu, J.; Nandy, S.; Minegishi, T.; Katayama, M.; Domen, K. Efficient Redox-Mediator-Free Z□Scheme Water Splitting Employing Oxysulfide Photocatalysts under Visible Light. *ACS Catal.* **2018**, *8*, 1690−1696.
(172) Zeng, C.; Hu, Y.; Zhang, T.; Dong, F.; Zhang, Y.; Huang, H. Core-satellite Structured Z-scheme Catalyst $Cd_{0.5}Zn_{0.5}S$/$BiVO_4$ forHighly Efficiency and Stable Photocatalytic Water Splitting. *J. Mater. Chem. A* **2018**, *6*, 16932−16942.
(173) Ou, M.; Wan, S.; Zhong, Q.; Zhang, S.; Song, Y.; Guo, L.; Cai, W.; Xu, Y. Hierarchical Z-scheme Photocatalyst ofg-C_3N_4@Ag/$BiVO_4$ (040) with EnhancedVisible-Light-Induced Photocatalytic Oxidation Performance. *Appl. Catal., B* **2018**, *221*, 97−107.
(174) Thalluri, S. M.; Hernández, S.; Bensaid, S.; Saracco, G.; Russo, N. Green-Synthesized W- and Mo-doped $BiVO_4$ Oriented along the {040} Facet with Enhanced Activity for the Sun-Driven Water Oxidation. *Appl. Catal., B* **2016**, *180*, 630−636.
(175) Zheng, M.; Cao, X.; Ding, Y.; Tian, T.; Lin, J. Boosting Photocatalytic Water Oxidation Achieved by $BiVO_4$ Coupled with Iron-Containing Polyoxometalate: Analysis the True Catalyst. *J. Catal.* **2018**, *363*, 109−116.
(176) Li, X.; Yu, J.; Jaroniec, M.; Chen, X. Cocatalysts for Selective Photoreduction of CO_2 into Solar Fuels. *Chem. Rev.* **2019**, *119*, 3962−4179.
(177) Liu, Y. Y.; Huang, B. B.; Dai, Y.; Zhang, X. Y.; Qin, X. Y.; Jiang, M. H.; Whangbo, M. H. Selective Ethanol Formation from Photocatalytic Reduction of Carbon Dioxide in Water with BiVO4 Photocatalyst. *Catal. Commun.* **2009**, *11*, 210−213.

DOI: 10.1021/acscatal.9b03411
ACS Catal. 2020, 10, 1024−1059

(178) Mao, J.; Peng, T. Y.; Zhang, X. H.; Li, K.; Zan, L. Selective Methanol Production from Photocatalytic Reduction of CO_2 on $BiVO_4$ under Visible Light Irradiation. *Catal. Commun.* **2012**, *28*, 38−41.
(179) Iwase, A.; Yoshino, S.; Takayama, T.; Ng, Y. H.; Amal, R.; Kudo, A. Water Splitting and CO_2Reduction under Visible Light IrradiationUsing Z□Scheme Systems Consisting of Metal Sulfides, CoO_x-Loaded$BiVO_4$, and a Reduced Graphene Oxide Electron Mediator. *J. Am. Chem. Soc.* **2016**, *138*, 10260−10264.
(180) Schneider, J.; Jia, H. F.; Muckerman, J. T.; Fujita, E. Thermodynamics and Kinetics of CO_2 CO, and H^+ Binding to the Metal Centre of CO_2 Reduction Catalysts. *Chem. Soc. Rev.* **2012**, *41*, 2036−2051.
(181) Wang, Z.; Teramura, K.; Huang, Z.; Hosokawa, S.; Sakata, Y.; Tanaka, T. Tuning the Selectivity toward CO Evolution in the Photocatalytic Conversion of CO_2 with H_2O through the Modification of Ag-Loaded Ga_2O_3 with a $ZnGa_2O_4$ Layer. *Catal. Sci. Technol.* **2016**, *6*, 1025−1032.
(182) Ou, M.; Nie, H. Y.; Zhong, Q.; Zhang, S. L.; Zhong, L. Controllable Synthesis of 3D $BiVO_4$ Superstructures with Visible-Light-Induced Photocatalytic Oxidation of NO in the Gas Phase and Mechanistic Analysis. *Phys. Chem. Chem. Phys.* **2015**, *17*, 28809−28817.
(183) Ou, M.; Zhong, Q.; Zhang, S. L.; Nie, H. Y.; Lv, Z. J.; Cai, W. Graphene-decorated 3D $BiVO_4$ Superstructure: Highly Reactive (040) Facets Formation and Enhanced Visible-Light-Induced Photocatalytic Oxidation of NO in Gas Phase. *Appl. Catal., B* **2016**, *193*, 160−169.
(184) Chen, R.; Zhu, C.; Lu, J.; Xiao, J.; Lei, Y.; Yu, Z. $BiVO_4$/α-Fe_2O_3Catalytic Degradation of Gaseous Benzene: Preparation, Characterization and Photocatalytic Properties. *Appl. Surf. Sci.* **2018**, *427*, 141−147.
(185) Sun, R.; Shi, Q.; Zhang, M.; Xie, L.; Chen, J.; Yang, X.; Chen, M.; Zhao, W. Enhanced Photocatalytic Oxidation of Toluene with a Coral-like DirectZ-scheme $BiVO_4$/g-C_3N_4 Photocatalyst. *J. Alloys Compd.* **2017**, *714*, 619−626.
(186) Yang, J.; Shi, Q.; Zhang, R.; Xie, M.; Jiang, X.; Wang, F.; Cheng, X.; Han, W. $BiVO_4$Quantum Tubes Loaded on Reduced Graphene Oxide Aerogel as EfficientPhotocatalyst for Gaseous Formaldehyde Degradation. *Carbon* **2018**, *138*, 118−124.
(187) Wang, X.; Liao, D.; Yu, H.; Yu, J. Highly Efficient $BiVO_4$Single-Crystal Photocatalystwith Selective Ag_2O-Ag Modification: OrientationTransport, Rapid Interfacial Transfer and Catalytic-Reaction. *Dalton Trans.* **2018**, *47*, 6370−6377.
(188) Huang, H.; He, Y.; Du, X.; Chu, P. K.; Zhang, Y. A General and Facile Approach to Heterostructured Core/Shell $BiVO_4$/BiOI p-n Junction: Room-Temperature in Situ Assembly and Highly Boosted Visible-Light Photocatalysis. *ACS Sustainable Chem. Eng.* **2015**, *3*, 3262−3273.
(189) Li, J.; Zhou, J.; Hao, H.; Li, W.; Liu, G. Exposed Specific {040} and {110} Facets of $BiVO_4$ Modified with Bi_2WO_6 Nanoparticles for Enhanced Photocatalytic Performance. *New J. Chem.* **2017**, *41*, 6922−6927.
(190) Chen, F.; Yang, Q.; Li, X.; Zeng, G.; Wang, D.; Niu, C.; Zhao, J.; An, H.; Xie, T.; Deng, Y. Hierarchical Assembly of Graphene-Bridged Ag_3PO_4/Ag/$BiVO_4$ (040) Z-scheme Photocatalyst: An Efficient, Sustainable and Heterogeneous Catalyst with Enhanced Visible-Light Photoactivity towards Tetracycline Degradation under Visible Light Irradiation. *Appl. Catal., B* **2017**, *200*, 330−342.
(191) Zou, L.; Wang, H.; Wu, C.; Li, L.; Yuan, G.; Wang, X. Construction of All-Solid-State Z-scheme 2D $BiVO_4$/Ag/CdS Composites with Robust Photoactivity and Stability. *Appl. Surf. Sci.* **2019**, *498*, 143900.
(192) Wang, Y.; Tan, G.; Li, B.; Dang, M.; Lv, L.; Wang, M.; Zhang, D.; Ren, H.; Xia, A. Enhanced NIR Photocatalytic of Ag-RGO@{010}$BiVO_4$/RGO@{110}$BiVO_4$ Photocatalysts Induced by Resonance Effect of Transverse Electric of RGO and Transverse Magnetic of Ag. *Appl. Surf. Sci.* **2019**, *489*, 1−12.

DOI: 10.1021/acscatal.9b03411
ACS Catal. 2020, 10, 1024−1059